HYBRID CELL FOR HARVESTING MULTIPLE-TYPE ENERGIES

A Ph.D. Dissertation
Presented to
The Academic Faculty

by

Chen Xu

In Partial Fulfillment
of the Requirements for the Degree
Doctor of Philosophy in the
School of Materials Science and Engineering

Georgia Institute of Technology

Atlanta, Georgia

August 2012

Copyright 2012 by Chen Xu

HYBRID CELL FOR HARVESTING MULTIPLE-TYPE ENERGIES

Approved by:

Dr. Zhong Lin Wang, Advisor
School of Materials Science and Engineering
Georgia Institute of Technology

Dr. Gee-Kung Chang
School of Electrical and Computer Engineering
Georgia Institute of Technology

Dr. Christopher Summers
School of Materials Science and Engineering
Georgia Institute of Technology

Dr. Jud Ready
Georgia Tech Research Institute
Georgia Institute of Technology

Dr. Zhiqun Lin
School of Materials Science and Engineering
Georgia Institute of Technology

Date Approved: May 17th, 2012

ACKNOWLEDGEMENTS

First of all, I would like to express my deepest appreciation to my advisor, Dr. Zhong Lin Wang, for taking a chance on me as a student. He always encouraged me, guided me, let me make mistakes and try again, and allowed me to grow. From him, I learned how to create ideas, organize research, and present results, and most importantly, to stay motivated, all of which will greatly benefit me throughout my career. I would also like to extend my sincere thanks to my committee members: Dr. Gee-kung Chang, Dr. Christopher J. Summers, Dr. Jud Ready, Dr. Zhiqun Lin, and Dr. Robert Snyder. They spent their precious time giving me advice about not only my research and thesis but also my personal career development.

During my Ph.D. program, I felt very fortunate to be involved in research conducted by an excellent group—Dr. Wang's group, incredible people with whom I have worked for several years. Many thanks to my group members, all of whom helped me with my research. In particular, Dr. Ding and Ms. Yolande Berta brought me into the world of the powerful tools of TEM, SEM. Dr. Xudong Wang and Dr. Yong Qin took on roles as my mentors in the early stages of my doctoral study. Having collaborated with them on a number of projects, I learned a great deal from their expertise. Dr. Jin Liu was very helpful in mentoring me on fabrication work and also enriched my knowledge about career development. I owe considerable gratitude to them for their constant patience, abundant assistance, and great friendship.

In addition, Dr. Youfan Hu, Dr. Yan Zhang, Dr. Jinhui Song, Dr. Changshi Lao, Dr. Jun Zhou, Dr. Wenjie Mai, Dr. Sheng Xu, Dr. Caofeng Pan, Dr. Ya Yang, Tim Zhang,

Yifan Gao, Cheng Li, Fan Bai, Guang Zhu, and Wenzhuo Wu offered me tremendous support by creating a pleasant family-like atmosphere. I would like to thank them all. Moreover, I would like to thank my American coworkers, namely Dr. Benjamin Weintraub, Dr. Jenny Morber, and Dr. Melanie Kirkham, who improved my language skills, taught me about American culture, and helped me quickly adapt to this new place. Besides, I would like to thank Dr. Gordon Gu from AOC, Inc. and Dr. Jiandi Zhang from LSU for their great mentorship throughout my Ph.D. program.

With regard to Georgia Tech, I have been here a substantial part of my life and "she" has become both a beloved and despised teacher. Still, I would like to thank the admissions people who allowed me to call myself a "yellow jacket" and without whose approval my life would certainly have been very different. I would also like to thank Susan Bowman, who has more than once answered a stupid question and helped me out of a sticky situation. Moreover, I gratefully acknowledge the help that I received from the CETL faculty, particularly Jane Chisholm. These individuals played an important role in improving my language skills.

I would also like to thank my family and all my friends. Both my parents, my first two professors, deserve my respect and gratitude for showing me how one goes about doing this "research thing" and for demonstrating to me the benefits of both loving a career and being a good parent. I thank them also for the exposure to the academic environment that they provided me at a very young age. The casual experience of growing up in a university environment has impacted me far greater than they could have known. I appreciate them for their undying love, constant support, and strict parenting, without which I would be a different, and I believe, inferior person. I would also like to

thank Gordon, Nancy, Crystal, and Justina for being such a good family to me. Their love and care warms me and makes me feel strong. Although I am a foreigner, because of them, I have never felt lonely during family holidays. Most importantly, I am very grateful for my girlfriend, who has steadfastly supported me and cared about me. I would never have come this far without her.

TABLE OF CONTENTS

LIST OF TABLES

LIST OF FIGURES

SUMMARY

An abundance of energy in our environment exists in the form of light, thermal, mechanical (e.g., vibration, sonic waves, wind, and hydraulic), magnetic, chemical, and biological. Harvesting these forms of energy is of critical importance for solving long-term energy needs and the sustainable development of the planet. However, conversion cells for harvesting solar energy and mechanical energy are usually independent entities that are designed and built following distinct physical principles. For example, a solar cell (SC) works only under sufficient illumination of light while a mechanical energy generator requires significant mechanical movement/vibration. The effective and complementary use of such energy resources whenever and wherever one or all of them are available demands the development of innovative approaches for the conjunctional harvesting of multiple types of energy using an integrated structure/material.

By combining solar and mechanical energy-harvesting modules into a single package for higher energy conversion efficiency and a more effective energy recovery process, the proposed research aims to design and demonstrate a hybrid device. The proposed hybrid cell (HC) integrates a dye-sensitized solar cell (DSSC) and a piezoelectric nanogenerator (NG) that share an electrode and use ZnO nanowire arrays (NWs) as a common material for both units. The integration of the DSSC and NG can be either in a series or in parallel by following different fabrication procedures. Currently, the prototype and second generation of the HC device have been designed and some promising results have been obtained. Based on the results of current data, the serially-integrated HC model successfully added up the power output from both an SC and an NG

in addition to the open-circuit voltage. In addition, the HC successfully demonstrated the ability to simultaneously harvest solar and mechanical energy.

The overall objective of the research is to fully utilize the energy available from our living environment by developing a technology that harvests multiple forms of both solar and mechanical energy 24 hours a day. As the proposed research represents a breakthrough in the innovation of energy harvesting, it should pave the way toward building a new field called “multi-type hybrid” energy harvesting.

CHAPTER 1

INTRODUCTION

1.1 Motivation

1.1.1 The history of energy

Energy[1] plays a vital role in shaping both the human condition and civilization. People's need for energy is equivalent to their need to survive. Throughout history, some of the most important activities of human life depended on energy production and consumption, and the advance of civilization as well as the evolution of human societies has become dependent on the conversion of energy for human use. For tens of thousands of years, people have relied solely on the chemical energy gained from food that produced the mechanical energy of working muscles. However, thanks to human intellect, people understand much more now than before how to generate, store, and utilize energy for civilization. The concept of energy emerged out of the idea of living force. The word "energy" derives from the Greek ἐνέργεια , or *energeia*, meaning "activity, operation." Energy is often understood as the ability of a physical system to generate work on other physical systems. Since "work" is defined as a force acting through a distance (a length of space), energy is equivalent to the ability to exert a pull or a push against the basic forces of nature along a path of a certain length. Moreover, energy, subjected to the law of the conservation of energy, can neither be created (produced) nor destroyed; it can only be transformed. The total inflow of energy to an isolated system must equal the total outflow of energy from the system plus the change in the energy contained within the system.

Because it can be transferred, energy can more easily be stored in systems without being present as matter, or as kinetic or electromagnetic energy. Stored energy is created whenever a particle has been moved through a field it interacts with, but the energy

required to accomplish such movement is stored as a new position of the particles in the field, referred to as "potential energy." Some forms of energy can often be readily transformed into others with the help of a device. For instance, a battery transforms chemical energy into electric energy; a dam transforms gravitational potential energy into kinetic energy of moving water (and the blades of a turbine) and ultimately to electric energy through an electric generator. Similarly, in the case of a chemical explosion, chemical potential energy is transformed into both kinetic and thermal energy within a very short time. A final example is that of a pendulum. At its highest point, the kinetic energy is zero, and the gravitational potential energy is at maximum. At its lowest point, the kinetic energy is at maximum and equal to the decrease in potential energy. If one ideally assumes that no friction is present, the conversion of energy involved in these processes is perfect, and the pendulum will infinitely continue to swing.

Regardless of the type of energy, human existence has been dependent upon a need for energy. As the world's population has grown exponentially, the demand for energy and different sources of energy has increased dramatically. People need available, reliable, affordable energy. Ever since the Industrial Revolution, fossil fuels, including coal, oil, and natural gas, have been the impetus to immense technological progress. However, as supplies of fossil fuels are limited, continued reliance on them may have significant environmental and social consequences. Fortunately, much attention has turned toward alternative sources of energy that replace traditional fossil fuels.

1.1.2 The category of energy

Until recently, energy has referred to any power source that could be acquired and utilized by human beings. Despite the availability of many types of energy in nature, researchers have been working on research and development of new types of energy[2] that

can meet the demand of modern development. In this research, energy is categorized as natural/artificial, polluted/clean, and regular/new, discussed below.

1. Depending on its source, energy is divided into first energy (natural energy) and second energy (artificial energy). “First energy” refers to naturally-existing energy sources that are derived directly from the environment. First energy consists of renewable hydro energy and non-renewable fossil fuel, including coal, oil, and gas. Hydro and fossil fuels are major types of natural energy that form the basis of global energy. First energy also consists of renewable energy including solar, wind, hydro, geothermal, oceanic, biological, and nuclear energy. “Second energy” refers to other energy types that are converted from first energy sources either directly or indirectly. Examples of second energy are electricity, oil, gas, coal gas, gasoline, diesel fuel, coke, clean coal, and methane.
2. Depending on its environmental consequences, energy is also categorized as either polluted or clean. Polluted energy includes coal, oil, and other fossil fuels while the clean energy includes hydro, solar, wind, and nuclear energy.
3. Depending on its use, energy is also divided into regular energy and new energy. Regular energy comprises hydro energy from first energy and fossil fuel from non-renewable energy. New energy includes primarily solar, wind, geothermal, ocean, biological, and nuclear energy.

From the perspective of environmental sustainability and long-term development, people are seeking clean, renewable energy sources from the environment to replace polluted, non-renewable fossil fuels, currently the major sources of energy.

1.1.3 Impact and direction of energy harvesting

The harvesting of energy from the environment dates back to the origins of the windmill and the waterwheel. Their modern day counterparts are hydro-power plants, wind farms, solar farms, and more recently, novel piezoelectric devices for power generation from mechanical vibration. The full utilization of power sources such as light, thermal, and mechanical energy is critical to our long-term energy needs and sustainable development. On a small scale, for example, the development of a wireless self-powered system that harvests its operating energy from the environment is an attractive proposition for sensing, personal electronics, and defense technologies.

Most energy today comes from fossil fuels, which unfortunately produce a considerable amount of CO_2 emissions, causing numerous environmental and health problems. To ensure sustainable development of our society, we must not only develop renewable energy sources but also find other innovative solutions to the energy problem. Currently, renewable energy comprises only 8.36% of energy production[3] worldwide (Figure 1.1), so considerable effort has gone to renewable energy harvesting[4], such as solar[5-12], hydroelectric[13], wind[14], and hydrothermal energy[15, 16].

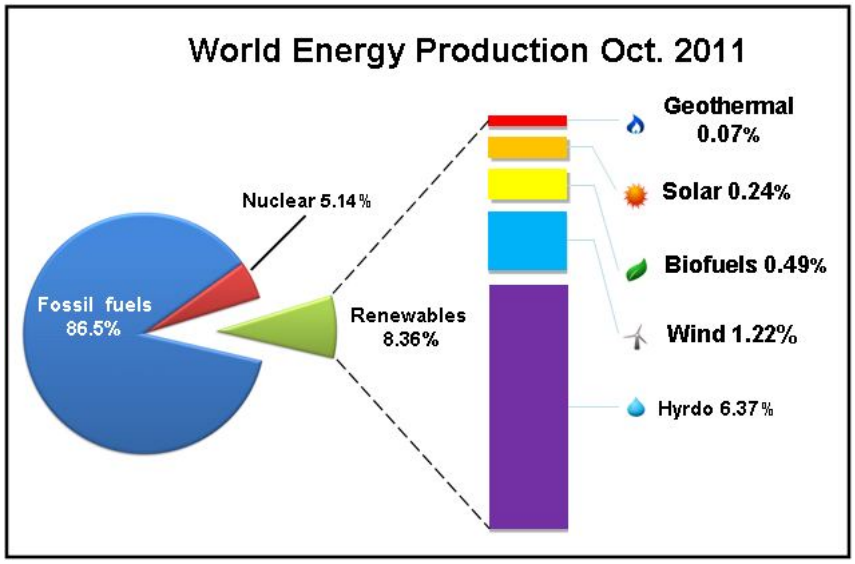

Figure 1.1 Pie chart of world energy production in October 2011 with renewable distribution.

Over the years, rationally designed materials and technologies have been developed for converting solar and mechanical energy into electricity. For example, photovoltaic technology relies on approaches such as inorganic P-N junctions[17], organic thin films[9, 18], and organic-inorganic heterojunctions[7, 8]. One of the most promising devices for inexpensive, large-scale solar energy conversion is the dye-sensitized cell (DSSC). More recently, a device in which traditional nanoparticle film is replaced by a dense array of oriented, crystalline ZnO nanowires has been developed. This device provides a larger surface area than a nanoparticle for the adsorption of light-harvesting molecules. Mechanical energy generators using the principles of electromagnetic induction and the piezoelectric effect[19-21] have also been developed. Using piezoelectric ZnO nanowire (NW) arrays, researchers have designed a novel approach for producing continuous direct-current output with the use of aligned NWs covered by a zigzag top electrode. In this device, a nanogenerator was driven by ultrasonic waves, establishing a platform for producing usable power output for nanodevices by harvesting mechanical energy[20] from the environment. All of the existing technologies have been developed independently and designed based on drastically different physical principles and diverse engineering approaches to uniquely harvesting a particular type of energy[22].

One-dimensional semiconductor nanostructures[23, 24], a subset of these materials, have been the focus of considerable attention, particularly for energy-harvesting technology, because of their unique properties and complex structures. Many nanostructure-based materials are promising candidates for multi-type energy-harvesting devices. The birth of HC devices could be important for the development of innovative technologies for maintenance-free, self-powered systems[20] without batteries or at least for the extension of the life time of batteries. This technology is particularly attractive for the study of wireless sensor networks[25], environmental monitoring[26], biomedical devices[27], and personal electronics[28, 29].

1.2 Zinc oxide nanostructures

The first attempt to synthesize nanobelts[24] for semiconducting oxides was made by Pan et al. in 2001. In their work, they developed ultra-long belt-like nanostructures for semiconducting the oxides of zinc, tin, indium, cadmium, and gallium by simply evaporating metal oxide powders at high temperatures. These oxide nanobelts are pure, structurally uniform, and single crystalline, and most are free from defects and dislocations. Work[24] by Pan et al. presents an ideal system that thoroughly explains the dimensionally-confined transport phenomena in functional oxides and that can build functional devices[30] along individual nanobelts. In addition, because of its well-defined geometry and perfect crystallinity, semiconducting oxide nanobelts have become a family of model materials that should facilitate a systematic understanding of fundamental electrical, thermal, optical, and ionic transport processes in wire-like nanostructures.

Since oxide nanobelts were first synthesized, myriad studies of functional oxide-based one-dimensional[23, 31-33] (1D) nanostructures[34] have been conducted because of their potential applications in optics, optoelectronics, catalysis, and piezoelectricity. Semiconducting oxide nanobelts, a unique group of quasi-1D nanomaterials, have been systematically studied, for they represent a wide range of materials with distinct chemical compositions and crystallographic structures. Field-effect transistors[35] and ultrasensitive nano-sized gas sensors[31] as well as nanoresonators[36] and nanocantilevers[37] have been fabricated based on individual nanobelts. Thermal transport along nanobelts has also been measured.

Among all the semiconducting oxide materials, zinc oxide is unique because it comprises the richest family of nanostructures with regard to both its structure and properties. In the past ten years, zinc oxide has been the most common semiconductor material, spawning a new research field based on ZnO[38] nanostructure-based devices. With a solid vapor phase thermal sublimation technique[39], nanocombs[40], nanorings[41, 42],

nanohelixes/nanosprings[42, 43], nanobelts[44], and nanowires[32, 44] of ZnO have been synthesized under specific growth conditions. They are widely used as catalysts[45], sensors[46], piezoelectric transducers[47], and photonic materials[48-50]. Moreover, since ZnO is a bio-compatible material, it is an ideal candidate for biological applications[31].

1.2.1 Basic properties of zinc oxide

a) Crystal structure

ZnO is a piezoelectric, transparent, semiconducting material. With a direct band gap of 3.37eV, ZnO[51-53] exhibits near-UV emission, transparent conductivity, and resistance to high- temperature electronic degradation. ZnO NWs, with all the properties of bulk ZnO, have other properties that are distinct to a nanoscale material. Because of these properties, ZnO NWs represent a very unique material with many potential applications in energy- harvesting devices.

The crystal structure of ZnO nanocrystalline, a wurtzite structure (space group C6mc) with lattice parameters of a=0.3296nm and c=0.52065nm, can be described as the number of alternating planes composed of tetrahedrally-coordinated Zn^{2+} and O^{2-} ions stacked along the c-axis (see Figure 1.2). The oppositely-charged ions produce positively-charged Zn(0001) and negatively-charged O($000\bar{1}$) polar surfaces, resulting in a normal dipole moment and spontaneous polarization along the c-axis.

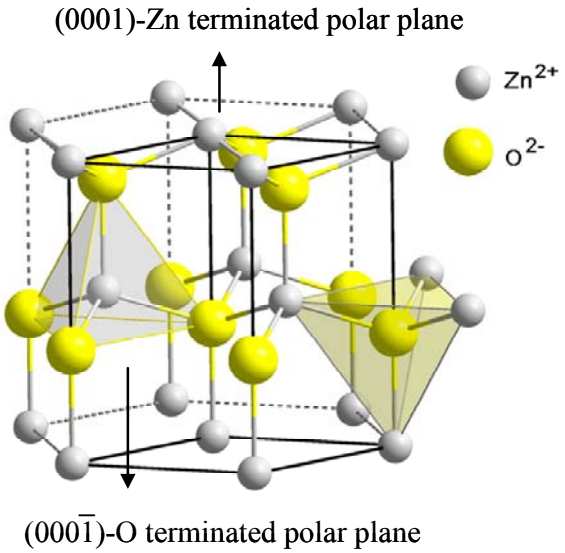

Figure 1.2 The wurtzite crystal structure of ZnO

Naturally, this formation takes on a non-symmetric structure, both atomically and electrically, which contributes to the spontaneous polarization of ZnO. Under no pressure, the centers of the negative charges coincide with those of the positive charges. Therefore, when no deformation of the material takes place, ZnO material exhibits a neutral electric charge. However, when pressure is exerted on the material, mechanical deformation initiates displacement between the centers of the positive and negative charges. The displacement, considered a dipole, is the origin of piezoelectricity present in ZnO.

Because of its high surface-to-volume ratio, the ZnO nanostructure is a perfect candidate for a photoelectrode of a dye-sensitized solar cell. The higher the surface area ratio is, the more dye loading can be achieved in the solar cell. Hence, more photons will be absorbed on the interface of the dye molecule, resulting in a large photo current. However, because of its limitations with regard to electron transport, ZnO nanostructure-based DSSC is not as efficient as TiO_2.

b) Electrical properties of ZnO nanowires

Normally, ZnO is an n-type semiconductor, indicating that electrons are the main carrier charges. The frequently observed unintentional *n*-type conductivity has often been attributed to oxygen vacancies. To maintain the charge balance, one oxygen vacancy is always accompanied by two electrons.

$$O_O^x \leftrightarrow \tfrac{1}{2} O_2(g) + V_O^{\bullet\bullet} + 2e'$$

As different synthesis methods for ZnO nanowires induce different levels of oxygen vacancies, the conductivity of ZnO nanowires will vary. Therefore, nanowires for DSSC are usually synthesized by the hydrothermal growth method, which entails more oxygen vacancies because of low temperature.

Obtaining higher charge carrier mobility will allow for the use of thicker active layers while minimizing carrier recombination and maintaining low series resistance of the device. To manipulate a specific contact such as the Ohmic or Schottky contact[54-56] in ZnO nanowire-based devices, we must select metals according to the difference between work functions Φ of the contact metal and those of ZnO. Work function Φ of n-type ZnO is 4.53 eV. The contact between ZnO and Au (Φ=5.1 eV) or Pt (Φ=6.1 eV) exhibits Schottky behavior while the contact between ZnO and Ti (Φ=3.9 eV) exhibits Ohmic behavior. Both kinds of contact are important in the electronics industry, whose main task is to produce reliable and repeatable devices.

Up-to-date knowledge of the fundamental processes of charge transfer and carrier recombination across interfaces is critical. Reducing device series resistance requires that contact resistance between layers be minimized, which is important in determining the fill factor and thus achieving efficient power conversion of a solar cell as well as a NG. Furthermore, the physical properties (e.g., wetting) of organic and inorganic components

and adhesion between layers are important for both the performance and the lifetime of the device.

1.2.2 Synthesis of zinc oxide nanostructures

To obtain higher efficiency of a device, we must be able to control the morphology and improve the piezoelectric properties of the electromechanically coupled effect and the optoelectronic properties of light-absorbing and charge-transporting materials. In addition, the synthesis of well-ordered arrays of ZnO nanowires is a promising route to the integration of the NG and the dye-sensitized solar cell with metal contact playing an important role in the process.

ZnO nanostructures can be synthesized in two primary ways: thermal evaporation[44] and the hydrothermal growth method[57]. The thermal evaporation method has been very successful and versatile in fabricating nanobelts and nanowires with various distinct characteristics. To form the desired nanostructures, the basic process entails sublimating source material (solid) into a powder form at a high temperature and in a subsequent deposition of the source material (vapor) in a certain temperature region. The flow gases used to carry the vapor gas are mainly argon and oxygen. However, as the determination of the exact control of oxygen partial pressure and its related thermodynamics is troublesome because of the influence of the carbothermal reduction process, nanowires are not easily fabricated in a reproducible manner.

The other approach to synthesizing ZnO nanostructures is the hydrothermal growth method, which involves the synthesis of single crystals, which depends on the solubility of minerals in hot water under high pressure. Hydrothermally-synthesized vertical arrays of crystalline zinc oxide nanowires grown on various substrates find applications in dye-sensitized and hybrid organic/inorganic bulk-heterojunction solar cells. Such applications necessitate both the ability to grow dense nanowires at high rates and a

fundamental understanding of the growth process. One method of increasing the nanowire growth rate is to stir the reaction solution. In addition, because anisotropic growth is interdependent on the intrinsic growth kinetics of the $(10\bar{1}0)$ and the (0001) surfaces of ZnO in zinc nitrate and methenamine, the growth rate, the yield, and the morphology of ZnO can be controlled simply by adjusting variables such as the temperature, the hold time, and the recirculation rate.

1.3 Thesis question and motivation

Although solving the large-scale world energy needs represent an enormous challenge, nanotechnology represents a new approach for renewable energy harvesting, a technology by which ambient energy is extracted from the environment and converted into electricity to power electronic devices. Researchers have developed several approaches for harvesting solar, thermal, mechanical, and chemical energies, but each one targets one type of energy for one particular application while ignoring the other types of energies that are, in essence, wasted. A solar cell, for example, harvests energy only from the sun, but it does not harness the energy from the heat generated by sunlight.

To fully utilize the energy available in our environment, we must develop a technology that simultaneously harvests multiple types of energy, including solar and mechanical energy, around the clock. Because conversion cells for harvesting these energy sources are usually separate and independent entities whose design and construction follow different physical principles, we need to develop innovative approaches for conjunctional harvesting of multiple types of energy using an integrated structure/material so that the energy resources can be utilized in an effective and complementary manner whenever and wherever one or all of the energy sources are available.

In an effort to address the issue, the research described in this dissertation focuses on the basic principles of and approaches to the development of HCs using nanowires. The major material in this work is ZnO, one of the most important functional semiconducting oxides. We need to investigate the controlled growth of nanoscale building blocks to understand their properties and to organize these building blocks. The objective of this research is to develop a hybrid device that combines solar and mechanical energy-harvesting modules into a single package for higher energy conversion efficiency and a more effective energy recovery process.

This work seeks to answer the following questions: Can semiconducting nanowire-based HC be produced for multi-type energy harvesting? How can we improve the performance and reliability of the HC? Can we harvest enough energy from different energy sources? How exactly does the nanostructure function in an HC device? Can we manage the power from HCs? And how do we use HCs in real applications?

The main text of this dissertation is organized into nine chapters: Chapters Two and Three present a general overview of the Dye Sensitized Solar Cell and the Nanogenerator, respectively, including their classifications, their major fabrication methods and mechanisms, and their properties and current applications. Chapters Four and Five discuss the design and fabrication of the first and second generation of HC for harvesting solar and mechanical energies. Chapter Six examines the enhancement of reliability and performance, respectively, in which a compact HC is created by the convoluted integration of two technologies. Chapter Seven then investigates the potential applications and power management of the HC and introduces a potential design of an HC, and Chapter Eight concludes.

CHAPTER TWO

DYE-SENSITIZED SOLAR CELLS

2.1 Energy from the sun

Access to economically viable renewable energy sources is essential for the development of a globally sustainable society. In the year 2008, the mean global energy consumption rate was 15 TW. However, according to even the most optimistic predictions of recent analyses, the population growth and energy consumption is expected to consume 58 TW (1.9×10^{21} joules) by the year 2100, about three times more than the current consumption. However, the maximum amount of energy that could be produced from biomass, wind, nuclear and hydroelectric sources is only 10, 2.1, 8, and 1.5 TW, respectively, calling into question the sources of more than half of the future global energy needs.

Traditionally, electricity generated from large-scale ambient energy such as the sun, the wind, and ocean waves is widely available, but technologies do not yet exist to capture it efficiently. As the discrepancy of discovery and the consumption of fossil fuels continue, the development of alternative energy has become an increasingly compelling problem for researchers. Energy harvesters currently do not produce sufficient energy to perform mechanical work, but instead provide a very small amount of energy to power low-energy electronics. However, because both the military and commercial sectors have a great need for energy-harvesting devices such as solar cells, thermoelectric devices, and piezoelectric devices, Chapters Two and Three of his research will discuss Dye-sensitized Solar Cell and piezoelectric Nanogenerators, respectively, state-of-the-art technology that can be used to harvest energy from several sources simultaneously.

In renewable energy harvesting, photovoltaic technology, also referred to as the solar

cell, is one of the most popular approaches to converting solar energy into electricity. The sun, 150 million kilometers far from the earth, is an inexhaustible (at least for a few billion years) and freely available energy source, generating more than 10,000 times the global energy consumed . Thus, solar energy represents an optimal long-term solution for the energy crisis. For thousands of years, human beings have utilized energy from the sun for drying clothes and food. However, only recently have they begun to harvest solar energy for generating electric power. Solar energy, besides fusion, has the greatest potential to satisfy future global demand for renewable energy sources. Even a tiny fraction of the sun's energy that reaches the earth (around a hundredth of a millionth of a percent) is more than enough to meet all of our power needs, if only we could harness it properly. From the 1.7 × 105 TW of solar energy that strikes the earth's surface, a practical terrestrial global solar potential value is estimated to be about 600 TW. Thus, even if solar farms run at 10% efficiency, they can easily about 60 TW of power.

The sun emits light with a range of wavelengths from ultraviolet and visible to the infrared. Light peaks in the visible wavelength, resembling the blackbody spectrum at a temperature of 5760 K. However, it is influenced by atmospheric absorption and the position of the sun. Ultraviolet light is filtered out by ozone, and water and CO_2 are absorbed mainly by infrared light, causing dips in the solar spectrum at 900, 1100, 1400, and 1900 nm (H_2O) and at 1800 and 2600 nm (CO_2). When skies are clear with the sun directly overhead, radiation takes the shortest path through the atmosphere, strikes the earth's surface at its maximum level. The path length is referred to as the air mass (AM), which is defined as the ratio of the actual radiation path to the shortest path. It can be approximated by AM $1/\cos\theta$, in which θ is the angle of elevation of the sun. The standard solar spectrum used for measurements of solar cell efficiency is AM 1.5 G (global), given that $\theta = 42°$. This spectrum is normalized so that the integrated irradiance (the amount of radiant energy received from the sun per unit area per unit time) is 1000 W m^{-2}. Irradiance varies, depending on the position of the sun, the orientation of the Earth, and

the conditions of the atmosphere.

Sunlight can also be categorized into direct or diffuse light. Direct light can be concentrated, which increases the solar cell efficiency by increasing cell voltage outputs. Diffuse light arises from the scattering of sunlight in the atmosphere at an average of about 15%), but this value is larger at higher latitudes and in regions with a significant amount of cloud cover. The AM 1.5 G solar radiation spectrum can be found from different sources. The spectrum illustrated in Figure 2.1 is the irradiance of the sun as a function of wavelength.

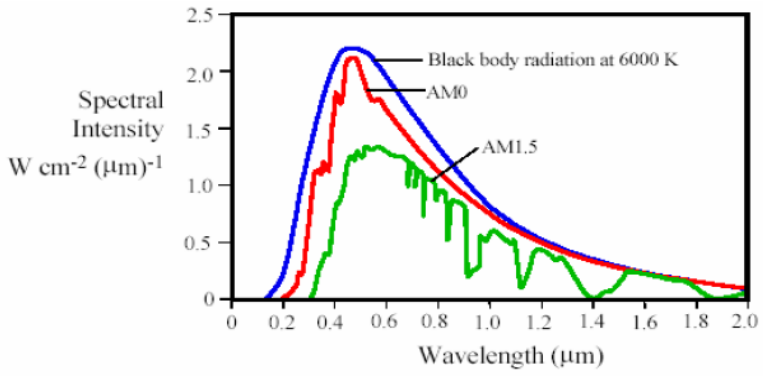

Figure 2.1 Solar energy spectrum

To harvest the enormous amount of energy emitted by the sun, the first solar cells used Si-based PV. According to the theory of the solar cell, when a photon hits a piece of silicon, one of three phenomena can occur: (i) The photon can pass straight through the silicon, which (generally) occurs when lower energy photons are involved; (ii) the photon can reflect off the surface of the silicon; and (iii) if the photon energy is higher than the silicon band gap value, the photon can be absorbed by the silicon, generating an electron-hole pair and sometimes heat, depending on the band structure, as in Figure 2.2.

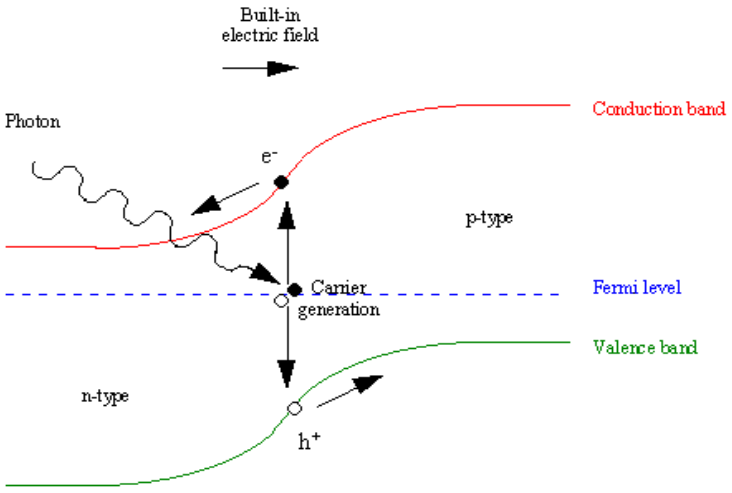

Figure 2.2 Band diagram of a silicon solar cell

When a photon is absorbed, as shown in the above figure, its energy is transferred to an electron in the crystal lattice. Usually this electron is in the valence band and tightly bound in the covalent bonds between neighboring atoms; hence, it is unable to move far. The energy transferred to it by the photon "excites" it into the conduction band, where it is free to move around within the semiconductor. The covalent bond that the electron was previously a part of then has one fewer electron, called a “hole.” The presence of a missing covalent bond allows the bonded electrons of neighboring atoms to move into the "hole," leaving another hole behind, and in this way, a hole can move through the lattice. Thus, it can be said that photons absorbed in the semiconductor create mobile electron-hole pairs.

A photon must only have greater energy than that of the band gap in order to excite an electron from the valence band into the conduction band. However, the solar frequency spectrum approximates a blackbody spectrum at about 5800 K, and as such, much of the solar radiation reaching the earth is composed of photons with energy greater than those in the band gap of the silicon. These higher energy photons will be absorbed by the solar cell as well, but the difference between the energy of these photons and those

of the silicon band gap is converted into heat (via lattice vibrations — called phonons) rather than usable electrical energy.

2.2 Characterization of solar cells

A commonly used method of evaluating the performance of the solar cells is current vs. the voltage curve, shown in Figure 2.3. I_{sc} is the photocurrent of the short circuit, which indicates the maximum current (short-circuit condition) for a solar cell device converting all incident photons below the absorption onset wavelength into electric current; and V_{oc} is the open circuit voltage when no current is flowing through the terminals, which equates to the energy splitting of the electron and hole quasi-Fermi levels in bulk intrinsic material. FF is the fill factor of the cell, defined as $I_{mp}V_{mp}/I_{sc}V_{oc}$, in which Imp and Vmp are the peak power current/voltage; and P_{solar} is the incident solar power. For air mass (AM) of 1.5 sunlight (solar zenith angle 48.19°), P_{solar} corresponds to $1000W/m^2$.

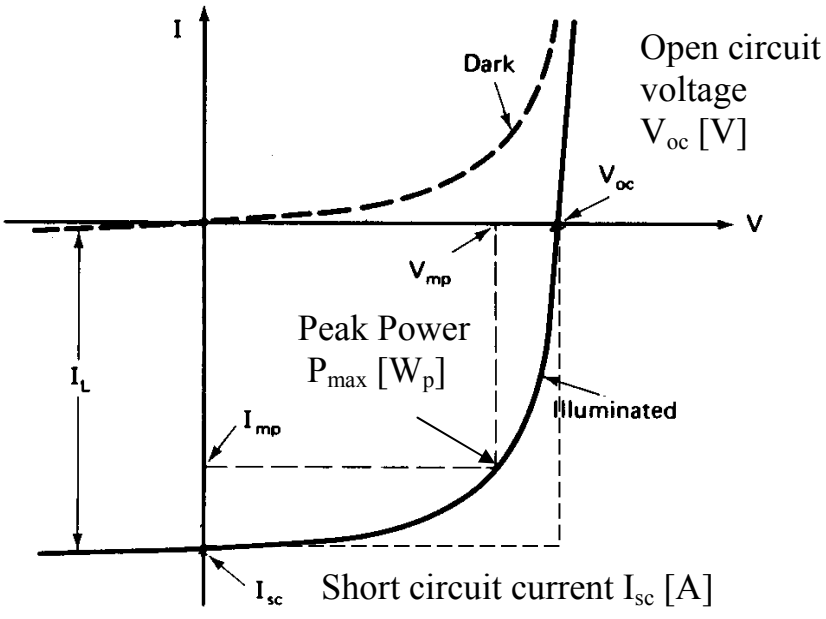

Figure 2.3 A typical current vs. a typical voltage curve

The overall energy conversion efficiency,η, for a solar cell can be calculated as shown in the following equation:

$P_{max}=V_{mp}I_{mp}=FFV_{oc}I_{SC}$

$\eta=P_{max}/P_I=J_{sc}V_{oc}\ (FF)/P_I$

2.3 The evolution of solar cells

Under laboratory conditions and with current state-of-the-art technology, single crystal silicon solar cells with close to 25% efficient can be fabricated. Moreover, as shown in Figure 2.4, solar cells have drawn considerable attention from the research society. Multi-junction cells and single-junction GaAs have very high efficiency and used mainly in space applications in which cost is not a concern. Crystalline Si-based cells are the most conventional PV technologies and have been widely adopted because of their efficiency and low cost while thin-film and emerging PV, while lagging behind, are catching up in this regard.

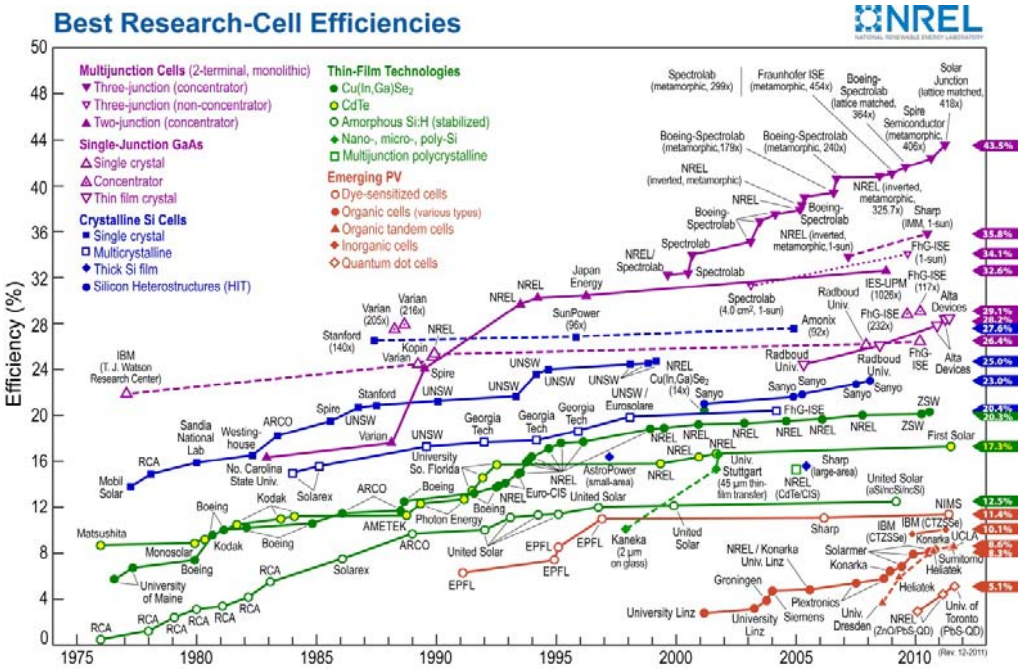

Figure 2.4 NREL's measurement of the best solar cell efficiencies

However, commercially mass-produced cells are typically only 15-16% efficient. The overriding reason for this difference in efficiency is that the research techniques used in the laboratory are not suitable for commercial production within the photovoltaic industry and therefore, lower cost techniques with lower efficiency are used.

Solar cell research continues to improve the efficiency of solar cells, with targets aimed towards the currently accepted limit of 25-30%. Efficiency results for commercially-produced solar cells lag some years behind those for laboratory-produced cells. However, it has been estimated that module efficiencies over 20% could be produced commercially. Even though the efficiency of solar cells continues to improve, we must account for another factor: cost. The use of advanced materials and technology that achieve higher efficiency raise the cost of production. In terms of the cost effectiveness, solar cells can be divided into three generations corresponding to regions in Figure 2.5. First-generation technologies mainly consist of crystalline Si-based cells with an efficiency of ~ 20%; however, their cost is relatively high. Second-generation technologies include thin-film and amorphous Si- based PV, which have lower cost and efficiency. To achieve truly competitive cost/efficiency ratios, third-generation PV technologies may require breakthroughs, even in mainstay technologies, originally developed by Martin Green of the University of New South Wales[58]. Here, third-generation technologies (III) can be separated into two categories. The first, IIIa, consists of novel approaches that strive to achieve very high efficiency by using concepts[59, 60] (e.g., hot carriers, multiple electron–hole pair creation, and thermophotonics) that have theoretical maximum efficiencies well in excess of the 31% target for single-junction devices such as multi-junction[61] or single-junction GaAs[62-64]. In this case, the allowable cost of the cell could be quite high. However, research in this area, still in its infancy, has presented examples of the fundamental mechanisms, but it has not yet yielded any working devices. The second type of third-generation device, IIIb, strives to achieve

moderate efficiency (15–20%), but at a very low cost. This goal will require inexpensive materials for active components, packaging, low-temperature atmospheric processing, and high fabrication throughput. One member of this category, organic-based photovoltaics[65, 66] (OPVs), can potentially have a significant impact on flexible electronics applications. However, achieving these goals will require significant basic and applied science advancements in the next decade.

The development of an affordable energy solution must involve a tradeoff at some point. For the cost of a given module, the more efficient it is, the more cost effective it is because it entails fewer additional costs (e.g., wiring costs) to generate the same amount of power. Ultimately, this suggests that the more efficient a PV module is, the more cost effective it becomes, and thus, the more attractive photovoltaics become as a source of electricity for both domestic and industrial use.

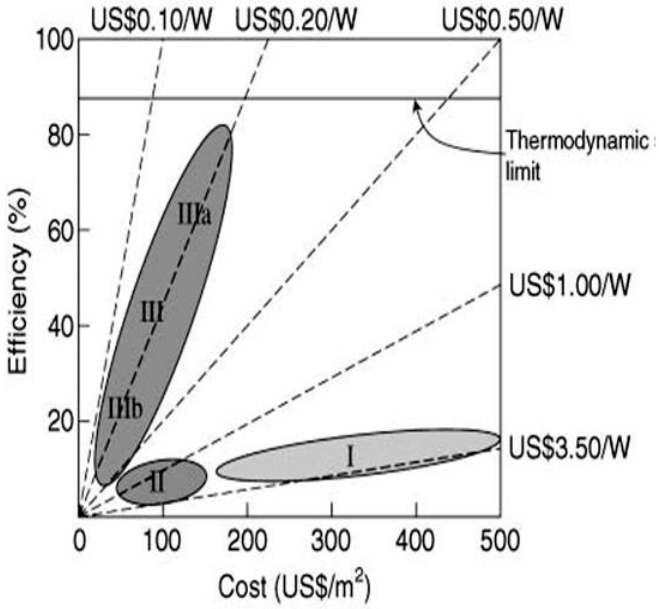

Figure 2.5 Cost-efficiency analysis for first-, second-, and third-generation photovoltaic technologies (labeled I, II, and III, respectively). Region IIIa depicts very-high-efficiency devices that require novel mechanisms of device operation. Region IIIb, the region in which organic PV devices lie, depicts devices with moderate efficiency and very low cost.

From previous analysis, inorganic solar cells have high efficiency and a long lifetime, but are expensive to produce. Unfortunately, highly efficient silicon solar cells require highly purified silicon, which drives production costs to an economically unviable level. In addition, it is desirable to operate the cell at low temperature, which adds cooling and maintenance expenses. Current organic solar cells are inexpensive to produce, but also have a shorter life span and lower efficiency than inorganic cells. Before organic solar cells become practical, which at the moment appears still far away, both efficiency and long-term stability and protection against environmental influences will require further improvement. Hence, to balance the tradeoff between cost and efficiency, a viable option is the Dye-sensitized Solar Cell (DSSC), which shows acceptable efficiency (~10%) at a lower cost than Si-based PV. If DSSCs are able to fit the technological profile represented by the optimization of these parameters, they will be open to commercialization. Hence, we adopted DSSC in our design and the details of DSSC are discussed in the next section.

2.4 Dye-sensitized Solar Cells

A relatively new class of low-cost solar cells referred to as "Dye-sensitized Solar Cell" (DSSCs) has drawn the attention of photovoltaic researchers. Also known as Grätzel cells[7], DSSCs invented by Michael Grätzel and Brian O'Regan at the École Polytechnique Fédérale de Lausanne in 1991. are based on a semiconductor formed between a photo-sensitized anode and an electrolyte[67], a photoelectrochemical system[5]. Dye-sensitization, the basis for DSSCs, has its historical origin in the 19th century, when photography was invented by Vogel in Berlin in 1873. However, the use of dye-sensitization in photovoltaics was not exploited successfully until the success of Grätzel and colleagues. This cell is a promising technology because it can be manufactured with low-cost materials, and its production does not require elaborate components. In addition,

in contrast to conventional systems in which the semiconductor undertakes both the task of light absorption and charge carrier transport, these two functions in this system are separate. Grätzel cells, using dispersed particles, provide a sufficient interface for photo-electrodes.

The semiconductor in this cell is titanium dioxide (TiO_2), which is quite advantageous in sensitized photo-chemistry and photo-electrochemistry. Furthermore, since the standard dye in the early 1990's was "Black dye" tris (2,2'-bipyridy1-4, 4'-carboxylate) ruthenium(II), the function of the carboxylate was the attachment by chemisorption of the chromophore to the oxide substrate. Under solar illumination, the first Grätzel cell achieved a conversion efficiency of 7.1%[7], and efficiency has improved continuously in subsequent cells. The anodes of Dye-sensitized Solar Cell are typically constructed using thick films (~10 μm) of TiO_2 or, less often, SnO_2 or ZnO nanoparticles, which are deposited as a paste and sintered to produce electrical continuity.

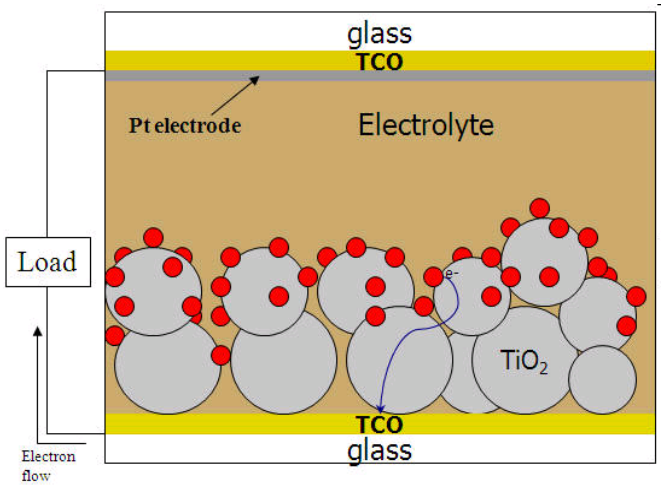

Figure 2.6 Schematics of TiO_2 nanoparticle-based Dye-sensitized Solar Cell

In 2001, Grätzel et al. achieved a new record of 10.4%[6] in conversion efficiency. However, this record was broken in 2003 when "N3 dye" cis-$RuL_2(NCS)_2$ was used in conjunction with guanidinium thiocyanate, a self-assembly facilitating additive that

allows the open-circuit voltage of the solar cell to increase substantially. Grätzel's nanoparticle DSSCs, however, still rely on trap-limited diffusion for electron transport, a slow mechanism that can limit device efficiency, especially at longer wavelengths. In 2005, Ohsaki et al. developed a dye-sensitized cell with a TiO_2 nanotube[68] as the photoelectrode with a larger specific surface area. Meanwhile, researchers have conceived of using other semiconductor materials as photoelectrodes. Zinc oxide is an ideal candidate that substitutes for TiO_2 because it has similar semiconducting properties and various nanostructures.

In 2005, Law et al. introduced a new version of the dye-sensitized cell[69] in which the traditional nanoparticle film was replaced by a dense array of oriented, crystalline ZnO nanowires. The nanowire anode, synthesized by mild aqueous chemistry, features a surface area as little as one-fifth the nanoparticle cell. Direct electrical pathways provided by the nanowires ensure the rapid collection of carriers generated through the device. The authors attained a full solar efficiency of 1.5%, limited primarily by the surface area of the nanowire array. In addition, the authors substituted the photo-sensitized dye with "N719 dye" ($[RuL_2(NCS)_2]$: 2 TBA). This work provides an efficacious approach to utilizing the nanostructure of ZnO. Before this work, most of the research focused solely on photo-sensitized dye, the interface between the photo-electrode and the dye and the electrolyte.

2.4.1 How does it work?

Nanocrystalline DSSC, based on the mechanism of a fast regenerative photoelectrochemical process, converts sunlight into electricity, just as a conventional cell made of Si does. Unlike Si cells, the functional element responsible for light absorption (the dye) is separate from the charge carrier.

As shown in Figure 2.6, the structure of DSSCs can be divided into three

components: the photoanode, the redox couple, and the counter electrode. The photoanode is generally composed of a transparent conducting oxide (TCO) substrate coated with high surface area nanocrystalline titanium dioxide (TiO_2) that has been sensitized with a broadly absorbing dye such as cis-$Ru(dcb)_2(NCS)_2$(Known as N3, dcb=4,4'- dicarboxylate-2,2'-bipyridine). The most common redox couple is iodide/triiodide, and the counter electrode is often a platinum-coated TCO in which a reduction in the redox mediator occurs. To complete the circuit, sensitization involves the formation of the molecular-excited state (1), followed by electron injection into the conduction band of the semiconductor (2). The electrons travel to the counter electrode to reduce the triiodide (3), and oxidized dye is regenerated into its chromophoric form by iodide (4) to complete the process with no net chemical reaction.

$S + h\upsilon \rightarrow S^*$	metal to ligand charge transfer excitation	(1)
$S^* + TiO_2 \rightarrow S^+ + TiO_2 (e^-_{cb})$	electron injection	(2)
$I_3^- + 2\ e^- \rightarrow 3\ I^-$	triiodide reduction	(3)
$2S^+ + 3\ I^- \rightarrow 2S + I_3^-$	dye regeneration	(4)

In the case of an n-type semiconductor, TiO_2 (bandgap 3.2 eV), the dye becomes excited by absorbing a photon and then injects the electron into the TiO_2, which can then be extracted at the front electrode (a transparent TCO glass) as an external current. The dye is also subsequently reduced by a redox electrolyte, which consists of an organic solvent and the redox couple iodide/triiodide.

The electrolyte also drives the charge transport between the counter electrode (also TCO glass) and the dye molecules. The counter electrode is covered with some Pt, which acts as a catalyst for the redox reaction, in order to obtain low-resistant electron transfer. It can be shown that only the dye molecules directly attached to the surface of the semiconductor are able to inject charge carriers efficiently into the semiconductor.

2.4.2 Manufacturing

The standard way of preparing the DSSC in a laboratory is to sandwich the various cell layers between two glass plates, the substrate and the superstrate, which are usually a TiO2 electrode. In order to minimize the manufacturing cost of mass production, single cells should be prepared between one common glass plate with a large surface area, which already takes place in the fabrication of commercial thin film modules.

Kay and Grätzel (1996) developed a three-layer monolithic cell structure that adopts a number of processing benefits of thin film solar cell technology. Thus, it can be commercialized. In the monolithic structure, all the layers of the cell can be deposited on top of one another on a single TCO-coated glass plate while the opposite glass plate without TCO coating serves merely as a protective barrier and encapsulation. All in all, except for Tennakone et al. (1999), attempts at replacing TiO2 with some other large band-gap semiconductor such as SnO2, ZnO, Cds, or CdSe have been in vain.

2.4.3 Advantages/Disadvantages

One of the major advantages of DSSC technology over other PV technologies is the relatively simple manufacturing processes and the inexpensive equipment and facilities needed. For example, old-fashioned screen-printing machines can be used instead of expensive clean room facilities, required for semiconductor processing. Furthermore, the materials of cells may become less expensive in large-scale production. (At present, costs are significant for cell elements such as the dye and the Pt catalyst at the back contact.)

Since the Dye-sensitized Solar Cell are printed on foil, they are flexible and therefore can be adapted to almost any shape. They do not have to reach the high efficiency

achieved by Si solar cells because they can be used in other ways. For example, they can be effectively used in the window glass of a building and thus distributed over areas in addition to the roof.

To become an economically viable and commercially feasible technology, Dye-sensitized Solar Cell should be capable of maintaining non-degrading performance in operating conditions over several years, preferentially decades. However, the question of the long-term stability of Dye-sensitized Solar Cell remains unanswered thus far, for potential sources of degradation in the cell such as changes in the surface structure of the TiO_2 or photo-chemical or chemical degradation of the dye still exist.

2.4.4 Future outlook

Although the M. Grätzel group at the Energy Research Centre of The Netherlands (ECN) achieved an efficiency record of 10.8% on small active areas (<1cm^2) of DSSC cells and a conversion efficiency of as much as 8.23% on larger areas (>1cm^2), several problems inherent in the development of Dye-sensitized Solar Cells for a large-scale applications have not been solved. In addition to determining the cause of the moderate efficiency, we must address more fundamental research issues such as the improvement in the stability of cell components and cells[70-72].

CHAPTER THREE

THE NANOGENERATOR

3.1. Harvesting mechanical energy

Photovoltaics, thermal electricity, and electromagnetic induction are well-established technologies for energy harvesting. In light of the availability of such technologies, why do we need to harvest mechanical energy? Let us examine several cases in which energy-harvesting technology could serve useful purposes. Cases in which individual sensors are difficult to acquire (e.g., in hostile territory) or those in which a sensor network consists of a large number of nodes distributed over a large geographic area may require the immediate replacement of batteries, which may not be possible. Although the battery is one of the best choices for many personal electronics and small electronics, the replacement, recycling, and disposal can be a huge environmental problem. In such cases, access to a self-sufficient power source that derives its power from the environment and thus requires no maintenance would provide an immediate way of solving such a problem. To be self-sufficient, a system must be able to harness energy from the surrounding environment and store it for later use. One example is a nanorobot, a smart machine that may be able to sense and adapt to the environment, manipulate objects, take action, and perform complex functions. However, a key challenge is to find a power source that can drive the nanorobot without adding much weight. One can easily introduce a nanorobot into a body that performs sensing, diagnostic, and therapeutic actions, but it might prove virtually impossible to fish it out to replace its battery. In the context of military sensing/surveillance, a node placed in difficult-to-reach location may need to be hidden or withstand dusty, rainy, dark and/or deep forest conditions. Because light is not strong enough in such conditions, it precludes the use of solar cell

technologies. Methods of energy harvesting that could provide an immediate answer to a problem at hand may include systems that utilize random vibration (e.g., vibration near a roadway), temperature gradients (e.g., the relatively constant temperature below the ground), or any other phenomena that could be exploited to provide energy. The ability to harvest mechanical energy could facilitate the performance of tasks that are not feasible using current energy-harvesting techniques.

Table 3.1 Ubiquitous sources of mechanical energy that can be harvested for electricity.

Human body/motion	Transportation	Infrastructures	Industry	Environment
Breathing, blood flow/pressure, exhalation, walking, arm motion, finger motion, jogging, talking …	Aircraft, automobile, train, tires, tracks, peddles, brakes, tubine enginin, vibration, noises …	Bridges, roads, tunnels, farm, house structure, control-switch, water/gas pipes, AC system …	Motors, compressors, chillers, pumps, fans, vibrations, cutting and dicing, noise…	Wing, ocean current/wave, acoustic wave…

What types of mechanical energies are we aiming to harvest? The environment contains an abundance of mechanical energy that comes in many forms such as wind, body movement, muscle stretching, acoustic/ultrasonic waves, noise, mechanical vibrations, and blood flow, as shown in Table 3.1. Moreover, because the frequency range of an available signal has to be quite wide, but most energy falls in the low-frequency range, a technology that operates from low (~Hz) to relatively high (~kHz) frequency range is required. Finally, because the environment can vary, a technology that has a high adoptability is required. A potential technology that can address these issues is the nanogenerator (NG), which has only recently, in the last seven years, been developed.

3.2 The invention of nanogenerators

The discovery of some interesting and striking piezoelectric and semiconducting coupled phenomena[73] in zinc oxide (ZnO) nanowires, the first of which was the NG, gave

rise to the theory of electromechanically-coupled nanodevices, which attempts to explain these new phenomena. Different from other semiconductor materials, ZnO has a wurtzite structure in which the Zn cations and O anions form tetrahedral coordination. The lack of center symmetry results in a piezoelectric effect, in which a mechanical stress/strain can be converted into electrical voltage and vice versa, owing to the relative displacement of the cations and anions in the crystal.

In 2006, Wang and Song demonstrated a prototype[19] of an NG based on ZnO nanowire arrays. When a nanowire (NW) is deflected by a conductive atomic force microscope (AFM) tip in the contact mode, the piezoelectric property of the zinc oxide nanowires creates an electric field across the nanowire (Figure 3.1A) in which the stretched side is positive and the compressed side negative. Because of the Schottky barrier between the Pt-coated tip and the NW, the charge generated by the piezoelectric effect is preserved until the AFM tip passes across the top of the NW and touches the compressed side of it. When the AFM tip touches the compressed side of the NW (as shown in Figure 3.1A.), the Schottky diode between the ZnO and the Pt metal on the AFM tip is forward-biased, causing a sudden increase in the output of the electric current. Experimentally, the output current always flows from the Pt-coated AFM tip to the ZnO nanowire, which indicates that electrons flow from the ZnO NW to the metal tip. It is estimated that the efficiency of the NW-based piezoelectric NG could reach as high as 17% to 30%[19].

Experimentally, both the topography (the feedback signal from the scanner) and the corresponding output voltage images across the load were recorded simultaneously when the AFM tip was scanned over the aligned NW arrays. In the contact mode, as the tip scanned over the vertically-aligned NWs, they were bent consecutively. The bending distance was directly recorded in the topography image, from which the maximum bending deflection distance and the elastic modulus of the NW as well as the density of the NWs that have been scanned by the tip are directly derived.

In the corresponding voltage output image for each contact position, many sharp output peaks were observed (Figure 3.1C). Note the output voltage signal was actually negative in reference to the grounded end. Through examination of the topological profile of an NW and its corresponding output potential, a delay was observed for the voltage output signal (Figure 3.1D),

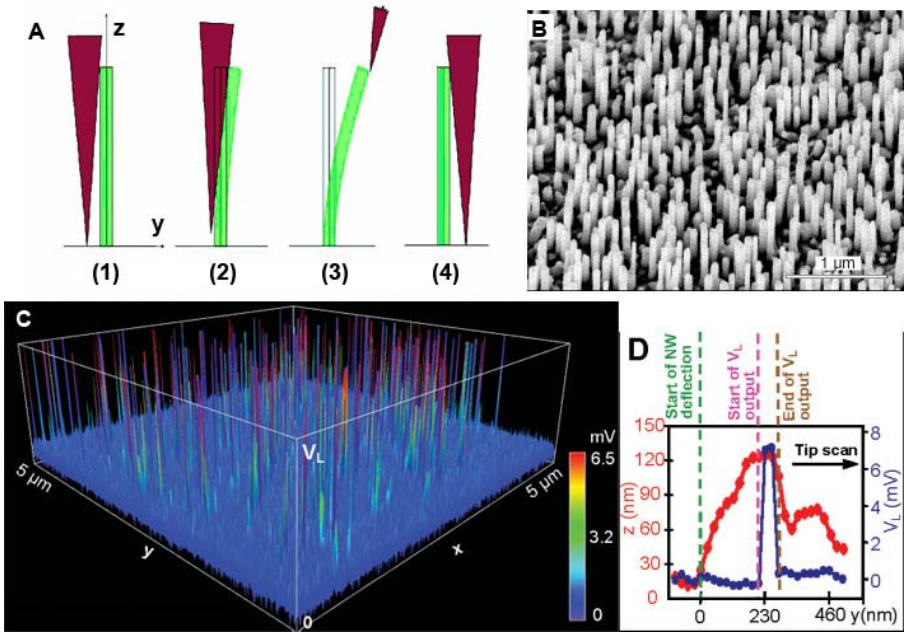

Figure 3.1 (A) The typical configuration of an AFM-based ZnO NG. When pushed by an AFM tip, mechanical deflection gives rise to an electrical field, the power of which can be released. The pushing force increases from (1) to (3), until (4) the wire is released. (B) SEM image of aligned NWs grown on a α-Al_2O_3 substrate. (C) The output voltage generated by the NWs. (D) Line profiles from the topography (red) and output voltage (blue) images across a nanowire.

which indicates no electric power output when the tip first came into contact with the NW; however, a sharp voltage peak was generated at the moment when the tip was about to lose contact with the NW. This delay is a key signature of the power output process. It is important to note that the voltage V_L presented here was converted from the current flowing through the external load R_L. The NG based on ZnO NWs has the following experimental characteristics:

i) The output potential is a sharp peak that is *negative* in reference to the

grounded end of the NW.

ii) No output current is produced when the tip first touches the NW and pushes it; electrical output is produced only when the tip almost loses contact with the NW during the second half of the contact.

iii) Power output is produced only when the tip touches the compressed side of the NW.

iv) An output signal is produced only for piezoelectric NWs. No electrical output is received if the NWs are tungsten oxide, carbon nanotubes, silicon, or metal. Friction or contact potential plays no role in the observed output power.

v) The magnitude of the output signal is sensitive to the size of the NWs.

vi) To generate electricity, contact between the tip and the NW is required to be Schottky, and the contact between the NW and the grounded end is Ohmic.

3.3 Characterization of nanogenerator outputs

Different from solar cell characterization, not only is the current vs. voltage curve measured, but the current vs. time and voltage vs. time curves are also measured for the characterization of the performance of NGs. As shown in Figure 3.2, a mechanical energy source (e.g., an ultrasonic wave or a linear motor) was turned on and off periodically to test the response of the NGs. In the absence of an energy source, the current/voltage output is zero; when an energy source is induced into the system, the open circuit voltage (Voc) and short circuit current (Isc) are measured from the voltage/current level.

3.4 Evolution of the nanogenerator

Although the principles presented in the AFM NG are applicable for energy harvesting, output power using a single nanowire is relatively small. Thus, obtaining a

significant increase in power requires the development of innovative approaches that scale up the approach. If we are to improve the performance of the NG from AFM tip-based mechanical agitation, we must

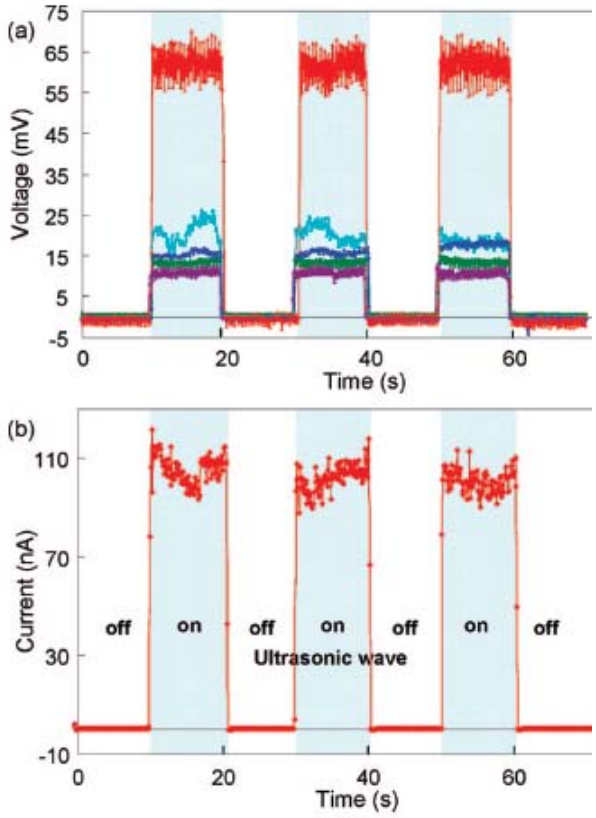

Figure 3.2 Voltage-time and current –time of NG characterization.

develop an innovative design in which we must first eliminate the use of AFM for making the mechanical deformation of the NWs so that power generation can be achieved by an adaptable, mobile and cost-effective approach over a larger scale. Second, all NWs must generate electricity simultaneously and continuously, and the generated electricity should be able to be effectively collected and output. Finally, energy that will be converted into electricity must be provided in the form of wave/vibration from the environment, even at frequencies as low as a few Hz.

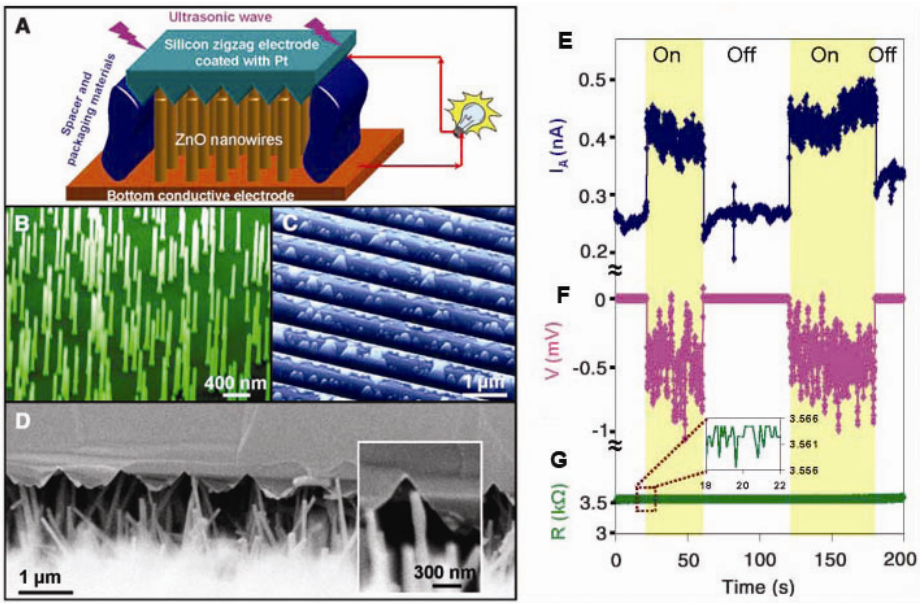

Figure 3.3 (A to D) The setup of a direct-current NG. (A) Schematic diagram showing the design of the NG. (B) Aligned ZnO nanowires grown on a GaN substrate. (C) The top electrode coated with 200nm of Pt. (D) Cross-sectional view of the NG. (E to G) Current profile, voltage profile, and resistance profile as a characterization of the performance of the NGs. (E) The short circuit current of the NG; (F) the open circuit voltage of the NG; (G) stable resistance remaining at $R = 3.560 \pm 0.005\ k\Omega$, which indicates that the jump in current could not be due to the variation in resistance.

In 2007, to develop a DC current NG driven by ultrasonic waves, Wang modified the NG[74] from the original model composed of vertically-aligned ZnO NWs and a Pt-coated zigzag top electrode. Their work, shown in Figure 3.3, changed the single AFM tip into a zigzag metal electrode, and the top electrode simultaneously and continuously created, collected, and output electricity from all of the aligned nanowires grown on a GaN or a sapphire substrate. When subject to the excitation of an ultrasonic wave, the teeth of the zigzag-shaped top electrode vibrate and push the nanowires. Each tooth, working as a single AFM tip, would also work in an AFM-based NG. When the tooth is in contact with the stretched side of the nanowire, which has a positive potential, the charge is retained because the zigzag trenches fabricated on a (001)-oriented Si substrate is coated with a thin layer of Pt. When the compressed side of the NW touches the top electrode, the metal/semiconductor interface is a forward-biased Schottky contact, so a

discharge process occurs. In one of the authors' experiments, the NG produced an electromotive force (EMF) that would generate a continuous short circuit current of ~0.15nA, with

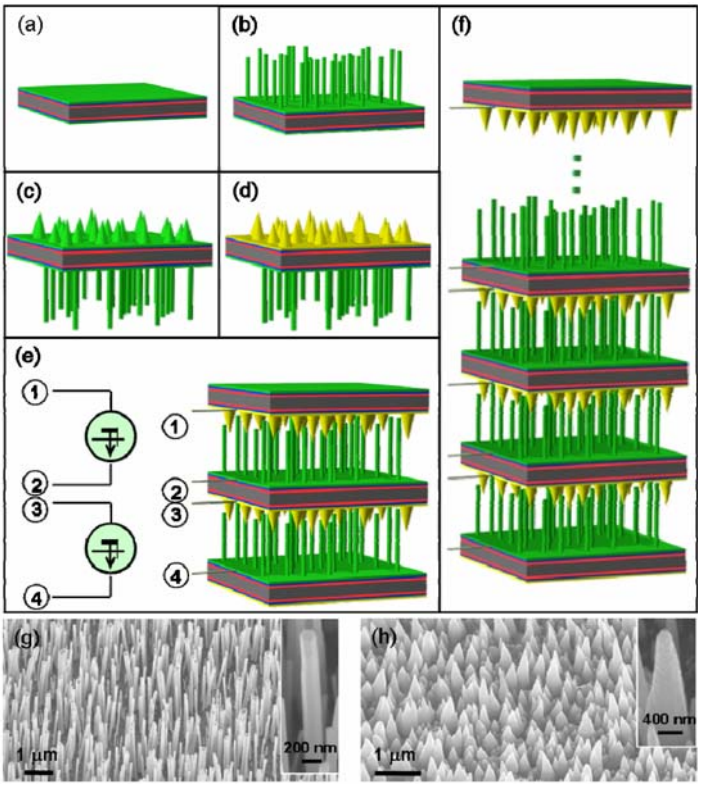

Figure 3.4 Design and fabrication procedures of the multi-layered NGs and the rational growth of the ZnO nanowire and nanotip arrays. (a) The as-fabricated substrate after coated with the $Zn(CH_3COO)_2$ seed layer. (b) Growth of hexagonal-prism-shaped nanowire arrays by the wet chemical method on one side. (c) Growth of pyramid-shaped nanotip arrays on the other side. (d) Coating the nanotip arrays with an Au layer by magnetron plasma sputter. (e) Two-layered NG made by stacking three layers of the wafer structures shown in (d) with Au-coated nanotip arrays facing and interpenetrating the bare nanowire arrays. The right-hand side is the designed symbol for representing the NGs. (f) A multilayered three-dimensional NG integrated by stacking multiple layers of wafer structures. (g) 60° tilted view SEM image of the hexagonal-prism-shaped ZnO nanowire arrays grown by the chemical approach. (h) 60° tilted view SEM image of the pyramid-shaped ZnO nanotip arrays grown by the chemical approach. Inset SEM images are high magnification views of a single nanowire and nanotip.

an open circuit output voltage of ~ -0.7mV[74]. The number of NWs that were actively generating an electric current was estimated to be 250 to 1,000.

Since the invention of direct current NGs, one breakthrough after another has

occurred[75, 76]. For one, the output current density has been significantly improved. In 2007, Wang et al. modified the design of ZnO NGs[74] so that they could effectively generate electricity inside the bio-fluid[77] with an output current as high as 35nA. By using the technique of a "double-side" testing procedure, Wang et al. successfully ruled out artifacts that might exist due to the measurement system. Their experiments also showed that connecting the NGs in parallel and in series raises their output current and voltage, respectively. The most important aspect of this work is that it clearly demonstrates the possibility of augmenting the output by three-dimensional integration and architecture.

Later in 2008 as shown in Figure 3.4, Xu et al. found a new approach to an NG[78] composed of integrated ZnO nanotip arrays and ZnO nanowire (NW) arrays that were synthesized using a chemical approach at a low temperature on the two surfaces of a common substrate. With one piece of such a structure stacked in close proximity on top of one another, forming a layer-by-layer matched brush architecture[78], a direct current was generated by exciting the architecture using ultrasonic waves. Sheng's work[78] demonstrated a four-layer integrated NG that generated an output power density of 0.11μW/cm2 at 62 mV. The layer-by-layer assembly provides a feasible technology for building three-dimensional NGs in applications in which force or pressure variations are available, such as in a shoe pad, in the underskin layer of airplanes, or in places next to a vibration source such as a car engine or a tire. More importantly, this work successfully illustrates the integration of NGs, which shows that the piezoelectric NG has a great potential of large output in the near future.

CHAPTER FOUR

HYBRID CELLS FOR HARVESTING SOLAR AND MECHANICAL ENERGIES

A subset of one-dimensional semiconductor nanostructures has been the focus of considerable interest because of their unique properties and complex structures, particularly those conducive to energy-harvesting technology. Chapters Two and Three addressed the applications of one- dimensional semiconductor materials in dye-sensitized solar cells and nanogenerators (NGs), which are useful in multi-type energy harvesting devices. This chapter introduces the creation of nanowire-based hybrid cells (HCs) for harvesting solar and mechanical energies. The birth of HC devices[79] could prove valuable to the development of innovative technologies towards maintenance-free, self-powered systems without batteries or at least to the extension of the lifetime of batteries. They could be particularly useful in wireless sensor networks, environmental monitoring, biomedical devices, and personal electronics.

4.1 Self-powered sensor network and systems[20]

A nanosystem is an integration of multi-functional nanodevices with sensory, control, communication, and actuation/response capabilities. Their low power consumption could facilitate the harvesting of energy from the environment for powering such a system. Power on the scale of microwatts is usually needed for independent, sustainable, maintain-free operations of implantable biosensors, remote and mobile environmental sensors, nanorobotics, micro-electromechanical systems, and even portable/wearable personal electronics. A nanorobot, for example, could sense and adapt to the environment, manipulate objects, take action, and perform complex functions. However, a key challenge is to locate a light-weight source of power that can drive a nanorobot. Self-

powered sensors are also needed for monitoring oil/gas transportation lines over long distances.

Self-powered sensors are a key component of defect-tolerant sensor networks, which use information- sensing equipment such as radio frequency identification (RFID), sensors, the global positioning system (GPS), and laser scanners, which connect objects to the Internet, to carry out communication, identification, positioning, tracking, monitoring, and management. By replacing the traditional finite number of discrete sensors with a large number of independent and mobile sensors distributed in the field, a statistical analysis of the signals collected through the Internet over distributed sensors can yield precise and reliable information. A conglomeration of entities that can link everyday objects and devices to large databases and networks (the Internet) are the future of health care, medical monitoring, infrastructure/environment monitoring, product tracking, and smart homes.

However, because of environmental and health concerns, such a sensor network will be highly impractical if each sensor has to be powered by a battery, particularly given the sheer number of batteries that will have to be consumed. The working mode of a wireless sensor can have an active mode, but more importantly, a standby mode, when the device is “sleeping” and consuming minimal energy. Therefore, new technologies that can harvest energy from the environment to produce sustainable self-sufficient micro/nanopower sources offer an alternative to batteries. One source of energy used for this purpose is mechanical energy. The mechanical energy available in our environment, called “random energy,” has a wide spectrum of frequencies and time-dependent amplitudes and can come from irregular vibrations, light air flow, noise, and human activity.

The power generated by an energy harvester may not be sufficient to continuously drive the operation of a device, but an accumulation of charges generated over a period of time is sufficient to drive the device for a few seconds. Such a power source could be of

practical use for devices that have standby and active modes, such as glucose and blood pressure sensors or even personal electronics such as blue tooth transmitters (driving power ~5 mW; data transmission rate ~ 500 kbits/s; power consumption 10 nW/bit), which are only periodically required to be in active mode. The energy generated when the device is in standby mode could sufficiently drive the device when it is in active mode.

Research in the near future will involve the integration of multi-functional nanodevices into a nanosystem so that it can function as a living species with capabilities of sensing, controlling, communicating, and actuating/responding. A nanosystem in the future will be composed of not only nanodevices but also a nano-power source (or nano-battery). However, the small size of the nano-battery largely limits its life-time. Therefore, if wireless devices and implanted biomedical systems were self-powered, or batteryless, it would not only greatly enhance the adaptability but also reduce the size and weight of the devices and systems. Therefore, the need for self-powered nanodevices necessitates the development of technology for harvesting energy. Such devices must be extremely small, supersensitive, extraordinary multi-functional, and extremely efficient (i.e., consuming minimal power). Therefore, energy harvested from the environment may be sufficient to power these systems.

In the working environment of a nanosystem or microsystem, the energy available for driving the system could vary from time to time and from location to location, which is especially true for mechanical vibration energy and solar energy. Although it is the most abundant energy source, solar energy, which is dependent on hours of sunlight and the weather, is not always available. Mechanical energy, which is dependent on location, may not be suitable for mobile electronics. Therefore, to effectively utilize the energies that are available at any given time and location, we require a generator that can convert all types of energy—solar, thermal, mechanical, and chemical—into electricity. For example, an emerging technology that can reliably measure various conditions in civil, aerospace, and biomedical applications is the wireless environmental sensor. One of the

major drawbacks, however, of wireless sensors is that they consume considerable power. In some remote locations, supplying power through cables or using disposable energy sources is often impractical, if not impossible. Thus, developing HCs according to a systematic approach would be highly advantageous.

4.2 The birth of the hybrid cell[79]

Photovoltaic cells, or solar cells, are a popular renewable energy technology. However, they do not function efficiently without sufficient sun light, necessitating a supplementary battery for the harvesting system, which limits their adaptability to certain applications. As mechanical energy is widely available in our living environment, we first demonstrate an approach for simultaneously harvesting solar and mechanical energies.

The hybrid cell (HC) integrates a Dye-sensitized Solar Cell (DSSC) and a piezoelectric NG built by sharing electrodes and using ZnO nanowire arrays (NWs) as a common material for both units. The integration of the DSSC and the NG can be fabricated either in a series or in parallel. The design and fabrication of the serially-integrated SC-NG hybrid cell (s-HC) entails the integration of the anode of a DSSC and the cathode of an NG onto one single silicon substrate. The structure of an s-HC is schematically shown in Figure 4.1, and the detailed fabrication process is described in Section 4.3.3.

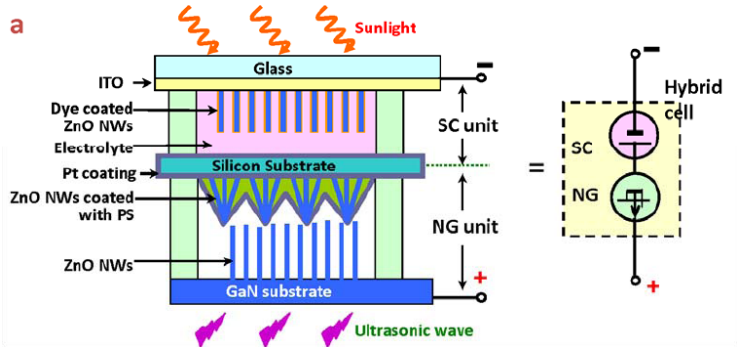

Figure 4.1 Design and structure of a hybrid cell (HC) which, composed of a serially-integrated solar cell (SC) and an NG, raises the output voltage.

The DSSC and the NG are serially integrated through a continuously-coated Pt film around the silicon substrate at the middle. An equivalent circuit of the s-HC, composed of a serially-integrated SC and an NG, is shown on the right-hand side of Figure 4.1.

4.3 Fabrication of the s-HC

In general, the DSSC was fabricated using vertically-aligned ZnO NWs, which were grown on an ITO-coated glass substrate through a hydrothermal method (Fig. 4.4). The counter electrode of the DSSC was the back side of a Pt-coated silicon substrate.

4.3.1 Materials synthesis

Thermal evaporation method[44]

Currently, thermal evaporation is the most common way to synthesize ZnO nanowires. The source material ZnO power and catalyst carbon power with a 1:1 ratio are placed at the center of an alumina tube that is later inserted into a horizontal tube furnace. The entire system is vacuumed to a high vacuum level of ~20 mTorr and then heated to 960^{o}C for an hour under a constant pressure of 30~300 Torr with specific carrier gases. By precisely controlling the pressure, temperature, synthesis time, and so forth, a high yield of nanowires, illustrated in Figure 4.2, can be synthesized at the substrates, which are placed at the downstream of the tube furnaces.

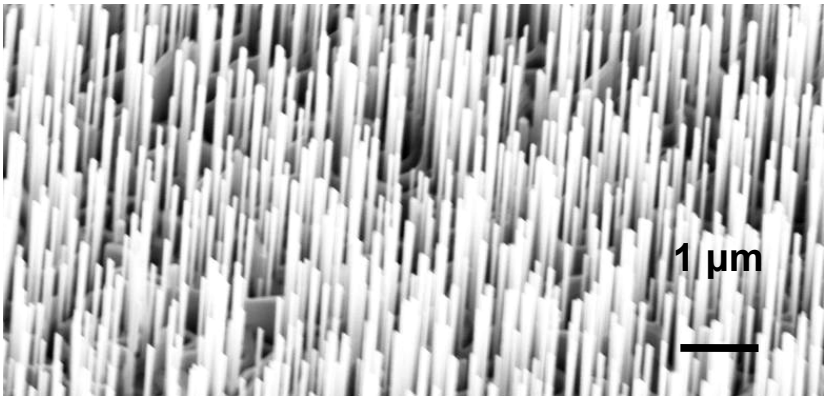

Figure 4.2 Vertically-aligned ZnO NWs grown through the high temperature vapor deposition method for NGs.

Hydrothermal method[57]

ZnO NWs were synthesized on the ITO substrate or the silicon substrate with a thin film of an ZnO seed layer. NWs were grown by immersing seeded substrates in aqueous solutions [80, 81]containing zinc nitrate hydrate and hexamethylenetetramine at 70-90ºC for 12 to 48 hours. Because NW growth slowed down after the zinc source was significantly consumed, substrates were introduced to a fresh solution after 24 hours in order to obtain long NW arrays shown in Figure 4.3.

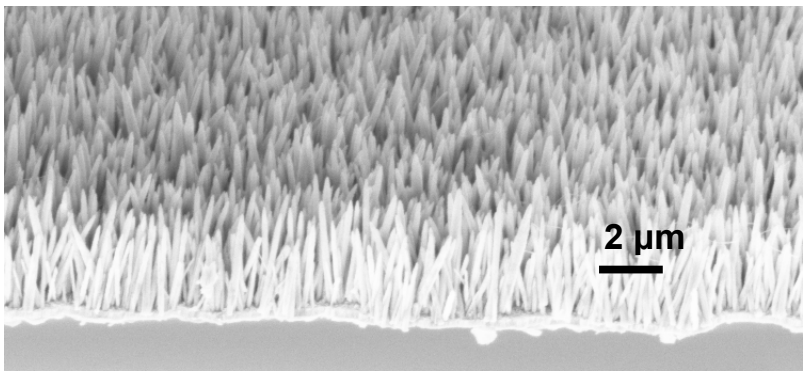

Figure 4.3 Vertically-aligned ZnO NWs grown through the hydrothermal approach for Dye-Sensitized Solar Cells.

4.3.2 Fabrication of zigzag electrode

A zigzag electrode was fabricated on a silicon substrate using aligned ZnO NW bundles as a template. Aligned ZnO NWs were synthesized using the hydrothermal approach[57] (Figure 4.5 b-1). Then the substrate with the aligned NWs was spin coated with a layer of polystyrene (Figure 4.5 b-2). The vertically-aligned ZnO NWs agglomerated into bundles under the effect of capillary force and formed cone-shape microstructures when they were embedded in polystyrene film to fill the gaps by spin coating. Finally, a thin layer of Pt (~200 nm) was coated on the polystyrene surface by thermal evaporation. This structure served as the zigzag

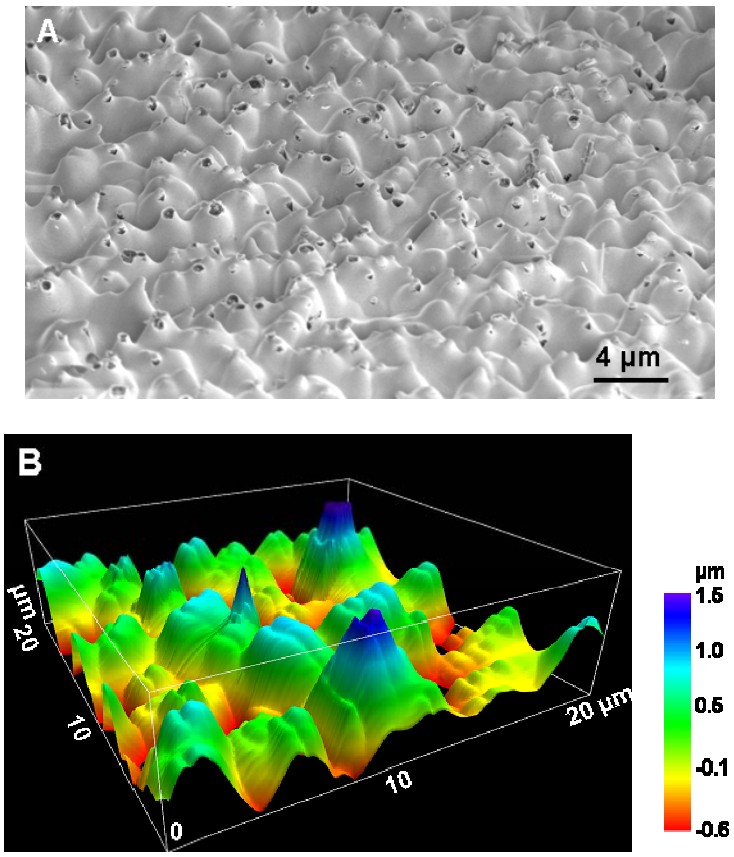

Figure 4.4 Self-assembled zigzag electrode. A. SEM image showing the Pt-coated electrode with randomly distributed cone-shape protrusions formed by agglomerated ZnO NWs imbedded in polystyrene. B. AFM image of the electrode surface showing the space between the "teeth" is ~2-3 µm and the depth of the gap is ~1-2 µm.

electrode for the NG, as shown in Figure 4.4A. Atomic force microscopy (AFM) imaging revealed a smooth yet bumpy surface with spaces between the teeth of ~2-3 μm in width and ~1-2 μm in depth (Figure 4.4B). These dimensions are ideal for inducing the mechanical deflection of NWs during NG operation. ZnO NWs used for the NG were grown on a GaN (0001) surface using the vapor deposition process (Figure 4.2).

4.3.3 Fabrication process of serially-connected hybrid cells (s-HC)

The s-HC model includes three main parts: ZnO NWs for DSSC, a zigzagged electrode, and the ZnO NWs for NG. First, vertically-aligned ZnO NWs ~10 μm high were grown on an ITO-coated glass substrate through hydrothermal approach as the electron collector for DSSC (Figure 4.5 a-1). Then, the NWs were immersed in a 0.5 mM solution of $(Bu_4N)_2Ru(dcbpyH)_2(NCS)_2$ (N719 dye, Dyesol) in ethanol for one hour (Figure 4.5 a-2).

The zigzag electrode was fabricated using ZnO NWs covered with polystyrene film, discussed in the previous section. Both sides of the zigzag electrode were coated with a thin layer of Pt as the anode of the DSSC (flat side) and the cathode of the NG (zigzagged side), respectively (Figure 4.5 b-3).

The DSSC was assembled by applying a 30-μm thick Bynel spacer between the ITO substrate and the silicon counter electrode. A liquid electrolyte was composed of a mixture of 0.5M LiI, 50mM I_2, and 0.5M 4-tertbutylpyridine in 3- methoxypropio- nitrile and infiltrated into the internal volume of the DSSC by the capillary effect (Figure 4.5 c). The DSSC was then heated to 120ºC to soften the spacer and to seal the edges to prevent the leakage of electrolytes.

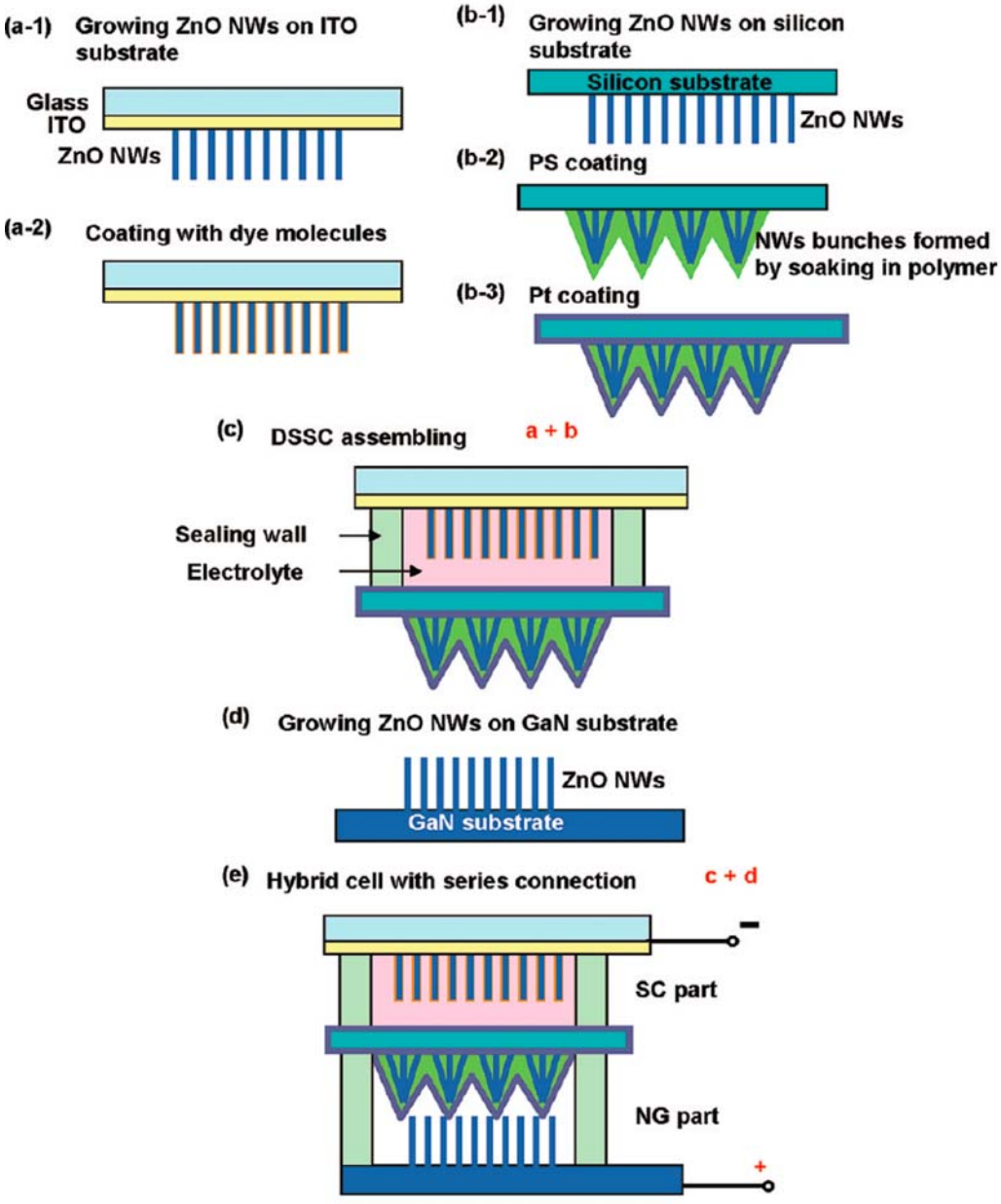

Figure 4.5 Fabrication procedures of a hybrid cell composed of a serially-connected SC and NG.

Vertically-aligned ZnO NWs growing on the GaN substrate were used for the NG component (Figure 4.5 d). Assembling the aligned ZnO NWs towards the Pt-coated NW bundles on the back side of the DSSC cell formed the complete hybrid cell (Figure 4.5 e). A thin layer of the flexible polymer wall was sandwiched between the substrate holding

the aligned ZnO NWs and the Pt-coated NW bundles so that they could move up and down under external agitation. The cathode of the NG and the anode of the DSSC were integrated on the same silicon substrate, which formed a serially-connected SC and NG. The continuous ZnO film deposited simultaneously with the NWs on the GaN substrate and the ITO glass served as the anode and the cathode of the hybrid cell, respectively.

A cross-sectional image of the entire s-HC is shown in the inset SEM image between Figures 4.6 b and c. It consists of three substrates from top to bottom: ITO, silicon, and GaN, respectively. The DSSC structure between the ITO and silicon substrates and the NG structure between the silicon and GaN substrates are presented in Figures 4.6 b and c, respectively. In the SC unit, the ZnO NWs were coated with dye molecules and separated from the counter electrode by a ~10 μm gap filled with electrolytes. In the NG unit, the ZnO NWs were approached and contacted by the top zigzag electrode, which periodically bent/deflected the NWs excited by the ultrasonic wave.

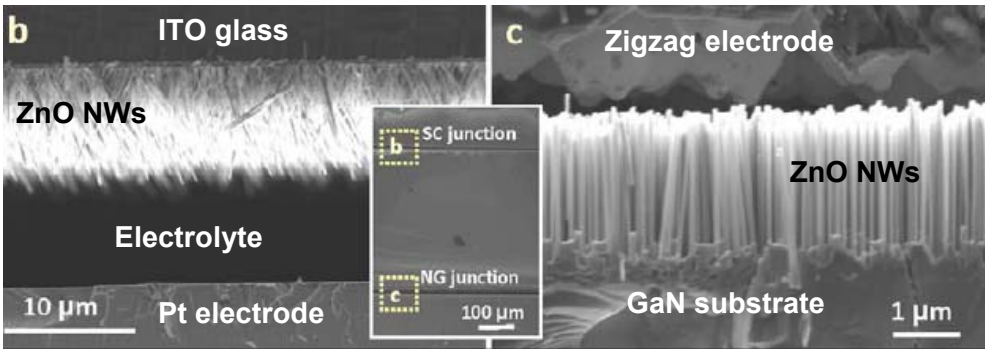

Figure 4.6 (b) SEM image of the SC unit. (c) SEM image of the NG unit. The SEM image inserted between B and C is a low-magnification cross-section view of the HC.

4.4 Electrical characterization methods of a hybrid cell

IV characterization is a typical method of characterizing solar cells as well as NGs. The packaged hybrid cell was affixed at the surface of the water in the cavity of an ultrasonic generator with the SC part exposed to sunlight and the NG part held in direct

contact with the water underneath, where ultrasonic waves of 41kHz were applied from the bottom, as shown in Figure 4.7. The hybrid cell was tested using AM 1.5G simulated sunlight.

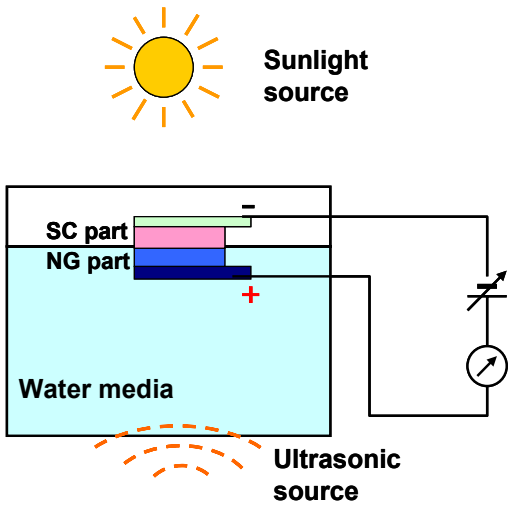

Figure 4.7 Experimental setup for IV measurement of hybrid cells

Meanwhile, an ultrasonic wave source that could be turned on and off independently was introduced through the bottom of the water cavity. IV curves were measured by serially connecting the HC to a synthesized function generator with a resistance of 50 Ω, sweeping from -1 to 1 V as an external load. The current signal was amplified by a preamplifier. Both current and voltage signals were converted through a BNC-2120 analogue-to-digital converter and recorded by a computer. The resistance of the hybrid cell was determined by recording the current signal under a steady 1V input. All of the measurements were performed at room temperature in air. All the IV data measured in this research has a confidence interval of 5%.

4.5 Performance of the s-HC and discussion

The performance of the SC was first characterized for the s-HC under simulated sunlight illumination without turning on ultrasonic waves. The SC exhibited an open circuit voltage ($U_{OC\text{-}SC}$) of 0.77 V and a short circuit current density ($J_{SC\text{-}SC}$) of 2.4 $mAcm^{-2}$. Although serially integrated with the NG, the fill factor of the SC reached 41% with an energy conversion efficiency of 0.76%. Compared with the work of other groups[69] the DSSC we made has a better Fill Factor, but a lower short circuit current, primarily because of the high resistance of the cell. However, the purpose of this paper is to demonstrate the approach of HC.

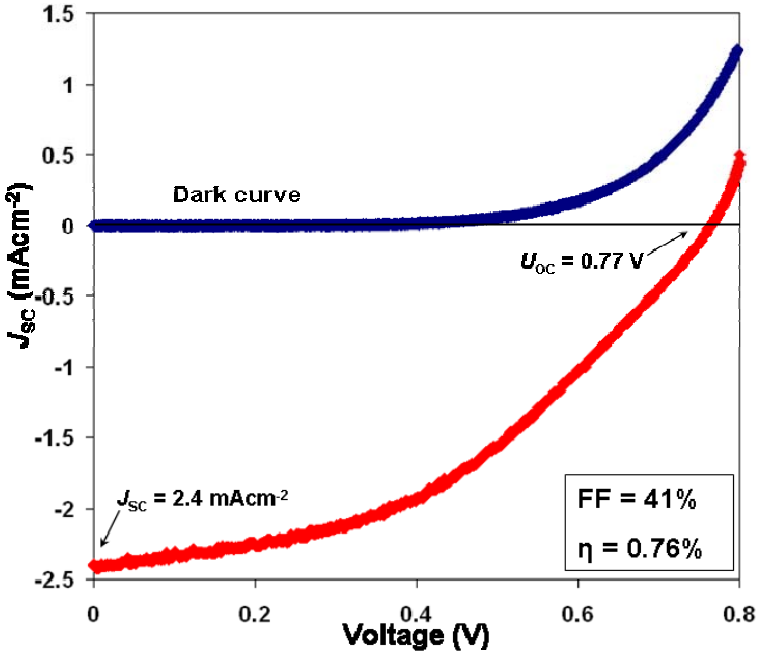

Figure 4.8 J-V (I-V) curve recorded from the SC part of a hybrid cell under simulated sunlight. The blue curve is the I-V curve when there is no sunlight illumination, which is a good calibration about the response of the SC. By illuminating with sunlight, the open circuit voltage is 0.77 V and the short circuit current is 240 μA (red curve). The fill factor of this DSSC is 41% at the operation point U=0.471V and I=170 μA. The energy conversion efficiency was calculated to be 0.76%.

The NG was tested by introducing ultrasonic waves through the water media without sunlight illumination; the corresponding J-V (or I-V) curve showed that the $U_{OC\text{-}NG}$ was

~0.01 V and the J_{NG} was ~1.1 μAcm^{-2} (Figure 4.10). Besides, a J-V curve of the NG was also recorded at near-zero-point region in dark condition by turning off sunlight and without applying ultrasonic waves (Figure 4.9). The curve passed right across the zero point, confirming that there was no contribution from the SC when only NG was characterized. The data provide evidence that the SC and NG units in the s-HC can work independently when only one type of energy source is available.

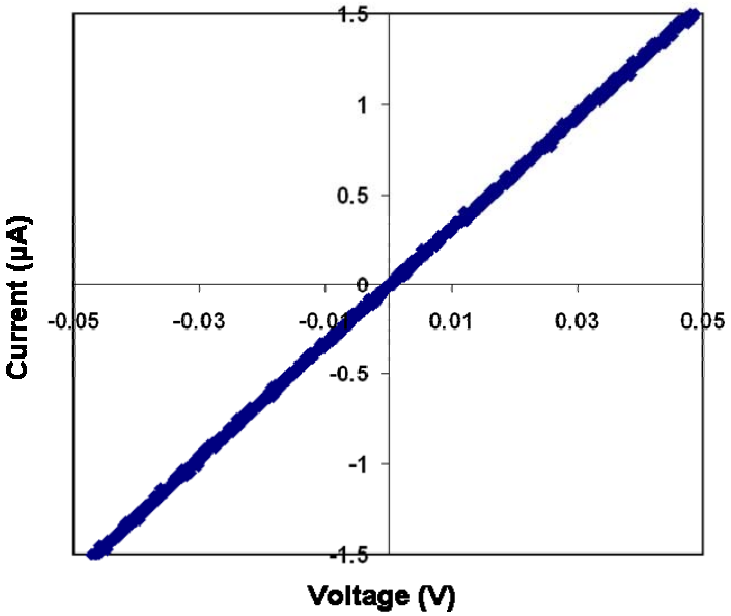

Figure 4.9 I-V curve recorded from the NG part of the hybrid cell at the near-zero-point region when both the sunlight and ultrasonic wave were turned off. The I-V curve came right across the zero point, showing no contribution from the SC part to the NG part when the hybrid cell was measured in the dark. This test is essential to exclude the influence of the SC to the characterization of the NG.

In order to demonstrate the ability of simultaneously harvesting solar and mechanical energies, we adjusted the SC output to a level comparable to that of the NG output by purposely reducing the intensity of the illuminating light because the output of the NG is much lower than that of the SC if one uses full sun illumination. When the sunlight source was on and the ultrasonic wave was off, the s-HC exhibited a U_{OC} of 0.591 V and a J_{SC} of 6.9 μAcm^{-2} (the blue curve in Figure 4.10). When both the

ultrasonic wave and sunlight were turned on, the U_{OC} reached 0.60 V while the J_{SC} remained at 6.9 μAcm^{-2} (the red curve in Figure 4.10). The output voltage of the s-HC differed by ~9 mV with or without the ultrasonic wave turned on, as shown by the expanded plot of U_{OC} in the inset of Figure 4.10, which is the same as the output voltage of the NG when the sunlight was off (Figure 4.10).

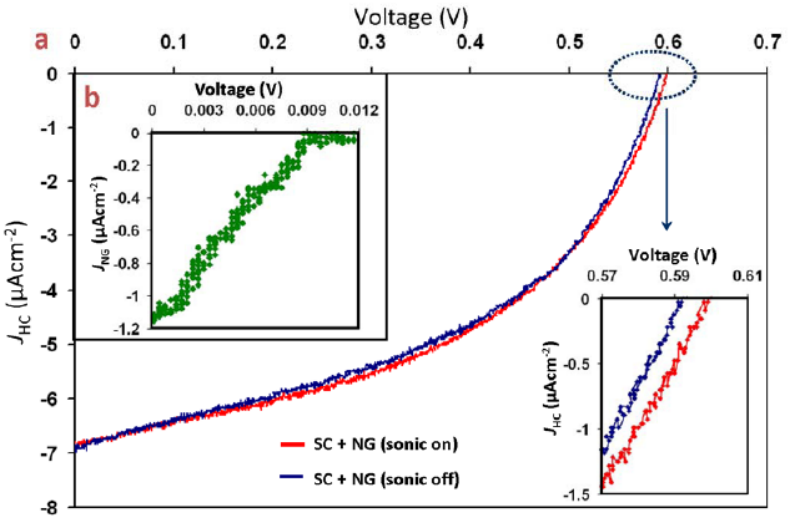

Figure 4.10 Performance of the HC composed of a serially-integrated SC and NG. (A) A comparison of the J-V characteristics of an s-HC when illuminated by simulated sunlight with (red curve) and without (blue curve) excitation of the ultrasonic wave. The inset is the expanded output of the open circuit voltage U_{OC} points around the axial cross point, showing an increment of U_{OC} for ~9 mV after turning on the ultrasonic waves. Both the SC and the NG were included in the measurement circuit. (B) J-V characteristic of the NG component when subjected to ultrasonic waves excitation, which was measured when both the SC and the NG were included in the measurement circuit but without sunlight.

To confirm that the increase in U_{OC} truly came from the NG unit, the J-V characteristics of the cathode and the anode of the SC unit were measured without including the NG unit in the measurement circuit. When the ultrasonic source was turned on and off, the J-V curves exhibited almost an identical trace (Figure 4.11). Particularly, the $U_{OC\text{-}SC}$ remained at the same point, as shown by the expanded plot of U_{OC} in the inset of Figure 4.11. Furthermore, the overall output of the s-HC can also be affected by the

internal resistance, which is mainly contributed by the NG unit. An exclusion of the NG from the measurement circuit resulted in a slight increase in the U_{OC} of the SC (see Figures 4.10 and 4.11).

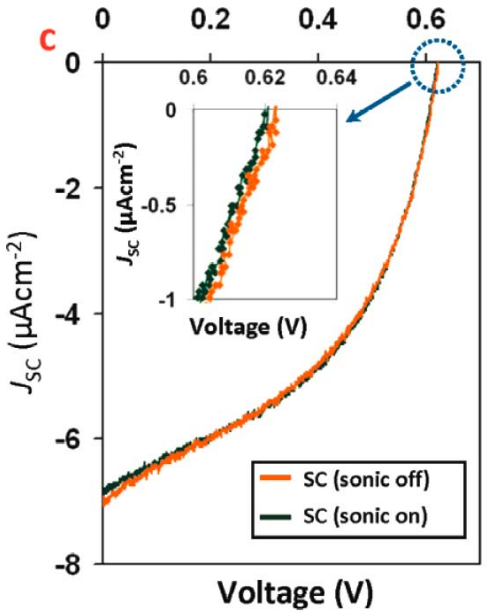

Figure 4.11 (C) J-V characteristic of the SC component alone, without including the NG component in the measurement circuit, when illuminated by a simulated sunlight with (green curve) and without (orange curve) turning on ultrasonic waves. The inset is an expanded plot around the U_{OC} points, showing almost no change in the U_{OC} by applying ultrasonic waves. The open circuit voltage U_{OC} point was not affected by the ultrasonic wave, simply ruling out the contribution made by the fluctuation in NG resistance to the performance of the SC.

To confirm that the increase in U_{OC} observed in Figure 4.10 for the s-HC resulted from the contribution made by the NG, the resistance of the NG was monitored when the ultrasonic wave was turned on and off (Figure 4.12). Although the resistance fluctuated for ~±2% at 28 kΩ, no step jump was observed at the points when the ultrasonic wave was turned on or off (Figure 4.12, inset). Therefore, the increase in U_{OC}/output power did not result from a resistance fluctuation of the NG in response to the ultrasonic wave.

The contribution of the NG to the output power of the s-HC is estimated by identifying the (J, V) point in the J-V curve at which the product of the current density and the voltage is maximized. When only the SC component operates under the dimmed

sunlight illumination condition, as shown in Figure 4.10, the optimum output power density was found to be 1.8945 μWcm^{-2} at 4.50μAcm^{-2} and 0.421 V. When both the SC and the NG operated simultaneously in a serial connection at the same operation current density of 4.50μAcm^{-2}, the voltage increased to 0.424 V, which produced a corresponding output power of 1.908 μWcm^{-2}. An increment in power (ΔP_{HC}) of 13.5 nWcm^{-2} was achieved after the NG was turned on, closely matching the optimal

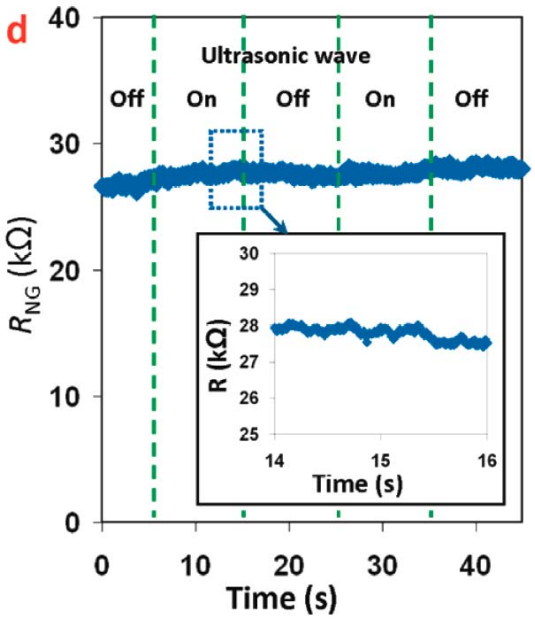

Figure 4.12 Resistance of the NG, measured by turning on and off the ultrasonic wave, to determine the effect of the ultrasonic wave on the stability of the resistance. The inset is an expanded plot of the resistance around a point when the ultrasonic wave was turned off, showing no visible trend in responding to the ultrasonic wave.

output power of the NG component ($U_{OC}J_{SC}$ ≈11 nWcm^{-2}). Therefore, the s-HC model successfully added up not only the open circuit voltage but also the power output from both the SC and the NG.

4.6 Working principle of the s-HC

The working principle of the s-HC can be explained using the electron energy band diagram shown in Figure 4.13. About the NG at the right-hand side, the maximum voltage output of the NG (V_{NG}) is determined by the difference between the Fermi level of the ZnO NWs (E_F, ZnO-NG) and that of the Pt that is

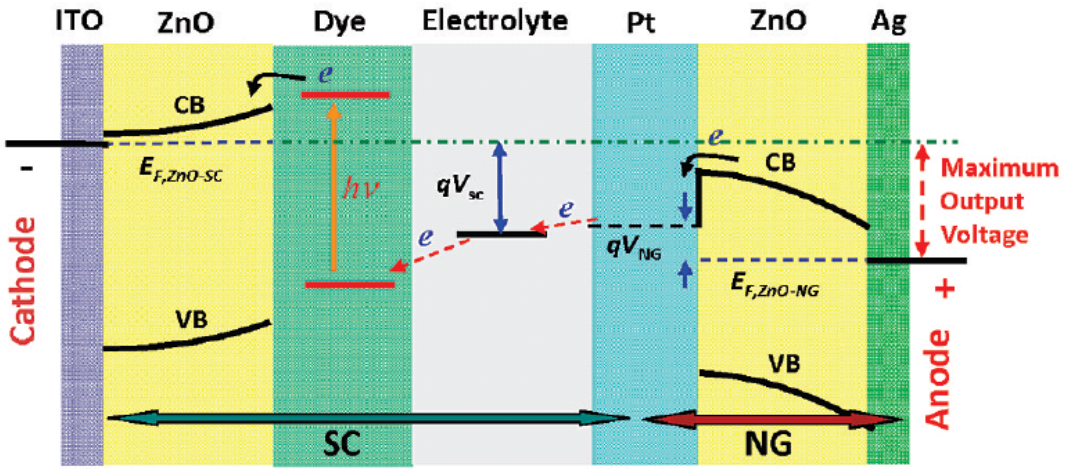

Figure 4.13 Electron energy band diagram of the s-HC, showing that the maximum output voltage is a sum of the voltages produced by the SC and the NG. The abbreviations are CB (conduction band), VB (valence band), and E_F (Fermi level).

"transiently" raised by the electrons "pumped in" under the driving force of the piezoelectric potential from the NWs and Ag bottom electrode[19]. Once subjected to mechanical deformation under the driving force of ultrasonic waves, for example, a negative local piezoelectric potential is created on the compressive side of an NW, which moves the charge carriers (e.g., electrons for n-type ZnO) located on the NW side close to the Pt-ZnO junction and injects them into the Pt electrode, owing to the forward-biased Schottky barrier[82]. These charge carriers continue to transport in the electrolyte[67] through a redox couple process into the SC. The left-hand side of Figure 4.13 shows the band structure of a ZnO-based DSSC where the maximum voltage output[83] (V_{SC}) is dictated by the gap between the Fermi level of the ZnO (E_F, ZnO-SC) and the electrochemical potential of the electrolyte[67]. When a light is applied on the glass side of the HC,

electrons are excited to the high energy state of the dye molecules, subsequently transferred to the conduction band of ZnO and then collected by ZnO NWs, and finally exported through the cathode at the energy of the Fermi level E_F, ZnO-SC. In the entire s-HC, the electron energy is promoted twice by the NG and the SC so that the overall maximum output voltage is the sum of V_{SC} and V_{NG}.

4.7 Fabrication of the hybrid cell with a parallel-connected SC and NG (p-HC)

In addition to the s-HC, an A HC composed of a parallel-integrated SC and NG (p-HC) that raises the output current has been designed. As schematically shown in Figure 4.14, the anodes of the DSSC (the Pt electrode) and the NG (the bottom layer of the aligned ZnO NWs) were integrated on a single piece of silicon substrate by around surface Pt coating. The anode of the NG is a Pt-coated zigzag electrode fabricated by etching silicon. The cathodes of the DSSC and the NG were connected by external wiring; thus, this device can be simplified as a parallel-connected SC and NG (see the right-hand side of Figure 4.14).

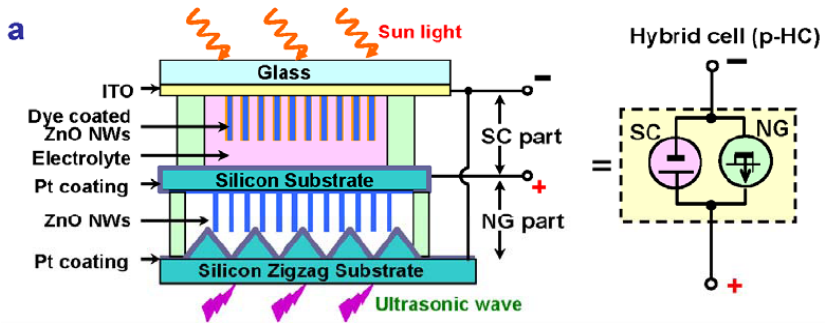

Figure 4.14 Design of a hybrid cell composed of a parallel-integrated SC and NG that raises the output current.

This design also includes three parts: ZnO NWs for DSSC, ZnO NWs for NG, and a zigzag electrode. First, vertically-aligned ZnO NWs were grown on the ITO-coated glass

substrate and coated with dye molecules using the same method as for s-HC. The NG part was built on the vertically-aligned ZnO NW array grown on a silicon substrate through the hydrothermal approach or on the GaN substrate using the vapor deposition method. The main difference from the s-HC is that on the back of the substrate, a thin layer (200 nm) of platinum was deposited. The Pt film also covered the side of the substrate and connected the ZnO buffer layer on the NW side so that the roots of all the ZnO NWs were electrically connected to the back electrode.

The DSSC was assembled between the ITO substrate and the back side of the substrate covered with grown NWs in front, where the liquid electrolyte was infiltrated to fill the gap. The Pt-coated silicon substrate with a zigzagged surface and the ITO glass were connected and served as the cathode of the NG and the p-HC. The Pt-coated silicon substrate with ZnO NWs on the other side served as both the common anode of the DSSC and the NG, and also the anode of the p-HC.

4.8 Fabrication process of the hybrid cell with a parallel-connected SC and NG (p-HC)

The fabrication procedures of a hybrid cell are schematically shown in Fig. 12. First, vertically-aligned ZnO NWs were grown on an ITO-coated glass substrate through a hydrothermal approach as the electron collector for the DSSC (Figure 4.15 a-1). The height of the NWs was controlled in the range of 3-10 μm. The NWs were then coated with dye molecules by immersing the substrate in a dye solution for one hour (Figure 4.15 a-2). The NG part was built on a vertically-aligned ZnO NW array that was grown on a silicon substrate through the hydrothermal approach or on a GaN substrate through the vapor deposition method. The height was about 2 μm. A thin layer of Pt was deposited on the back of the substrate. The Pt film has to cover the side of the substrate and connect the ZnO buffer layer on the NW side so that the bottom of all the ZnO NWs were electrically connected to the back electrode (Figure 4.15 b-2). The DSSC can thus

be assembled by applying a 40-micon thick spacer as a sealing wall between the ITO substrate and the flat side of the silicon substrate, where liquid electrolyte was infiltrated to fill the gap (Figure 4.15 c). Here Pt-coated silicon substrate with a zigzagged surface (Figure 4.15 d) is used as the cathode of the NG part so as to form a p-HC (Figure 4.15 e). The Pt-coated silicon substrate with ZnO NWs on the other side serves as both a common anode of both the DSSC and the NG, and also the anode of the p-HC. The ITO substrate and the Pt-coated zigzag substrate are the cathode of the DSSC and the NG, respectively, and they can be electrically connected and used as the cathode of the p-HC.

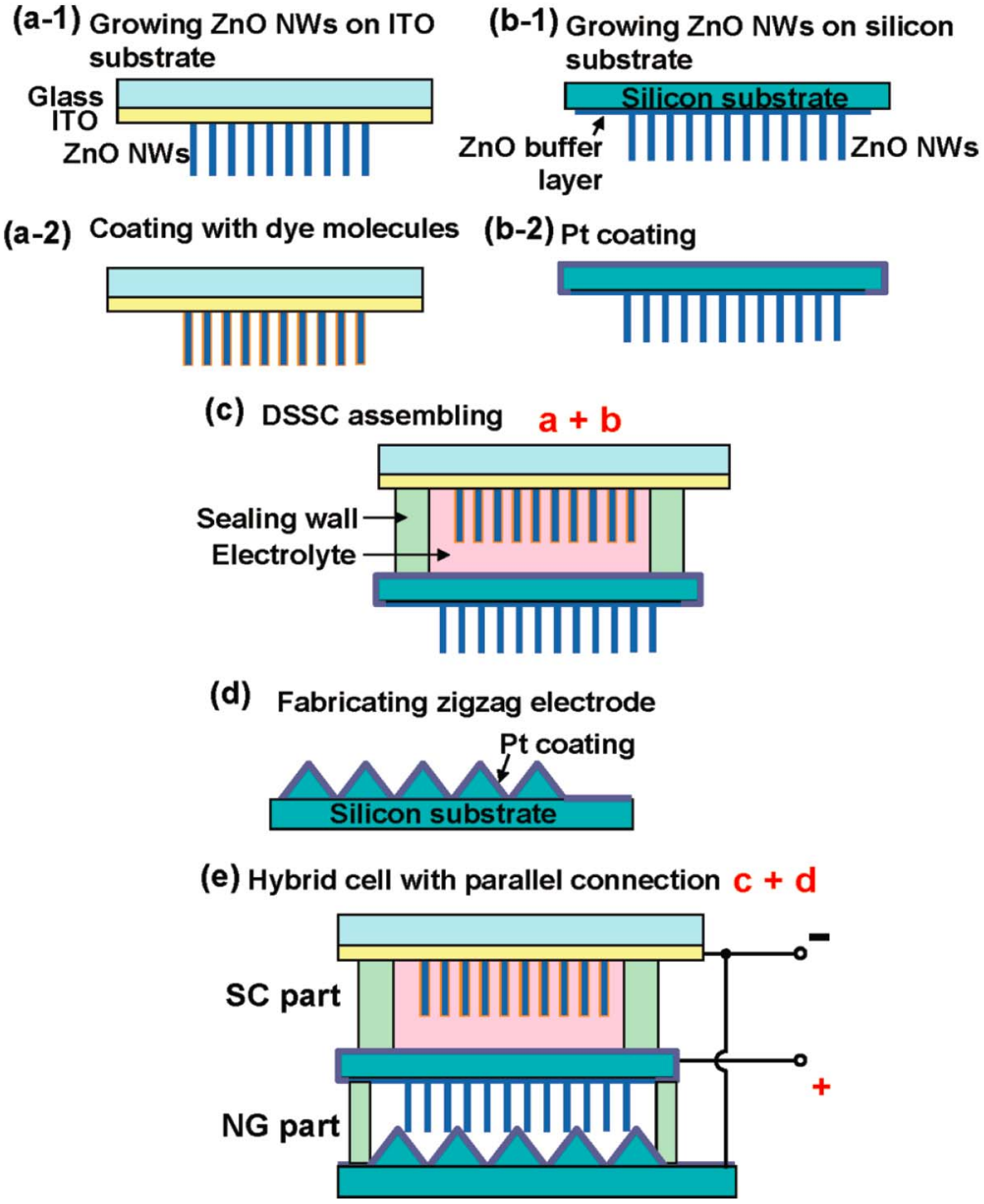

Figure 4.15 Fabrication procedures of a hybrid cell composed of a parallel-connected SC and NG.

4.9 Working principle of the hybrid cell with a parallel-connected SC and NG (p-HC)

The working principle of a p-HC is illustrated in Fig. 3B. As discussed previously, for an NG working independently, the output voltage (V_{NG}) is determined by the shift in the transient Fermi level of the Pt electrode ($E_{F, Pt\text{-}NG}$) in reference to that of the ZnO NW ($E_{F, ZnO\text{-}NG}$) once the electrons are pumped in by piezoelectric potential, as shown in the red dashed box on the top right-hand side of Figure 4.16. When the NG is parallel integrated/connected to an SC, the band structure of which is given in the green dashed box on the top left side of Fig. 3B, Fermi levels will realign at the anode and cathode, respectively. When the Pt electrode of the NG is integrated with the ITO electrode of the SC, extra electrons are fed from the SC side to the NG side because the SC side has a higher Fermi level. However, these electrons cannot flow through the NG because of the existence of a Schottky barrier at the interface between the Pt electrode and ZnO NW. Instead, they tend to accumulate on the Pt side close to the Schottky barrier, resulting in a rise in the local Fermi level to $E'_{F, Pt\text{-}NG}$ until it matches that of the cathode of the SC, $E'_{F, Pt\text{-}NG} = E_{F, ZnO\text{-}SC}$. However, the connection of the two anodes leads to an alignment of the Fermi levels on the anode side: $E_{F, ZnO\text{-}NG} = E_{F, Pt\text{-}SC}$. The resulting voltage output of the p-HC is

$$V_{p\text{-}HC} = V_{SC} = V'_{NG} = E'_{F, Pt\text{-}NG} - E_{F, ZnO\text{-}NG}$$

This relationship indicates that the output voltage of the NG can rise to the same level as that of the SC under the parallel integration configuration possibly due to the existence of a reversely- biased Schottky barrier in the NG, which has a high enough resistance that it blocks the flow through of the electrons fed by the SC. This discussion holds if the barrier height is higher than the SC output; otherwise, the SC output will break through the NG. The electron affinity (E_a) of bulk ZnO is 4.5 eV, the work function of bulk Pt is 6.1 eV, and the barrier height is estimated to be ~1.6 eV. In reality, the typical voltage output of a DSSC is ~0.7-0.8 V. Therefore, parallel-integrating an SC to

an NG may effectively boost up the output voltage of an NG from several millivolts to several hundred millivolts.

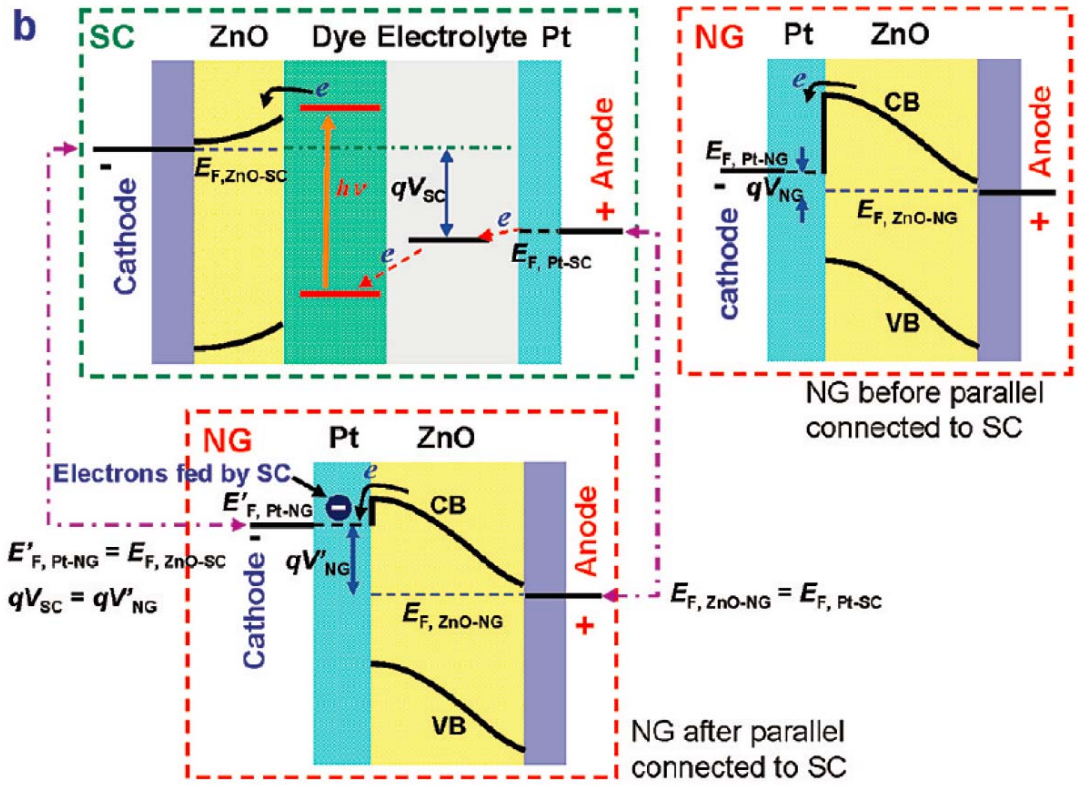

Figure 4.16 Electron energy band diagram of the p-HC and its working principle. The top two diagrams are the band structures of the SC and the NG before parallel integration, respectively. The bottom diagram is the band structure of the NG after being parallel integrated to the HC with a realignment of Fermi levels at the cathode and anode, respectively. The maximum voltage output of the p-HC is approximately the voltage output of the SC.

4.10 Performance of the hybrid cell with a parallel-connected SC and NG (p-HC)

The proposed working principle for the p-HC was confirmed by J-V characterization under the same experimental setup as for the s-HC (Figure 4.7). When a p-HC was measured under simulated sunlight without the application of ultrasonic waves, the U_{OC} and J_{SC} were found to be 0.102 V and 44 μAcm^{-2}, respectively (the blue curve in Figure 4.17a). Note that the output voltage for the SC is deliberately kept low by lowering the

sunlight intensity in order to enhance the relative contribution from the NG. When ultrasonic waves were applied together with sunlight, its J-V characteristic shows the same shape but with a slight increase in J_{SC} (the red curve in Figure 4.17a). Expanded plots of U_{OC} and J_{SC} (inset of Figure 4.17a) reveal that the J_{SC} increased by ~1.5 μAcm^{-2}, while no change in U_{OC} occurred. By turning off the light, the p-HC produced an U_{OC} of ~7 mV and an J_{SC} of ~3 μAcm^{-2} (Figure 4.17b), which are the outputs of the NG. Since the output voltage of the SC unit is ~0.1 V, which is significantly lower than the Schottky barrier height of Pt/ZnO, the promotion effect kept the overall output voltage of the p-HC the same as that of SC but with an increased current output, showing the feasibility of raising the output voltage of the NG using the "promotion effect" of the SC. Note that the increment of J_{SC} is only about half of the output of the NG, which is possibly due to the small fraction of charges fed from the SC into the NG and accumulated in the Pt electrode next to the Schottky barrier to raise its voltage, corresponding to the process illustrated in the lower diagram of Figure 4.16. The flow direction of the current fed back is against that produced by the NG.

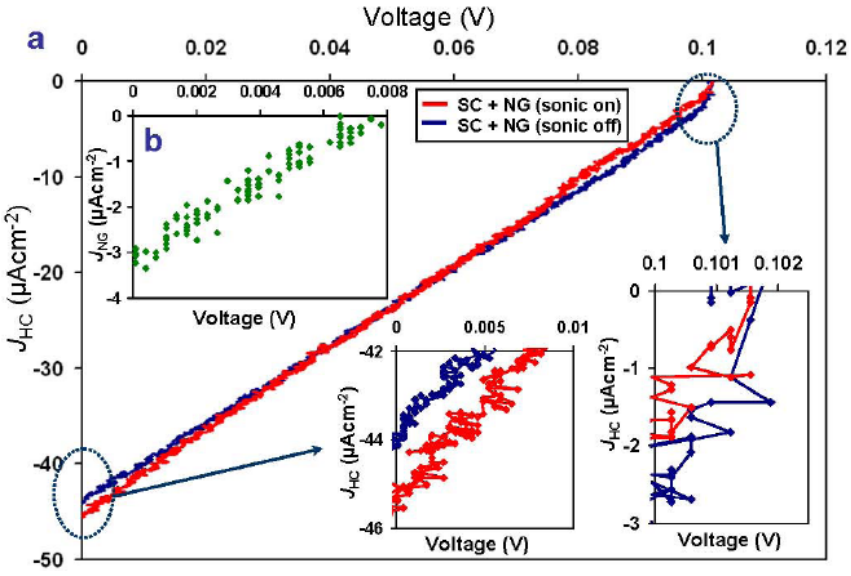

Figure 4.17 Performance of the HC composed of the parallel-integrated SC and NG.

The output voltage for the SC was deliberately kept low by lowering the intensity of the sunlight in order to enhance the relative contribution from the NG. When ultrasonic waves were applied together with sunlight, its J-V characteristic exhibited the same shape but with a slight increase in J_{SC} (the the red curve in Figure 4.17). Expanded plots of U_{OC} and J_{SC} (the inset of Figure 4.17) reveal that the J_{SC} increased by ~1.5 μAcm^{-2} while no change occurred in U_{OC}. By turning off the light, the p-HC produced an U_{OC} of ~7 mV and a J_{SC} of ~3 μAcm^{-2} (Figure 4.17), which are the outputs of the NG. Since the output voltage of the SC unit was ~0.1 V, which was significantly lower than the Schottky barrier height of Pt/ZnO, the promotion effect kept the overall output voltage of the p-HC the same as that of SC, but with an increased current output, showing the feasibility of raising the output voltage of the NG using the "promotion effect" of the SC. Note that the increase in J_{SC} is only about half that of the NG output, which could have occurred because a small fraction of charges were fed from the SC into the NG and accumulated in the Pt electrode next to the Schottky barrier, raising its voltage.

To have a comparison of HCs performance with different types of energy, Table 3.2 has summarized the values according to the corresponding condition.

Table 3.2 Hybrid cell output comparison with different types of energy

	S-HC		P-HC	
	Uoc (mV)	Isc (μAcm^{-2})	Uoc (mV)	Isc (μAcm^{-2})
Only light on	591	6.9	102	44
Only vibration on	10	1.1	7	3
Both light and vibration on	600	6.9	100	45.5

CHAPTER FIVE

SECOND GENERATION OF HYBRID CELL

The prototype of the nanowire-based hybrid cell, demonstrated to harvest both solar and mechanical energies, uses a Dye-sensitized Solar Cell (DSSC) and a piezoelectric Nanogenerator (NG). However, as a result of the encapsulation problem posed by the use of the liquid electrolyte[6] in conventional DSSC, solvent leakage and evaporation are two major obstacles, so the present hybrid cell is actually a back-to-back physical integration of an NG and a DSSC on the same substrate, which may limit its performance. The next two chapters will describe the second generation of hybrid cell and the enhancement of reliability and performance on hybrid cells. First, we developed an innovative approach that convolutes a solid state dye-sensitized solar cell[12, 84, 85] and an ultrasonic wave-driven piezoelectric NG into a single compacted structure for concurrently harvesting solar and mechanical energies. With the introduction of a solid electrolyte to the DSSC part, we improved the reliability of the HC over that of the liquid-based cell.

5.1 Design of the compacted hybrid cell[86]

The second generation of hybrid cell, called the compacted hybrid cell (CHC) , convolutes the roles played by nanowire arrays so that it simultaneously performs their functionalities in an NG and a DSSC. The main frame structure consists of two sets of ZnO nanowire arrays placed teeth-to-teeth (Figure 5.1), as previously demonstrated for the fiber-based NG[87]. The DSSC follows the template in which the nanowire array is at the top, which is coated with a layer of metal so that it can serve as the electrode for the

NG. The nanowire array at the bottom acts as a piezoelectric structure that converts mechanical energy into electricity. The sunlight illuminates the device from the top, and

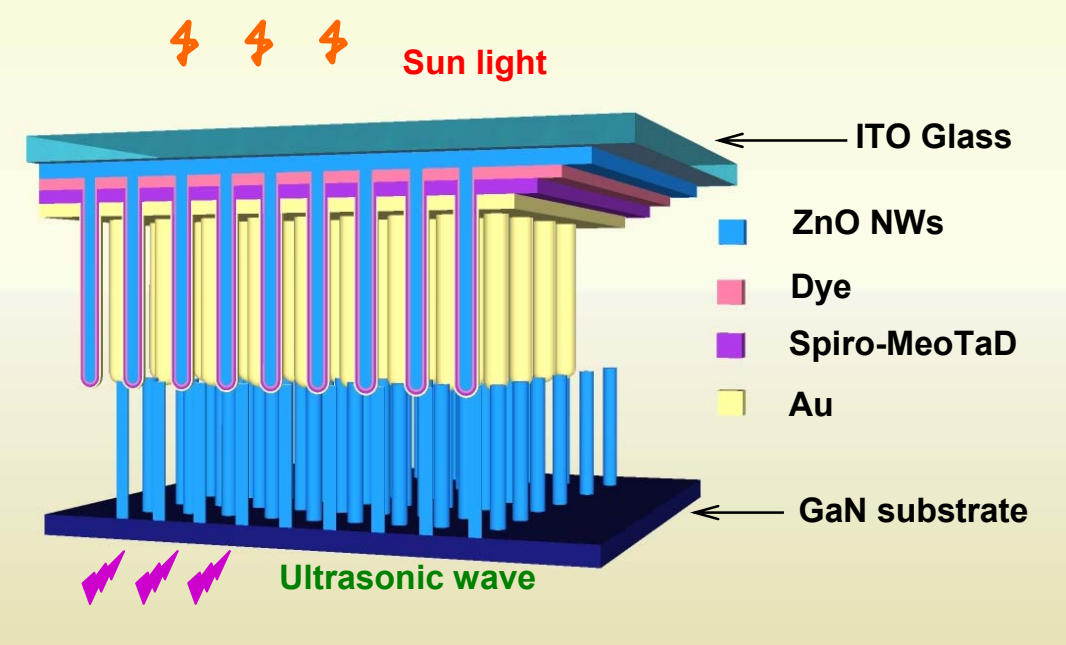

Figure 5.1 Design of the compacted hybrid cell (CHC) structure composed of a dye-sensitized solar cell (SC) and a nanogenerator (NG). Schematic illustration of a CHC, which is illuminated by sunlight from the top and excited by an ultrasonic wave from the bottom. The ITO layer on the DSSC part and the GaN substrate are defined as the cathode and the anode of the CHC, respectively.

the ultrasonic wave is applied from the bottom. The convoluted HC with DSSC and NG in a series is presented schematically in Figure 5.2.

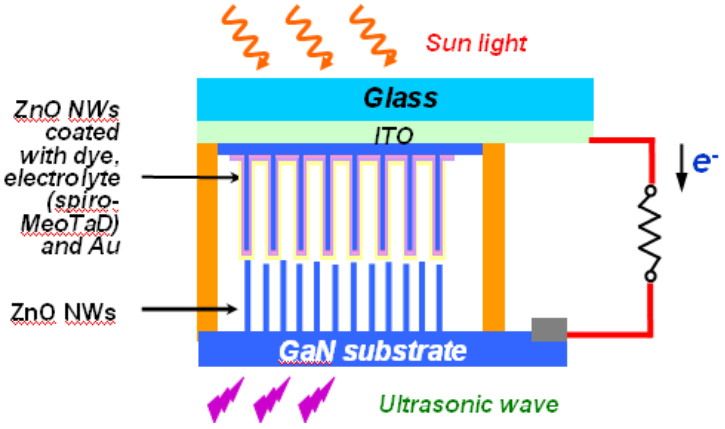

Figure 5.2 Schematic structure of a CHC.

5.2 Fabrication of the CHC

To fabricate the solid state DSSC, the vertically-aligned ZnO nanowires (NWs) were grown on an ITO-coated glass substrate (CB-40IN-0107, 4-8Ω, Delta Technologies, Ltd.) using a hydrothermal method. The substrate was first cleaned by standard acetone/ethanol/IPA/Di water sonication and a thin film of ZnO 200 nm thick was deposited by magnetron RF sputter. Then, the ZnO NWs were synthesized by floating the substrate on the nutrient solution surface, which is composed of 5 mM 1 to 1 ration of $Zn(NO_3)_2$ and hexamethylenetetramine at 80°C for 24h. After rinsed with acetone, the NWs were immersed in a (0.5mmol L^{-1}) sensitized solution of $(Bu_4N)_2Ru(dcbpyH)_2(NCS)_2$ (N719 dye) in ethanol for 1h for dye loading. Then an amorphous organic hole-transport material 2,2',7,7'–tetrakis(N,N-di-p-methoxyphenyl-amine) 9,9'–spirobifluorene (OMeTAD) was spun on the dye-sensitized ZnO NWs at 2000rpm for 60s and baked at 100°C to eliminate the organic solution.

As shown schematically in Figure 5.3, a cone-shaped surface was created. A continuous gold (Au) thin film (60 nm thick) coating resulted in the formation of a cone-shaped electrode required for the NG, described next. Figure 5.4 shows the scanning electron microscopy (SEM) imaging of the cone-shaped surface in which the space between the cones was 1-2μm wide.

For NG fabrication, ZnO NWs (Figure 5.5) used for the NG were grown on a GaN (0001) surface using a high-temperature vapor deposition process[44] to achieve uniform polarity. Figure 5.6 shows the scanning electron microscopy (SEM) imaging of ZnO NWs on GaN. The nanowires were ~2-3μm long and the interspacing between the nanowires was 400-700 nm. By stacking the two sets of nanowire arrays inter-digitatively face-to-face, the Au-coated cone-shaped electrode on the top served as a "zig-zag" electrode for mechanically triggering the nanowires located at the bottom (Figure 5.1). This functional NG will be driven by ultrasonic wave.

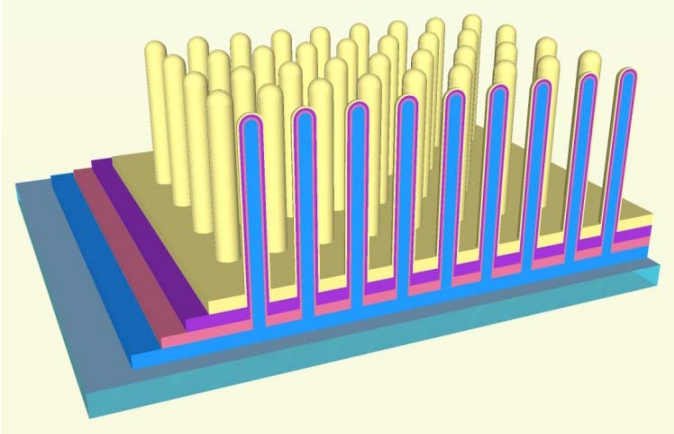

Figure 5.3 Schematic illustration of a solid state DSSC.

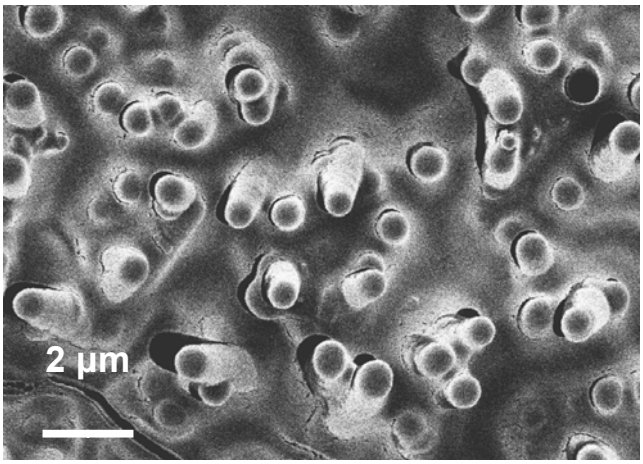

Figure 5.4 Top view SEM image of the DSSC.

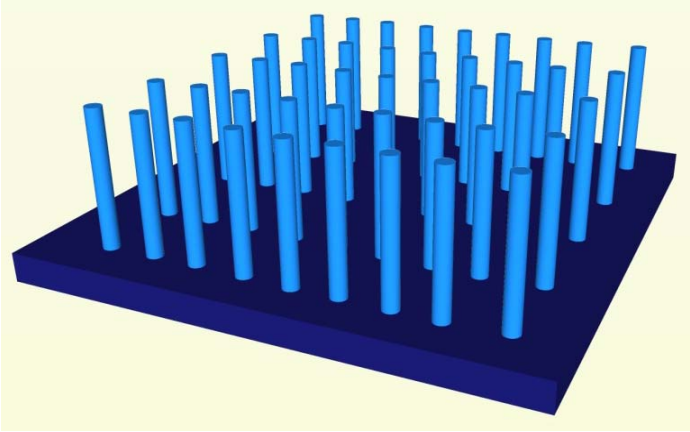

Figure 5.5 Schematic illustration of a vertically-aligned ZnO nanowire array grown on a GaN substrate.

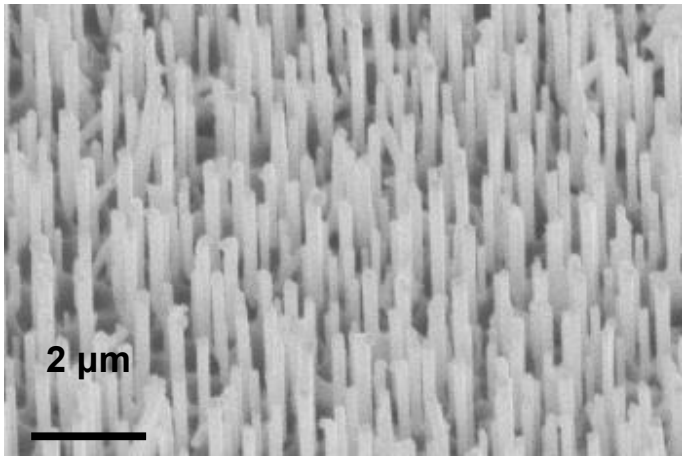

Figure 5.6 SEM image of the ZnO nanowire array through the high temperature vapor deposition method for the NG.

The "convolution" of the DSSC and NG in a series forming a CHC is presented in Figure 5.2. Here ITO serves as the cathode while the silver (Ag) paste in contact with GaN serves as the anode in this configuration. After connected to the output wires, the entire CHC, except for the window of the DSSC, was sealed and packaged by epoxy resin to prevent infiltration of any liquid.

5.3 Working principle of the CHC

The working principle of the CHC is presented by the electron energy band diagram (Figure 5.7). The electrons were promoted by piezoelectric potential and photovoltaic potential consecutively through the two devices. The maximum output voltage achievable is the difference between the Fermi level of the ZnO NWs in the DSSC ($E_{F,\ ZnO\text{-}SC}$) and that of the ZnO NWs in the NG ($E_{F,\ ZnO\text{-}NG}$). The maximum output is a summation of the output voltages of the NG and DSSC. In the NG section, the gap between the Fermi level of the ZnO NWs ($E_{F,\ ZnO\text{-}NG}$) and that of the Au determined the maximum voltage output of the NG (V_{NG}). The Au-ZnO junction

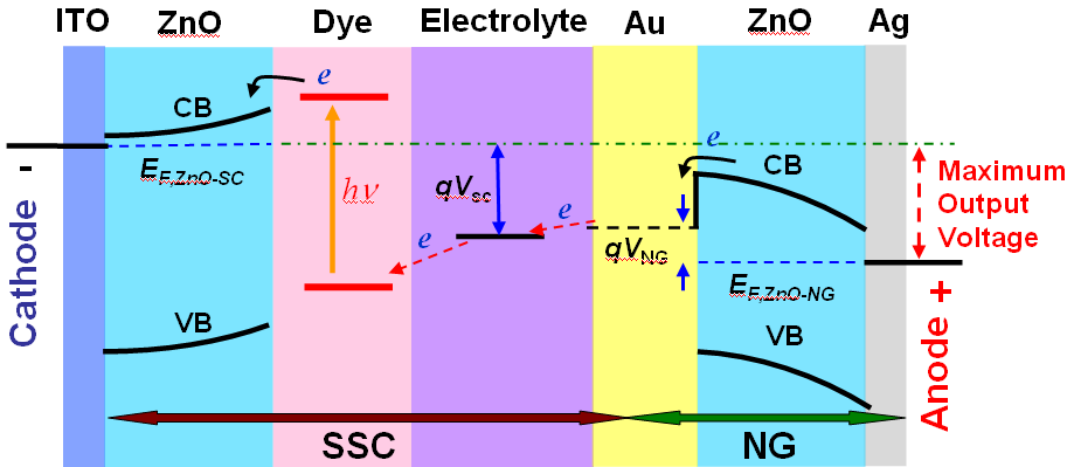

Figure 5.7 Electron energy band diagram of the CHC, showing that the maximum output voltage is a sum of those produced by DSSC and NG. The abbreviations are: CB (conduction band), VB (valence band), and E_F (Fermi level).

forms a Schottky contact because Au has a work function of 4.8 eV, which is greater than the electron affinity of ZnO (4.5eV), which serves as a "gate" that blocks the back flow of electrons. When the Au electrode slowly pushed an NW like an AFM tip, a strain field was created across the NW width, with the outer surface in tensile strain and the inner surface in compressive strain. The piezoelectric potential at the compressive side of the nanowire sets the Schottky contact as forward biased and drives the electrons across the Au-ZnO junction. Through an electron-transfer process[67], these charge carriers continue to be transported in the solid state electrolyte into the DSSC. In the DSSC section of Figure 5.7, the maximum voltage output (V_{SC}) is dictated by the difference between the the Fermi level of the ZnO ($E_{F,\ ZnO\text{-}SC}$) and the electrochemical potential of the electrolyte[67]. Visible-light absorption by the dye sensitizer excites electron transfer to the conduction band of ZnO. The electron injection from the excited sensitizer into ZnO is followed by the regeneration of the dye sensitizer by the electrons from OMeTAD. The electrons in the conduction-band of ZnO and the holes in the electrolyte are separated and subsequently transported to the contact electrodes.

5.4 Performance of the CHC and discussions

Both the DSSC and NG units of the CHC can work independently and conjunctionally. The CHC was characterized by affixing it on the water surface in an ultrasonic generator cavity with the transparent DSSC side facing the sunlight source and the NG side in direct contact with the water underneath, where an ultrasonic generator with a frequency of ~41 kHz was applied from the bottom side (Figure 5.1). J-V curves were recorded for the CHC, the DSSC, and the NG. The short circuit current was measured by serially connecting the CHC to a DS345 30MHz- synthesized function generator (Stanford Research Systems) with a resistance of 50Ω sweeping from -1 to 1V as an external load. The current signal used a DL 1211 preamplifier (DL instruments). All of the signals were converted through a BNC-2120 analog-to-digital converter (National Instruments) and recorded by a computer. The photovoltaic performance of the DSSC in the CHC was first characterized under simulated sunlight illumination (AM 1.5G simulated sunlight 300 W model 91160, Newport) without applying an ultrasonic wave. The open circuit voltage ($U_{OC\text{-}SC}$) was 0.42 V, and the short circuit current density ($J_{SC\text{-}SC}$) was 0.25 $mAcm^{-2}$ (Figure 5.8). The fill factor of the DSSC reached 30.6%, which corresponded to an overall energy conversion efficiency of 0.03%. These values were comparable to the present ZnO-based solid state DSSC reported.

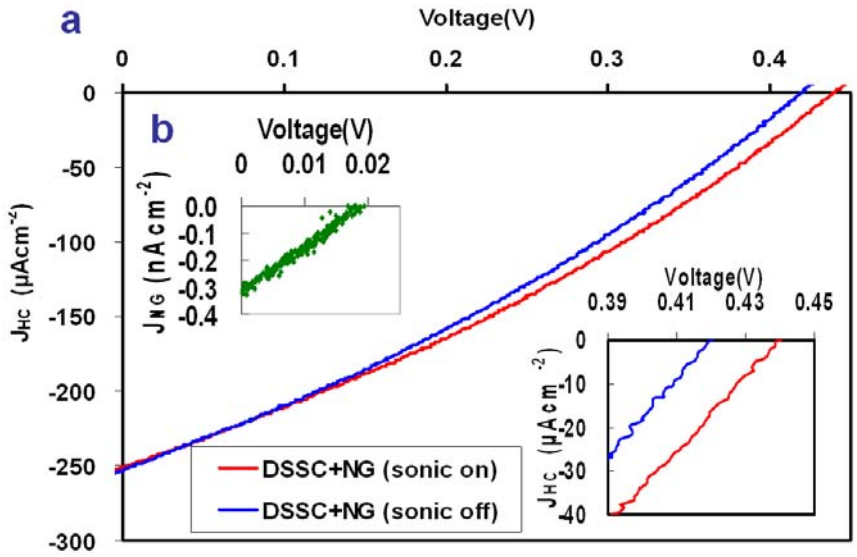

Figure 5.8 (a) A comparison of the J-V characteristics of a CHC when illuminated by simulated sunlight with (red curve) and without (blue curve) turning on the ultrasonic wave excitation. Inset is an expanded output of the open circuit voltage U_{OC} points around the axial cross point, showing an increment of U_{OC} for ~19 mV after ultrasonic waves are turned on; **(b)** the J-V characteristic of the NG when subjected to excitation of the ultrasonic wave, but with no sunlight.

The NG was characterized by the introduction of ultrasonic waves through water media without sunlight illumination; the corresponding J-V curve showed that the $U_{OC\text{-}NG}$ was ~0.019 V and the I_{NG} was ~0.3 pA cm^{-2} (the left inset of Figure 5.8).

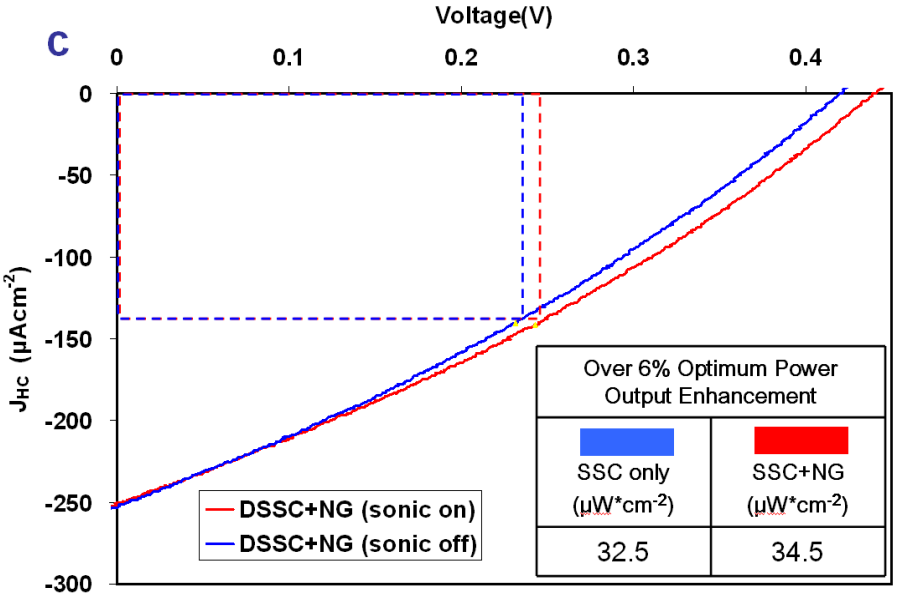

Figure 5.9 A comparison of the power output J-V characteristics of a CHC. The rectangular area is the optimal power output for the CHC.

A J–V curve of the NG (Figure 5.10) was recorded when the sunlight was turned on and off. The corresponding Uoc-NG showed no change, indicating no contribution from the SC to the NG when only the NG was being characterized. Furthermore, an I-V curve of the NG was also recorded at the near-zero point region when the device was in a dark condition without ultrasonic waves have been applied. As shown in Figure 5.11, the curve passed right across the zero point. The data prove that the DSSC and NG units in the CHC can work independently when only one type of energy source is available. A ZnO-based solid state DSSC was purposely chosen because the output of the DSSC is comparable to that of the NG. However, it can be largely improved by using a TiO_2-based solid state DSSC.

To demonstrate the technological feasibility of the CHC for simultaneously harvesting solar and mechanical energies, we measured the J-V curve on the CHC under various conditions. When the full sunlight source was turned on and the ultrasonic wave source was turned off, the CHC exhibited a U_{OC} of 0.415 V and J_{SC} of 252 μAcm^{-2} (blue curve in Figure 5.8). When both the

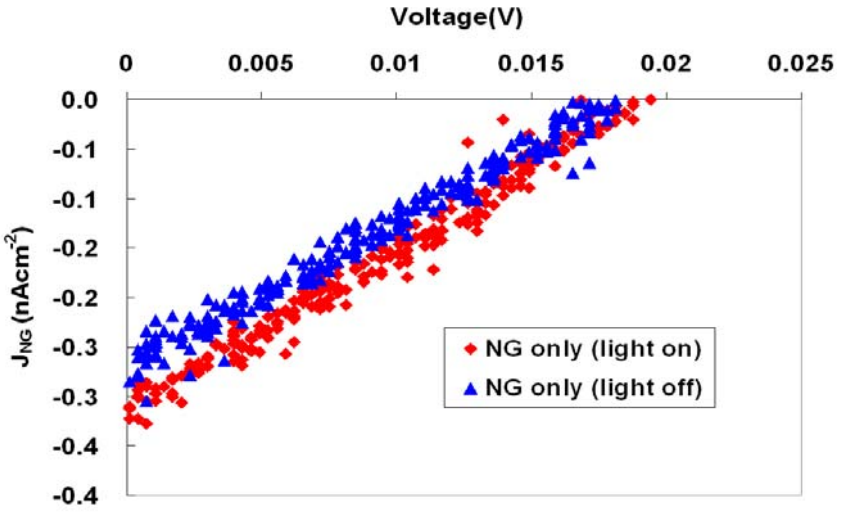

Figure 5.10 The J-V characteristic of the NG, without the DSSC unit in the measurement circuit, when excited by ultrasonic waves with (red curve) and without (blue curve) simulated sunlight turned on. It shows almost no change in the U_{OC} of the NG, even when the simulated sunlight was turned on or off.

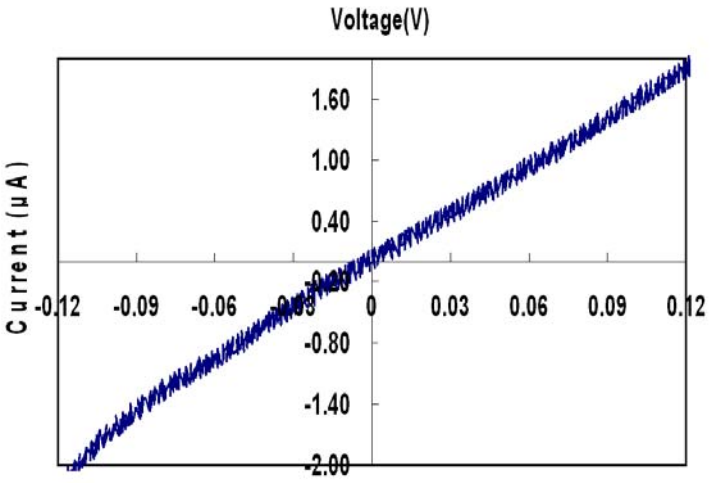

Figure 5.11 I-V curve recorded from the NG part of the hybrid cell at the near-zero-point region when both the sunlight and the ultrasonic wave were turned off. The I-V curve came right across the zero point, showing no contribution from the DSSC to the NG when the hybrid cell was measured in the dark. These tests were essential if the influence of the DSSC on the characterization of the NG was to be excluded.

ultrasonic wave and the sunlight were turned on, the U_{OC} reached 0.433 V while the J_{SC} remained at 252 μAcm^{-2} (the red curve in Figure 5.8). The output voltage of the CHC showed a 19 mV difference when the ultrasonic wave was turned on and off, as shown by the expanded plot of U_{OC} in the right-hand inset of Figure 5.8, which represents only the output voltage of the NG when the sunlight was turned off (Figure 5.9).

The main advantage of this new CHC is that, unlike our previous hybrid cell[79], the new CHC is a solid state device without a liquid electrolyte, and two parts are convolutedly designed in a single compact cell. In particular, the possibility of solvent leakage and evaporation from the DSSC is no longer an issue. Moreover, the single compact design makes it a truly single device with the ability to harvest both solar and mechanical energy.

To further confirm that the increase in U_{OC} is coming from the NG unit, another set of J-V characteristics of the cathode and the anode of the DSSC unit was measured without the inclusion of the NG unit in the measurement circuit. The performance of the CHC was shown in the J-V curves (Figure 5.12a) with the NG performance in Figure 5.12b. By turning on and off the ultrasonic waves, the J-V curves exhibited a nearly

identical trace (Figure 5.12c). In particular, the $U_{OC\text{-}SC}$ stayed at the same point, as shown by the expanded plot of U_{OC} in the Figure 5.12c inset.

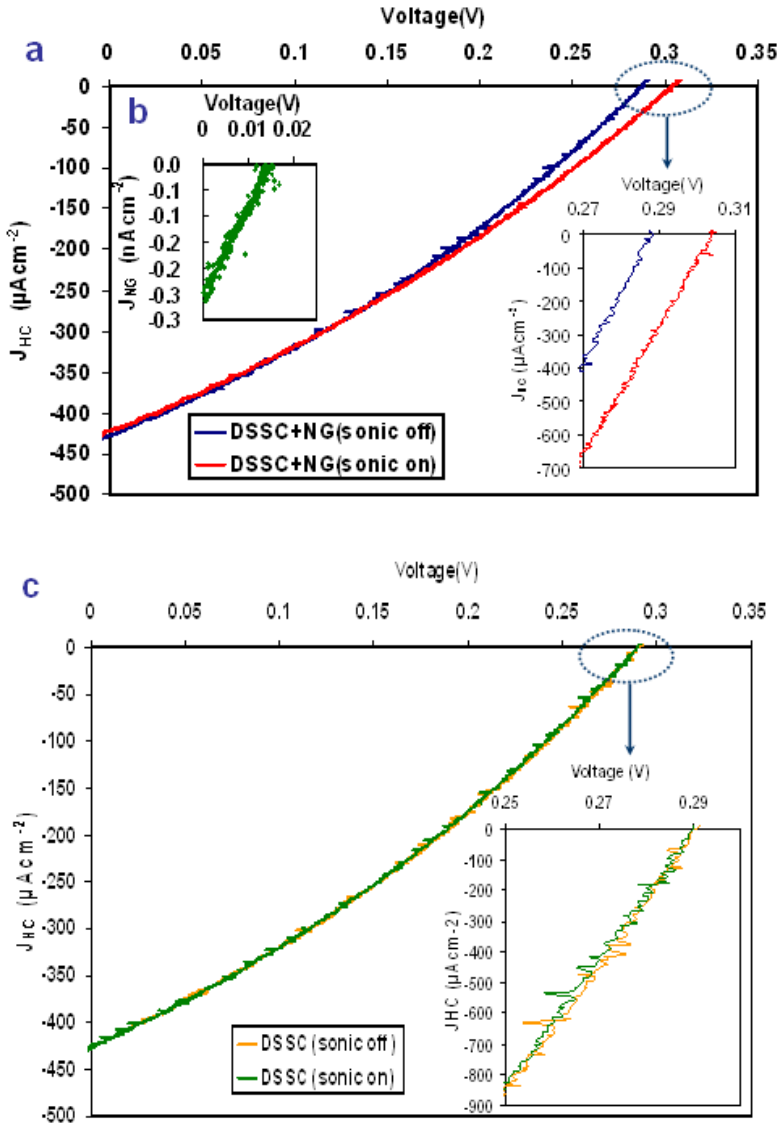

Figure 5.12 Controlled performance of the CHC. **(a)** J-V characteristics of another CHC when simulated sunlight was illuminated onto the SC side and the ultrasonic wave was turned on (the red curve) and off (the blue curve). **(b) The** J-V characteristic of the NG component subjected to ultrasonic wave excitation but with sunlight off. **(c)** The J-V characteristic of the DSSC, not including the NG unit in the measurement circuit, when the DSSC is illuminated by a simulated sunlight with (green curve) and without (orange curve) the ultrasonic waves turned on. The inset, an expanded plot around the U_{OC} points, shows almost no change in U_{OC} when the ultrasonic waves are turned on. The open circuit voltage U_{OC} point was not affected by the ultrasonic wave, which rules out any contribution by the fluctuation in NG resistance to the performance of the SC.

So that the optimum power output from the J-V curve could be visualized, the product of the current density and voltage was calculated. The area of the rectangle represented the optimum output power density. By comparing the area difference, we are able to see that the CHC enhances the energy-harvesting performance more than either one of the devices. When only the DSSC component was in operation and under the one full sunlight illumination as in Figure 5.9, the optimum output power density (the blue rectangle) was found to be 32.5 μWcm^{-2} at J_{SC} = 140 μAcm^{-2} and U_{OC} = 0.231 V. When both the DSSC and the NG were simultaneously operating in the serial connection, the corresponding output power density was 34.5 μWcm^{-2} at J_{SC} = 141 μAcm^{-2} and U_{OC} = 0.243 V (the red rectangle). An increment (ΔP_{HC}) of 2 μWcm^{-2} in the power density, which showed an enhancement of over 6% in optimum power, was achieved after the ultrasonic wave was turned on. Therefore, in addition to the open circuit voltage, the CHC successfully added up the total power outputs from both the SC and the NG.

In summary, we have developed a second generation of hybrid cell, which is fully-integrated, solid-state, compacted hybrid cell comprised of a ZnO nanowire "convoluted" structure for concurrently harvesting both solar and mechanical energy in a single device. The compacted hybrid cell is based on a conjunction design of the organic solid state DSSC and piezoelectric NG in one compacted structure; it shows an increase in not only the output voltage but also output power as the driving ultrasonic wave is turned on, clearly demonstrating its potential for simultaneously harvesting multi-type energy. An increase of 6% in optimum power for the CHC was demonstrated by incorporating the contribution made by the NG. Therefore, the CHC is more efficient for fully utilizing the available solar and mechanical energy in our living environment for powering small electronic devices for independent, sustainable, and mobile operation.

CHAPTER SIX

ENHANCEMENT OF PERFORMANCE

Chapters Four and Five illustrated the design of HCs. The results are encouraging. However, from a practical point of view, the low output of the HC is the biggest roadblock to its use in many applications. As discussed in previous chapters, the performance of the SC unit is not optimum for the purpose of HC demonstration. To ensure full utilization of the HC for renewable energy harvesting, future research must develop a means of increasing the output of the NG unit on an integrated nanowire-based energy harvesting device.

6.1 The bottleneck of the performance of the NG

The previously developed NG was based on a vertically-aligned ZnO nanowire array placed beneath a zigzag electrode with a small gap. The NG relied on the piezoelectric potential created in a nanowire that was once subject to elastic straining, which drove the flow of charge carriers. The zigzag electrode acted as an array of parallel integrated tips for the simultaneous creation, collection, and output of electricity from all of the active nanowires. However, the non-uniform heights and random distribution of the nanowires matching the zigzag electrode might prevent a large fraction of nanowires from contributing to the energy conversion process. Thus, a bottleneck technology in the application of NGs is the output power, especially the output voltage, which is dictated by individual nanowires. The output current of an NG is the sum of the current contributed by all of the active nanowires, while the ultimate output voltage is determined by an individual nanowire. Packaging technology is critical to maintaining just the right distance between the zigzag electrode and the nanowire arrays so that it is large enough to allow the nanowires to be freely bent/deflected, but small enough to ensure an intimate

contact between the nanowires and the electrode. Figures 6.1A to C show four possible configurations[74] of contact between a nanowire and the zigzag electrode. Analogous to the situation described for NW I, the same processes apply to the charge output from NW II. NW III is chosen to elaborate on the vibration/resonance induced by an ultrasonic wave. When the compressive side of NW III comes into contact with the electrode, the same discharge process as that for NW I occurs, resulting in a flow of current from the electrode into the NW. NW IV, which is short in length, is forced (without bending) into compressive strain by the electrode. In such a case, the piezoelectric voltage created at the top of the NW is negative. Thus, across the electrode–ZnO interface, a positively-biased Schottky barrier forms; hence, the electrons can flow freely across the interface. Thus, as deformation occurs, electrons flow from the grounded substrate electrode into the NW and then into the top zigzag electrode. This discharge process, if substantial, may contribute to the measured current. In each of the four cases described in Figures 4.4 A to C, all of the currents are added up in the same phase.

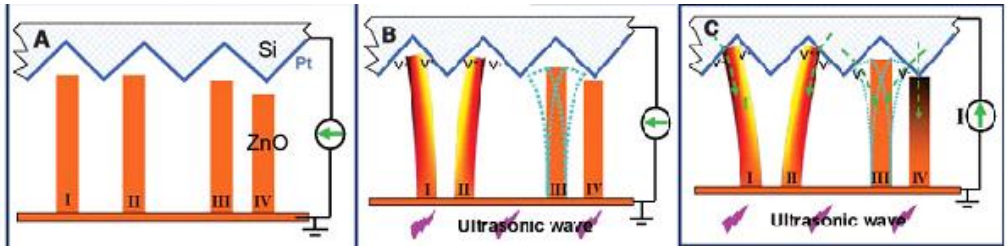

Figure 6.1 (A) Schematic illustration of the zigzag electrode and the four types of NW configurations. (B) Piezoelectric potential created across NWs I and II under the push or deflection of the electrode. (C) Schematic of the NW under vibration

Motivated by a bottleneck of the direct current NG explained above, we need to fabricate position-defined ZnO nanowire arrays on substrates that match the shape and the morphology of the top zig-zag electrode very well, which would eventually increase the number of active nanowires for all participating electricity generation. To achieve this goal, we use a new device structure by changing a vertical-NW-based to lateral-NW-

based NG. This approach requires the growth of laterally-aligned ZnO nanowires and the manipulation of contact of the two ends of the NW, which will be discussed in Section 6.2.

From the theoretical calculation[88, 89] of the ZnO nanowire, we expect to obtain enhancement in terms of the performance of the piezoelectric generator. An unstrained ZnO nanowire is grown along the c-axis with a length of 1200 nm and a hexagonal side length of 100 nm. Two ends of the nanowire are assumed to be surrounded by. As shown in Figure 6.2, it creates a potential drop of approximately 0.4 V between the two ends of the nanowire with the +c-axis side a higher potential. When the applied force changes to compressive, the piezoelectric potential reverses with the potential difference remaining at 0.4 V but with the c-axis side at a higher potential.

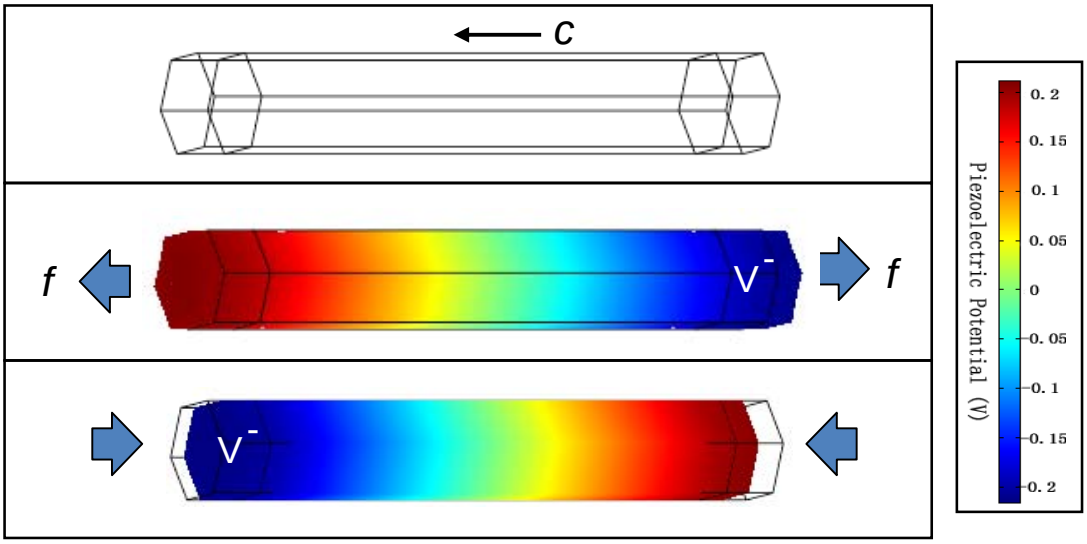

Figure 6.2 Colored online numerical calculation of the piezoelectric potential distribution in a ZnO nanowire without doping.

6.2 The lateral NG design[90]

The lateral design of a single nanowire-based AC-NG (Figure 6.3) uses a piezoelectric wire that is in firm contact with metal electrodes at each end, laterally bonded, and packaged on a flexible substrate, the bending of which can be simply driven

by mechanical agitation present in our living environment. Different from DC-NG, which is driven mostly by an ultrasonic wave source, the single wire generator demonstrates a robust approach to harvesting low-frequency energy generated by in-vitro human or animal motion. However, the output power of a single nanowire-based NG is rather limited. As in practical applications, the design of the AC-NGs must be scaled up so that we can enhance output power by integrating the contributions made by millions of nanowires.

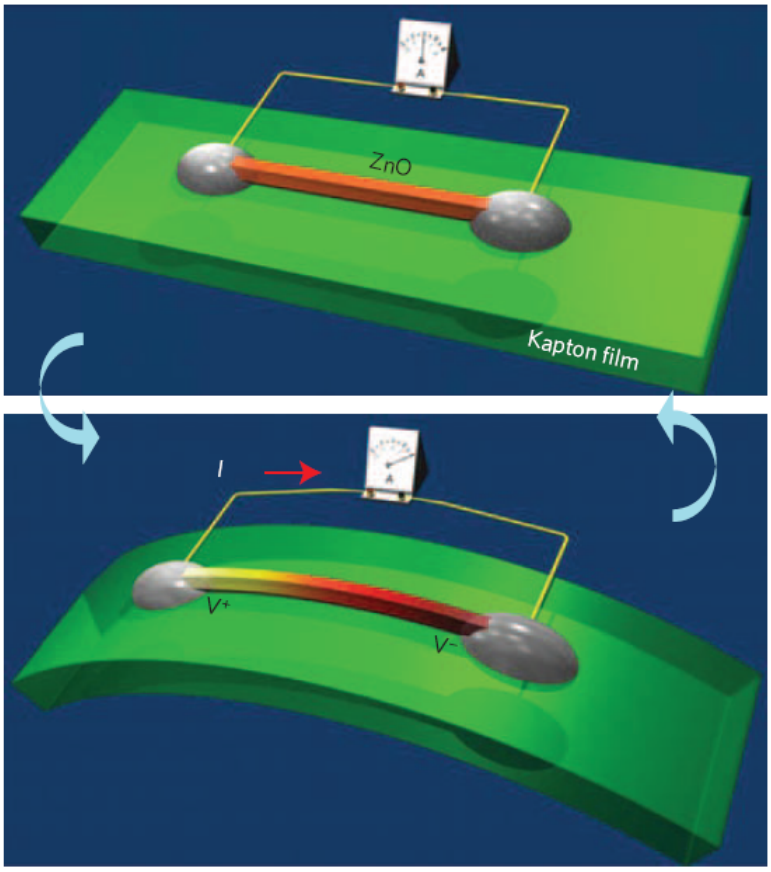

Figure 6.3 Design of a piezoelectric fine wire (PFW) generator on a flexible substrate. (a) The PFW lies on a polymer (Kapton) substrate, with both ends tightly bonded to the substrate and outlet interconnects. (b) Mechanical bending of the substrate creates tensile strain and a corresponding piezoelectric potential in the PFW, driving electrons through the external load.

To present the design of laterally-integrated NG (LING), we first illustrate the principle of the AC-NG using a single NW. The physics of the NG is based on a piezoelectric effect with the presence of a Schottky contact on at least one end of an electrode. Since the diameter of the NW is much smaller than the thickness of the substrate film, the NW is subjected to pure tensile strain when the substrate is stretched, and a piezoelectric-potential-drop is created along the NW, with the positive c-axis of the crystal orientation pointing toward the higher piezopotential side. A Schottky barrier forming on at least one end of the NW serves as a "gate" that prevents the flow of electrons across the NW-metal interface, so the electrons accumulate in the area adjacent to the contact, constituting the charging process. When the substrate is released from straining, the strain in the NW is released, and the corresponding piezopotential also disappears. The accumulated electrons will back flow through the external load, constituting the charge release process. The piezopotential in the NW serves as a "charging pump" that drives the back and forth flow of electrons in the external circuit in response to the strain and release of the NW. If we can synchronize the charge and discharge processes of many NWs, the generated AC voltage can be added up constructively (Figure 6.4), resulting in high output.

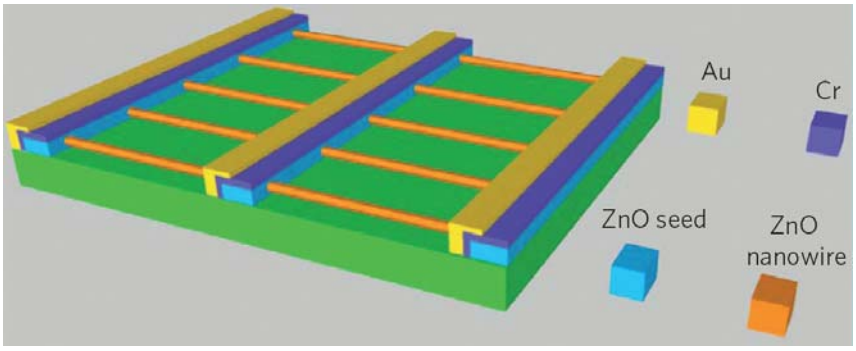

Figure 6.4 Schematics of the LING structure, where Au and Cr are used to create Schottky and Ohmic contacts, respectively, at the two ends.

Single NW based NG on a flexible substrate could be driven by mechanical agitation present in our living environment, such as human or animal motion. It is essential to enhance the output power by integrating the contributions from multiple NWs (Figure 6.4). Since the diameter of the NW is much smaller than the thickness of the substrate film, all of the NWs on the substrate are subjected to a pure tensile strain when the substrate is stretched. Every active NW works as a "charging pump" and is independent from each other as the substrate is bent and released. If we can synchronize the charging and discharging processes of many NWs, the output AC voltages can be added up constructively (Figure 6.4), resulting in a high output voltage.

To constructively integrate the outputs of many single-wire-based NGs, we must investigate several factors. First, the metal contacts at the two ends of the nanowire arrays must be non-symmetric to produce a Schottky contact on one end and an Ohmic contact on the other (Figure 6.5). This requirement follows the mechanism introduced above. Second, the contacts on the two ends of the NWs must be robust, which is achieved by fully enclosing the ends of the NWs with the deposited metal so that the mechanical deformation can be more effectively transmitted from the electrodes to the NWs. Third, all of the ZnO NWs should have the same crystallographic orientation to ensure that the alignment of the polarities of the piezoelectric potentials generated in all of the NWs. Since a ZnO NW grows in parallel to the *c*-axis in general cases, and because it has an anisotropic wurtzite structure and polarization along the c-axis, the NWs need to be rationally grown directly on the substrate rather than by chemical assembly, the latter of which usually provides orientation alignment but not crystallographic polarity alignment. Polarity-aligned NWs create a macroscopic piezoelectric potential. By contrast, randomly c-axis-oriented NWs may result in the cancellation of generated electrical current. Finally, all of the ZnO NWs must be stretched and released in a synchronized manner so that the polarities of the piezoelectric

potential generated by all of the NWs are in the same direction at the same time (Figure 6.6), resulting in maximized output voltage.

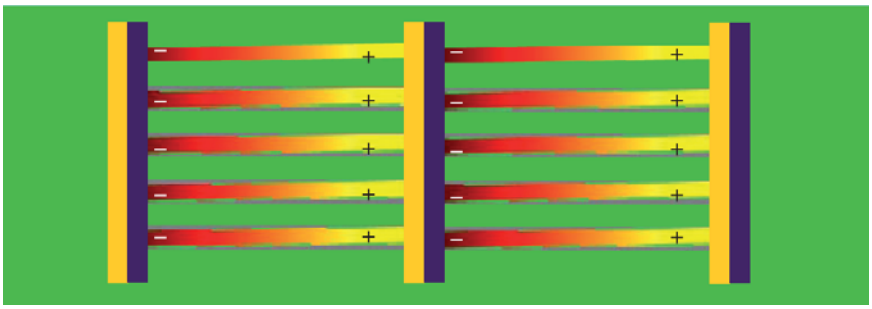

Figure 6.5 The working mechanism of the LING when it is subjected to mechanical deformation. The "+, -" signs indicate the polarity of the local piezoelectric potential created in the NWs.

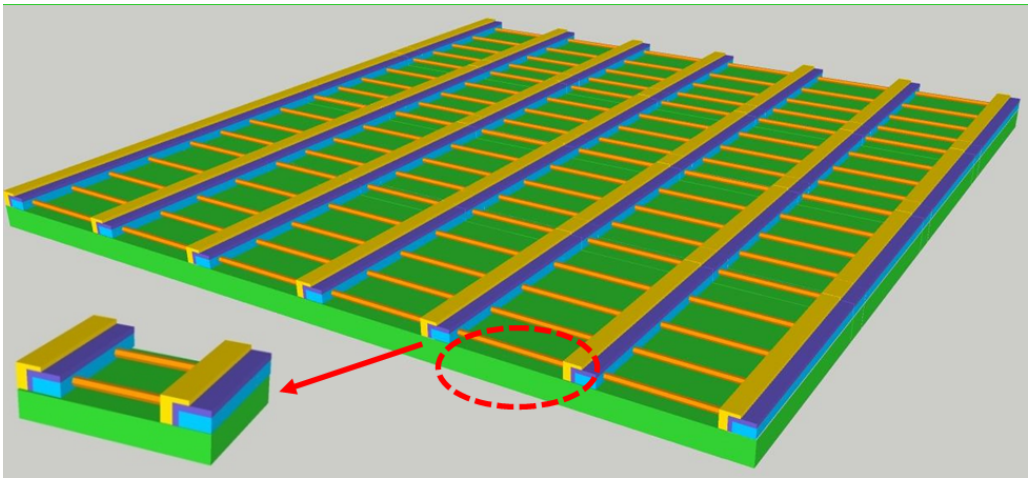

Figure 6.6 Schematics of a LING array made of many rows of nanowires.

6.3 Fabrication of a LING

The following experiments were rationally designed so that fabricated the LING meets all of the required conditions, as presented in Figure 6.7.

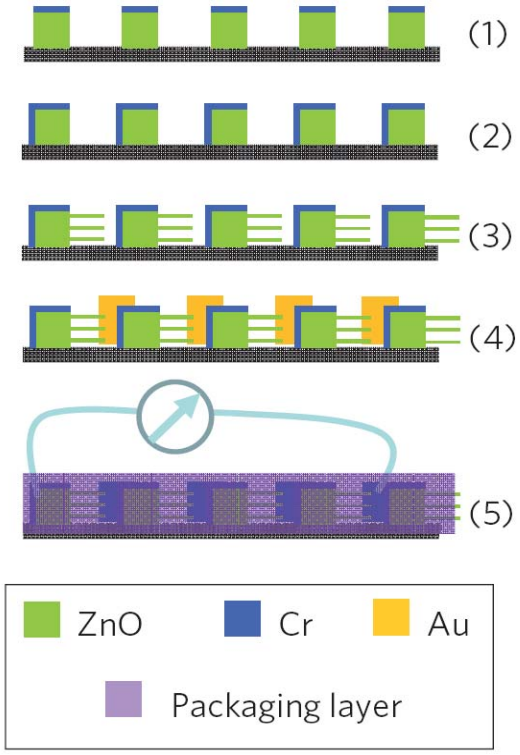

Figure 6.7 Schematics for the rational growth of orientation-aligned NW arrays parallel to the substrate surface.

The detailed fabrication of the LING followed a five-step procedure. In the first step, patterned ZnO stripes covered with a Cr layer on top were fabricated as the seed layer. A Kapton film with a thickness of 125 μm (Dupont) was cleaned with acetone, isopropyl alcohol, and ethanol using ultrasonic bath, which was used as the substrate. A photoresist (Shipley Microposit 1813) was spincoated onto this film at a speed of 3,000 RPM for 40s. Then the film was baked at 110°C for 10 minutes. The film was first patterned using a mask aligner. Then, 300 nm ZnO and 5 nm Cr layers were deposited. Finally, after the photoresist was developed and lifted off, the stripe-shape ZnO pattern with a top layer of Cr was fabricated (Figure 6.7(1)). In the second step, Cr was deposited at only one side of the ZnO stripe but with the other side exposed. We span coat the entire structure by a layer of photoresist, then used a masker to cover only one side of the ZnO strip by controlling its offset position. Optical lithography followed by developing exposed only

one side of the strips. Then, a layer of Cr (10 nm) was sputtered. A lift-off produced the structure shown in Figure 6.7(2). In the third step, after covering one side and the top side of the seed stripes with Cr, which prevented local growth, ZnO NWs were grown directly from the exposed seed layer on the other side using a chemical approach at 80ºC along the direction nearly parallel to the substrate.

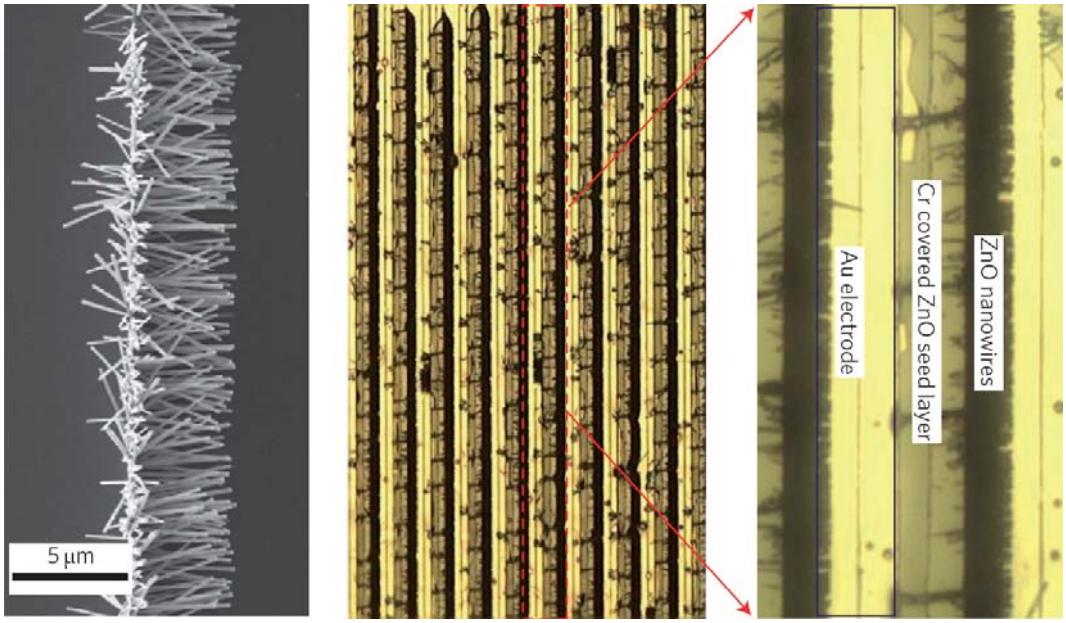

Figure 6.8 SEM image of a row of laterally grown ZnO NW arrays. Optical microscopy images of the LING structure using many rows of NW arrays.

The fabricated ZnO NW arrays, shown in Figure 6.7 (3) were crystallographically aligned. After 12 hours aging in the solution, the film surface turned white, indicating that they were covered by ZnO NW arrays. Finally, they were rinsed with deionized water several times and baked at 100ºC for 1 hour. Figure 6.8 shows a typical scanning electron microscopy (SEM) image of horizontally-grown ZnO NW arrays. Most of the ZnO NWs were grown horizontally with one end fixed to the seed layer. The length of the NWs is about 5µm, and the diameter about several hundred nanometers. Figure 6.8 is an optical microscopy image of the fabricated LING. The ZnO NW arrays are connected

end-to-end by patterned electrodes. The lengths of the NWs were controlled by refreshing the aging solution and increasing the aging time so that they reached the other electrodes (Figure 6.9).

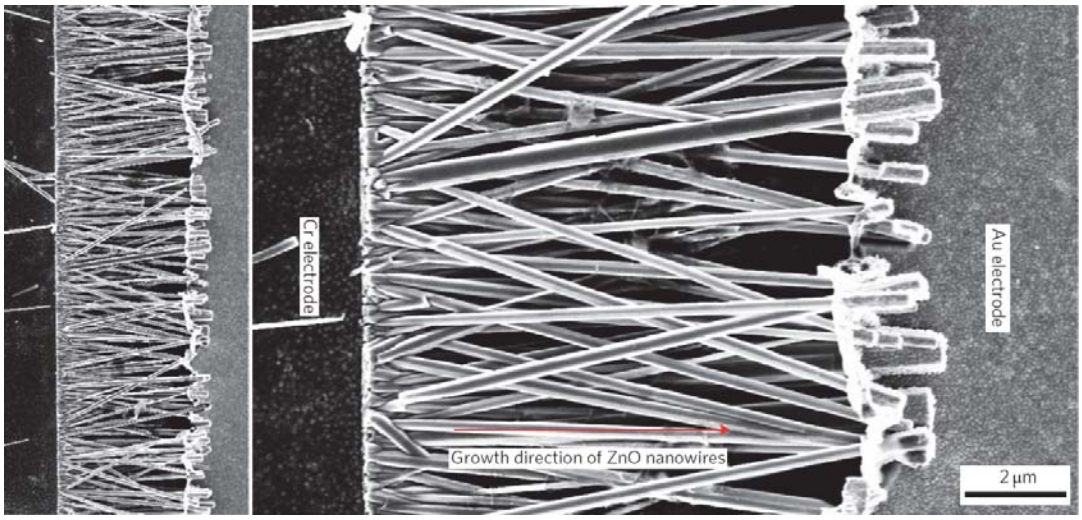

Figure 6.9 SEM images of a single-row LING structure

In the fourth step, patterned Au electrodes were fabricated using a masking technique, and the Au was deposited only on the side where the Cr layer was present (Figure 6.7 (4)). The work function of Au is higher than the electron affinity energy of ZnO, which usually leads to a Schottky connection between ZnO NWs and the Au electrode while an Ohmic contact was formed between the ZnO NWs and Cr electrode at the other end. Deposition of a thick Au film ensured a good connection between the NWs and the electrodes (Figure 6.9). Moreover, the tips of the NWs were fully enclosed and bonded with the Au electrode so that the NWs would be robust for mechanical deformation without loose contacts (Figure 6.9). Finally, the entire structure was packaged using an insulative soft polymer such as a photoresist (MicroChem PMMA 950K A2) (Figure 6.7 (5)). This packaging layer fixed the ZnO NWs firmly onto the substrate and synchronized the mechanical stretching and releasing of the NWs with the outer surface of the Kapton film. Therefore, mechanical stretching of the substrate produced tensile strain in the NWs,

which created a macroscopic piezoelectric potential along the NWs owing to the crystallographic alignment of the NWs. The multi-rows of NGs were integrated to form a flexible sheet (Figure 6.10).

Figure 6.10 A low-magnification optical image of the LING and a demonstration of its flexibility (inset).

6.4 Working principle of the LING

The working principle of the LING is very similar to that of the single NW AC-NG. For a working LING that was effective for producing output power, the I-V characteristic always showed Schottky behavior, the most outstanding characteristic of a good AC-NG.

We now examine the nature of the piezoelectric potential. The piezoelectric potential is created by ion polarization in crystal rather than free-mobile charges. Since the charges associated with the ions are rigid and affixed to the atoms, they cannot freely move. Free carriers in the semiconductor NW may screen piezoelectric charges, but they cannot completely cancel/deplete them. With the Schottky barrier at the interface, the free-electrons cannot cross the boundary between the metal and the ZnO. Therefore, a "dipole" layer between the accumulated electrons on the metal side and piezoelectric charges on the ZnO side. This phenomenon distinctly differs from that occurring on the p-n junction in semiconductor physics. Therefore, the piezoelectric potential is still preserved; however, a reduction in magnitude owing to the finite conductivity of the NW

is possible.

An as-synthesized ZnO NW is generally n-type. The presence of oxygen vacancies and impurities and a large portion of surface atoms (surface states) naturally introduce moderate conductivity for the NW. These free carriers can partially screen piezoelectric charges, but they cannot entirely neutralize them. Therefore, the piezoelectric potential is still preserved, but at a reduced magnitude, even in light of the moderate conductivity of ZnO.

When the Kapton film was mechanically deformed, the positive voltage pulse and the current pulse, generated when the ZnO NWs were tensile stretched, were measured. The stretching of the ZnO NWs generated a piezoelectric potential along ZnO NW on the Au contact side, which drove the electrons in the external circuit to flow from the low to high potential side and accumulated at the contact interface. After one second, the NG was released, which led to the disappearance of the piezoelectric potential. Correspondingly, the accumulated electrons flowed back in the opposite direction. Thus, the corresponding negative voltage pulse and current pulse were measured. Compared with the output of a single wire NG, the output voltage and current both increased, but they did not increase as high as the sum of the outputs of all the individual NGs, part of the reason of which was the smaller strain in the NWs. More importantly, it was the result of the potential drop consumed at the metal-semiconductor contacts. Thus, a thin Au electrode of only 300 nm or less may not be effective enough to establish good electrical contact with ZnO NWs

6.5 Performance of LING and discussion

To measure the energy harvesting performance of the LING, we used a periodic external force to deform the Kapton substrate so that the NWs experienced a cycling stretching-releasing deformation process (as shown in Figure 6.11). Since the Kapton substrate was much thicker than the diameter of the NWs, a mechanical motor was used to push the substrate at its middle section, stretching its outer surface and producing a pure tensile strain across the rows of the NGs built on the top. Such strain was calculated based on the curvature of the bending and the thickness of the substrate film.

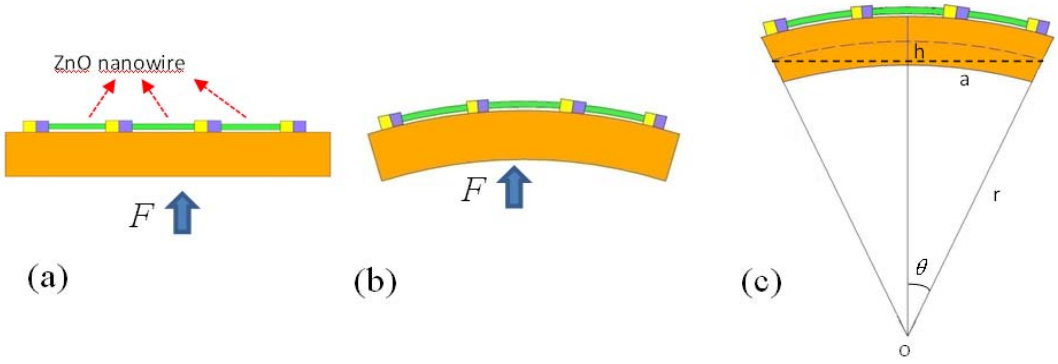

Figure 6.11 Schematics showing the LING structure and the application of a vertical force that created tensile strain in the nanowires.

By bending the substrate into an arc shape, with a dimension as illustrated, the strain created at the outer surface was

$$\varepsilon = \frac{hD}{a^2 + h^2}$$

where h is the height of the arc (e.g., the normal displacement of the substrate resulting from the external force impact) and a is the half width of the arc. The rate at which strain is created is $\varepsilon v/h$, where v is the speed at which the external force impacts the substrate. In our experiments, we pushed the Kapton substrate at a relatively fast strain rate, but held it at one position for one second before releasing it. Then we waited for two seconds

before pushing it again. The degree to which the LING can be deformed is determined by the robustness of its structure.

Enhancing the output voltage and the current of the LING necessitate the integration of more ZnO NWs, an improvement in the interconnection between electrodes and ZnO NWs, and an increase in the strain as well as the strain rate. Figure 3 shows the output voltage and the current of a LING that has demonstrated an average output voltage of ~1.2 V at a strain rate of 2.13%/s and a strain of 0.19%. The LING was composed of 700 rows of NWs, each of which contained about ~20,000 NWs. When the Kapton film was mechanically deformed, a positive voltage pulse of 1.2V and a current pulse of 26nA were measured (Figures 6.12a and 6.12b). Note that the magnitudes of the current/voltage peaks slightly differed when the LING was stretched and released because the strain rate in the two processes differed; the stretching was driven by an external force while the releasing was natural. The inserted figures are the V_{oc} and I_{sc} output for one cycle of deformation. The stretching of the ZnO NWs generated a piezoelectric potential along ZnO NW on the Au contact side, which drove the electrons in the external circuit to flow from the low to high potential side and accumulated at the contact interface. After one second, the NG was released, which led to the disappearance of the piezoelectric potential. Correspondingly, the accumulated electrons flowed back in the opposite direction. The average output voltage peaks were greater than 1.2V (indicated by the red dashed line in Figure 6.12a) and the maximum voltage reached 1.26V. These results demonstrate the potential of scaling up the output voltage by the serial integration of many rows of NWs. Most of the output current peaks were greater than 25 nA (indicated by the red dashed line in Figure 6.12b) and the maximum current peak was 28.8 nA. By assuming that one-third of the NWs were actively contributing to the current output, the average current generated by one NW was estimated to be 4.3 pA, which was compatible to the output current of ~10 pA when an NW was triggered by an AFM tip. Excluding the area occupied by the electrodes, we obtained a peak output power density of ~70 nW/cm^2.

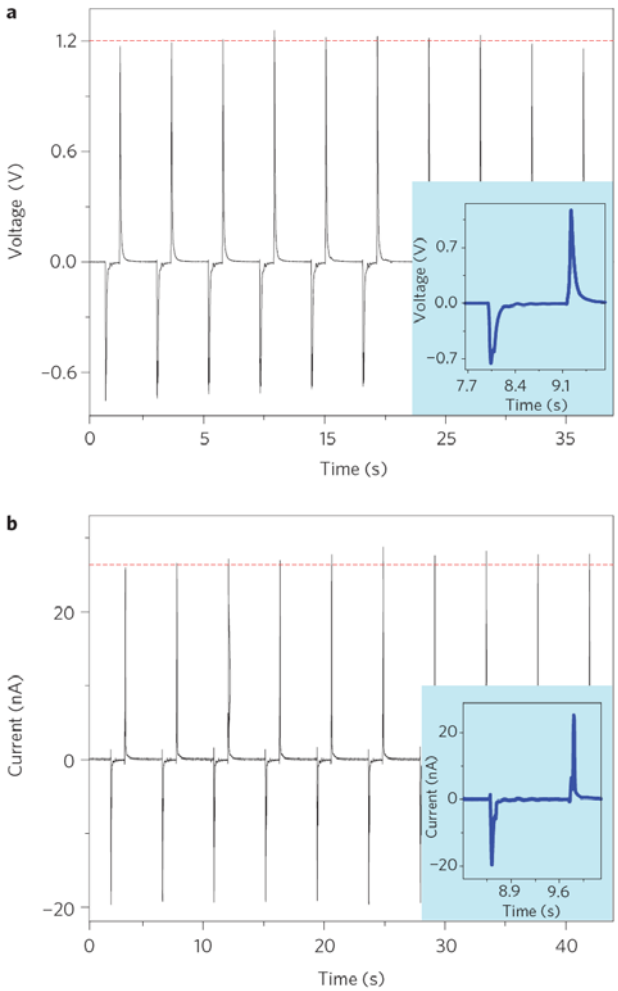

Figure 6.12 The performance of a laterally-integrated NG. (a) Open-circuit output voltage and corresponding (b) short-circuit output current measured from a LING structure consisting of 700 rows of NW arrays. The maximum output voltage peak reaches 1.26V. The insets are output voltage and current in one cycle of mechanical deformation. The LING is periodically deformed at a strain rate of 2.13%/s to a maximum strain of 0.19%.

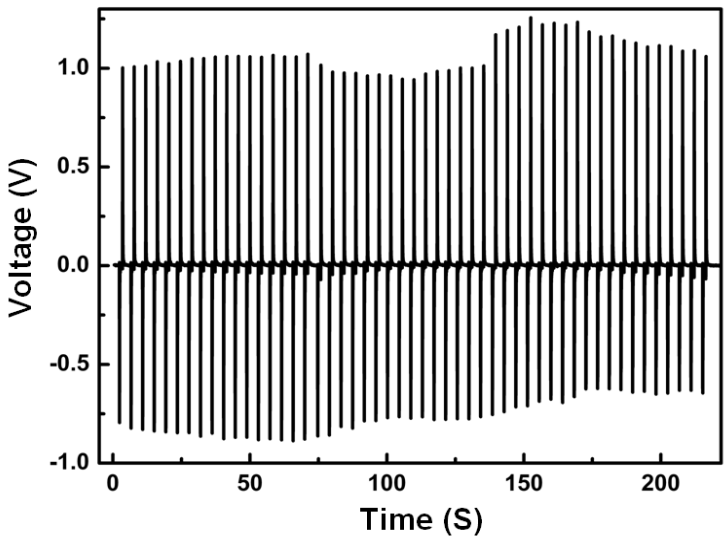

Figure 6.13 Open-circuit output voltage of a lateral integrated NG with 700 lines of ZnO NW arrays of over 50 cycles.

The cycle test is one of the most stressful tests conducted on the LING. The chart above shows the performance of the LING tested over 50 cycles. An increase in the strain is an effective way to obtain high output voltage and current because the magnitude of the piezopotential increases relatively linearly with strain. Figure 6.14a shows the output short-circuit current I_{sc} and open-circuit voltage V_{oc} measured at a different strain from that of a LING structure consisting of 100 rows of NWs. Both I_{sc} and V_{oc} increased monotonously with the increase in the strain. I_{sc} was 137 pA when the strain was 0.03%, and it increased to 288 pA when the strain was 0.055%. V_{oc} was 25 mV when the strain was 0.03%, and it increased to 57 mV when the strain was 0.055%. A large V_{oc} of 121 mV was measured as the strain increased to 0.085%. Increasing the strain rate is also effective at raising the output voltage. Shown in Figure 6.14b is a measurement from an NW as a function of the strain rate by maintaining a fixed maximum strain. Both the output current and the voltage increased as the strain rate increased.

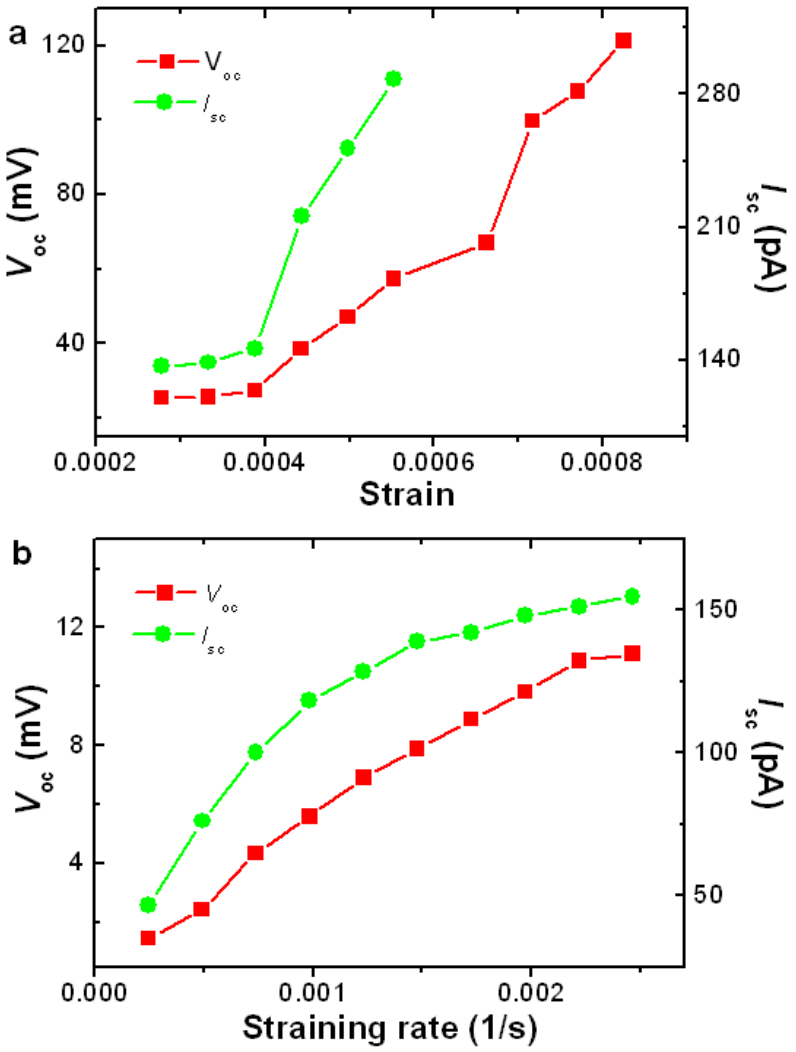

Figure 6.14 (a) The open-circuit output voltage and the short-circuit output current of a LING as a function of the tensile strain created in the NWs. (b) The open-circuit output voltage and the short-circuit output current of a LING consisting of 100 rows of NWs, as a function of the strain rate at which the LING is deformed by the mechanical stimulator. The maximum strain remains 0.025%.

The LING structure has been demonstrated to largely enhance the total output voltage of NGs by lateral integration—a major milestone in the development of applications of NGs. The limited output current is likely the result of several factors. First, the orientation alignment of the as-grown lateral-NWs was not perfect, and many were sticking out slightly away from the electrode (see Figure 6.9), so only a fraction of them were in contact with the Au electrode. Among the NWs that were in contact, only a

fraction of them, the so-called active NWs, were actively outputting electricity, while the inactive NWs made no contribution to the output current but served as capacitance, reducing the output voltage. Another factor was the bonding between Au and ZnO, which was not very tight, for it may have loosened during repeated mechanical stretching that may have prevented a large strain from being applied to the NWs. In the experiments in this work, we applied a maximum strain of only 0.19%. Theoretical simulation indicates that the maximum tensile strain that a ZnO NW can hold before fracture is 6%. A final factor was the inner resistance of the entire integrated sheet, 1-10 MΩ, which reduced the total output current.

In summary, based on a rational chemical synthesis of nanowire arrays parallel to a polymer substrate, a row-by-row laterally-integrated nanogenerator (LING) that raises the output voltage of the NGs was fabricated. A LING structure consisting of 700 rows of nanowire arrays increased the magnitude of the output voltage to 1.26V in response to low-frequency mechanical strain at a strain rate of in between 2.13%/s and 0.19%. The structure, built on a general flexible, foldable, and stretchable substrate, was processed and fabricated at a substrate temperature of $<100^{o}$C; thus, such a structure can be applied virtually to any materials at a low cost. The materials used were environmentally friendly and biocompatible. ZnO NWs are easy to grow on any substrate of any shape at a low temperature. In addition, experimental observation shows that ZnO NWs are robust and fatigue free. Therefore, a layer-by-layer integration of LINGs is possible for fabricating three-dimensional energy harvesters that have a high enough output for powering small electronic devices for independent, sustainable and self-powered operation. Our current work demonstrates a technological roadmap for improving the performance of the NGs in practical applications.

6.6 Enhancement of HC performance

Although a flexible HC design that improves voltage output has been developed, enhancement of the current is also required. To achieve this goal, we connected a ZnO nanowire-based DSSC to an NG with improved performance in parallel to form an HC (Figure 6.15). In this work, instead of generating direct current (DC), the NG generates alternating current (AC) output synchronized with an external strain. The output current density of the HC contributed by the NG unit was about 0.3 $\mu A/cm^2$ and that of the SC unit was 0.95 $\mu A/cm^2$.

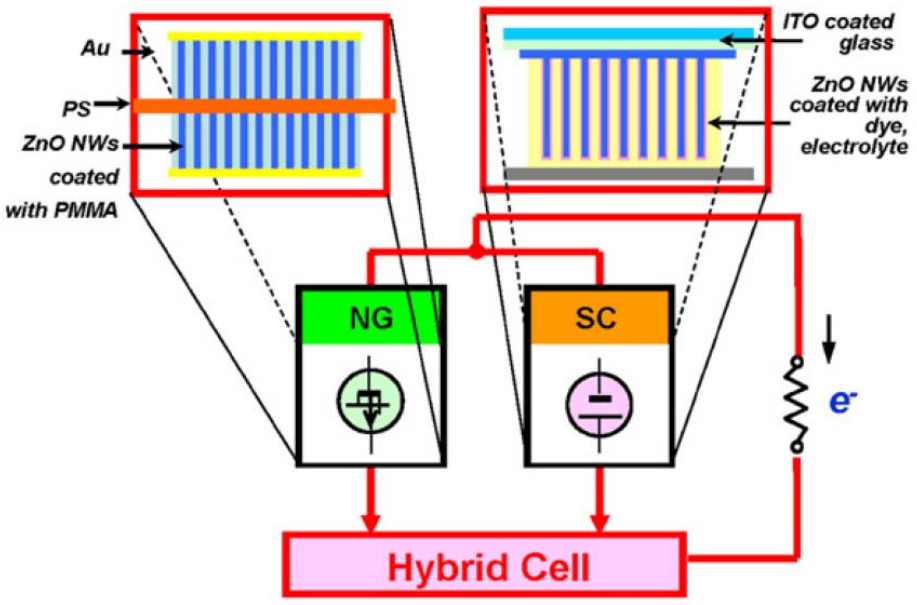

Figure 6.15 Design and performance of the parallel connected HC consisting of an SC and an NG. (a) the SC is illuminated by sunlight from the top and the NG is driven by a linear motor. The ITO layer of the SC and one side of the Au electrode of the NG are connected as a cathode while the Pt electrode of the SC and the other side of the Au electrode of the NG are connected as an anode.

In this design, a double-side grown ZnO nanowire-based NG[91] was chosen for the mechanical energy converter, and it was based on NG theory, generated voltage from the piezoelectric potential with the applied strain along the c-axis of the ZnO nanowire grown direction. Instead of using vertically-aligned ZnO nanowires, ZnO nanowire

textured films were grown on the top and bottom surfaces of a flexible polyester (PS) substrate (Dura-Lar, 220 μm thick), and the top surfaces of these nanowires were scratched so they would bond tightly to the nanowires in a uniform film. Therefore, the entire ZnO nanostructure could be regarded as a textured thin film consisting of fully-packed ZnO nanowire arrays between two parallel ZnO nanowire films. According to the growth mechanism, the c-axes for these nanowires were their growth direction. Finally, after the two leads were connected to the top and bottom electrodes, the entire device was fully packaged with polydimethylsiloxane (PDMS) to enhance its mechanical robustness and flexibility. Thus, each bending of the NG generated an electric pulse.

Considering the AC contribution of the HC, the multi-type energy harvesting function was characterized by recording the current-time curve in Figure 6.16. The operation of the HC devices is very similar to that of the flexible HC, which was tested with simulated light under simulating mechanical strain generated by a linear motor that was accurately controlled by software. First, the simulated light (AM 1.5) was shined onto the HC, detecting the output of current density contributed from the solar unit of $0.95\mu A/cm^2$. After turning off the simulated light, periodic strain was applied to the HC at a frequency of 0.67 Hz instead of driving it by ultrasonic wave. Figure 6.16 shows that the strain frequency was in consistent with the output current line. The compressed and tensile strains corresponded to up and down peaks. During each cycle, the applied strain was maintained for 0.5s; then it was withdrawn and the NG was unstrained for 1s before the next cycle. A maximum output of current density of $0.3\mu A/cm^2$ was obtained, as shown in the second column of Figure 6.16. Then the simulated light was turned on again, and a mesa enhancement of the current output was obtained. The AC current output varied from $0.65\mu A/cm^2$ to $1.25\mu A/cm^2$, confirming that both the solar and NG units contributed to the output. The fourth column shows that the mechanical contribution remained, even when the solar light was turned off.

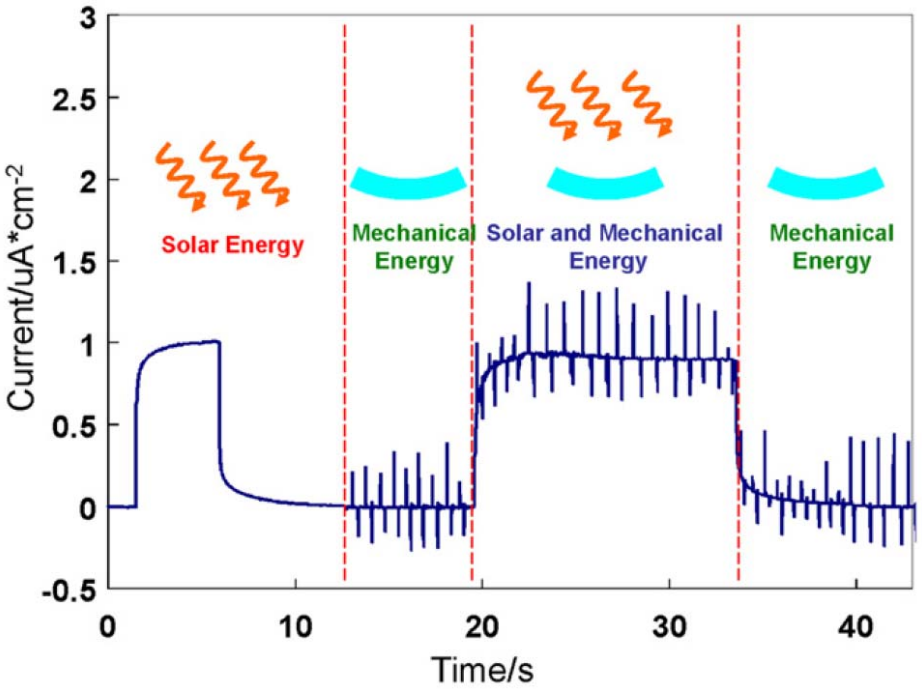

Figure 6.16 A comparison in power output J–t characteristics of a parallel connected HC that works independently and simultaneously.

Since the current output levels of the NG and the SC are comparable, small electronic devices can be driven by HCs with different types of energy. With the HC device, the various sources of energy become more compatible and thus provide a reliable power source for small electronic devices.

CHAPTER SEVEN

APPLICATIONS AND POWER MANAGEMENT

In the previous chapters, the design and fabrication of hybrid cells with a focus on solar and mechanical energy have been illustrated. While the applications based on solar cells are widely in use, those based on mechanical energy[92, 93], despite the rapid enhancement of the performance of NGs[94], are not currently in widespread use are not. This chapter describes how to power LCD by a NG driven by mechanical energy. Meanwhile, advances in nanoscale integration have resulted in a new class of miniaturized electronic systems (e.g., smart dust sensors, biomedical implants[95]) that enable new application domains. This discussion should lead to a better understanding of various design considerations and tradeoffs for a multi-energy harvesting system.

7.1 Liquid crystal display demonstrations by mechanical energy

7.1.1 Lighting an LCD with an NG

We continue to improve the performance of the NG[90, 91, 96-98] so that mechanical energy will be a complementary/secondary source of power for wireless devices. For example, the output power of the NG can sufficiently drive an LCD screen. As shown in the equivalent circuit (Figure 7.1), the NG and the LCD are connected in a traditional fashion.

An LCD is a nonpolar device that can be driven directly by AC power as long as its output potential exceeds a threshold value. The LCD screen used for the test was taken from a Sharp calculator; a proper connection combination was chosen to obtain an output of number “6” at the front panel; the size of the lighting area was about the same as that of the NG. The LCD screen

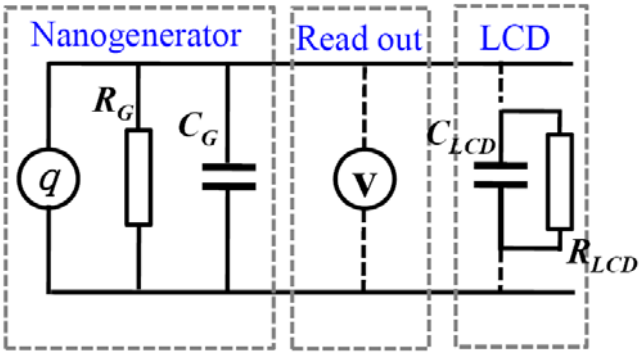

Figure 7.1 Equivalent circuits of the NG, a read out voltmeter, and the LCD load.

was directly connected to an NG without involving any external sources or measurement meters. Figure 4a depicts a series of snapshots taken for a full cycle driving of an LCD by the NG at a frequency of 0.3 Hz, showing a correspondence between the blinking LCD and each AC output peak of the NG. The output was measured at 2V (equivalent to an open circuit voltage of 3.3 and 50 nA in current (Figures 7.2b,c). Thus, the LCD screen blinked when a periodical mechanical deformation of strain 0.11% at a strain rate of 3.67% s^{-1} was applied to the NG. The output of the NG was not affected significantly by the increase in the driving frequency (Figure 7.2d), and the power output at each peak was able to drive the LCD (see video 1).

The construction of the LCD screen can be regarded as some liquid crystal insert between two electrode plates. This load is equivalent to a capacitor, a C_{LCD}, with a parallel connected leakage resistance, R_{LCD}, as shown in the equivalent circuit in Figure 7.1. With regard to the resistance of our voltage and current measurement equipment, we derived the equivalent inner resistance R_G of this NG, which was 66.7MΩ, using the measured voltage and current values, and obtained a maximum output power of 42 nW.

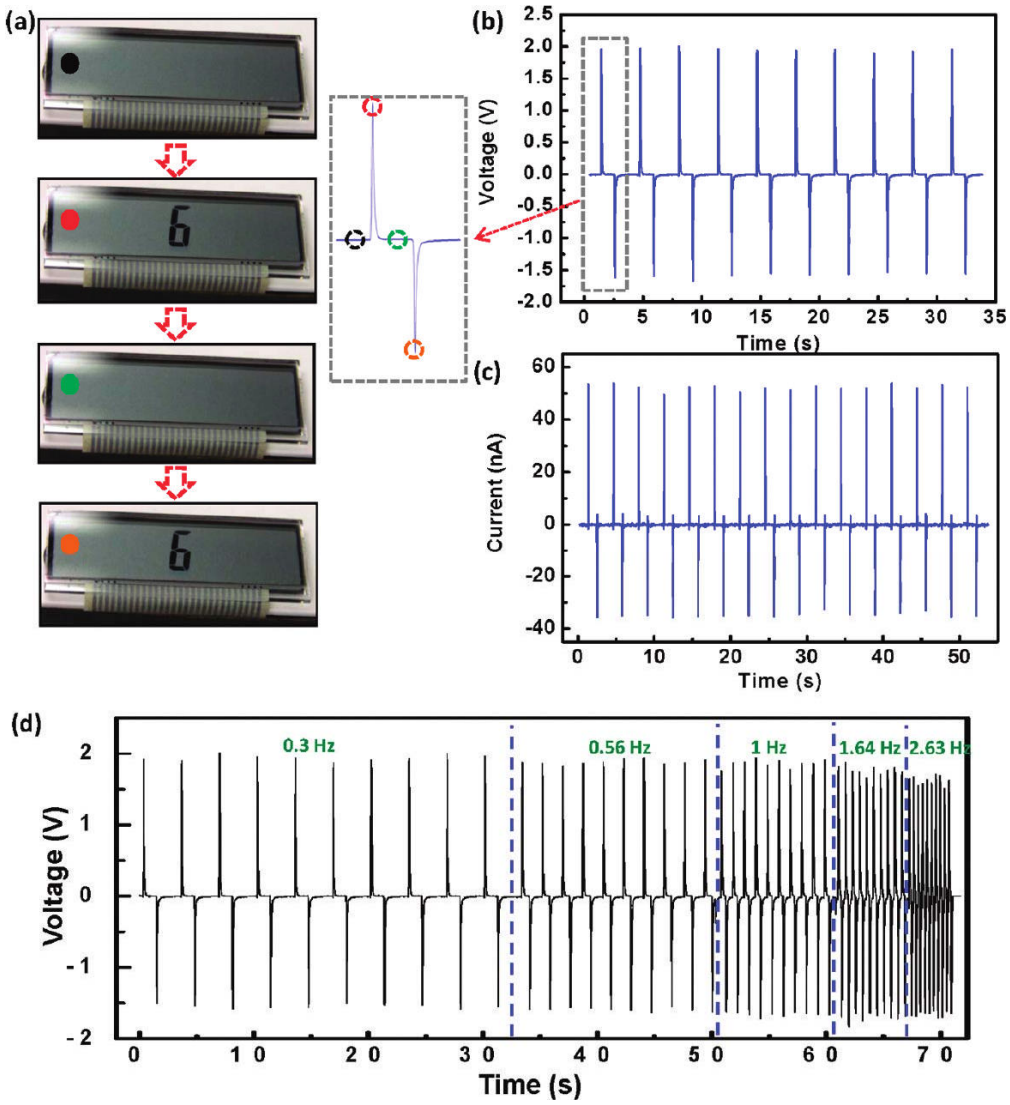

Figure 7.2 Driving a commercial LCD by an NG. (a) Four snapshots taken from a full cycle driving of an LCD by the NG at a frequency of 0.3 Hz (b) and (c) the measured output voltage and output current of the NG. The right-hand part of (a) is an enlarged single cycle of the NG output. We use the dotted circle marked in different colors to show the LCD blinking that corresponds to each AC output peak of the NG. The LCD was taken from a calculator; only a small segment of the entire display area was powered by the NG. (d) The output of the NG with the increase in driving frequency, showing its good stability.

The NG can continuously light an LCD. An LCD screen is a capacitive device that can release input charges within specific a period of time, during which it continuously lights up if the electric field generated by the remaining stored charges exceeds the threshold, which is possible if the LCD discharging time is longer than the time interval between two consecutive mechanical

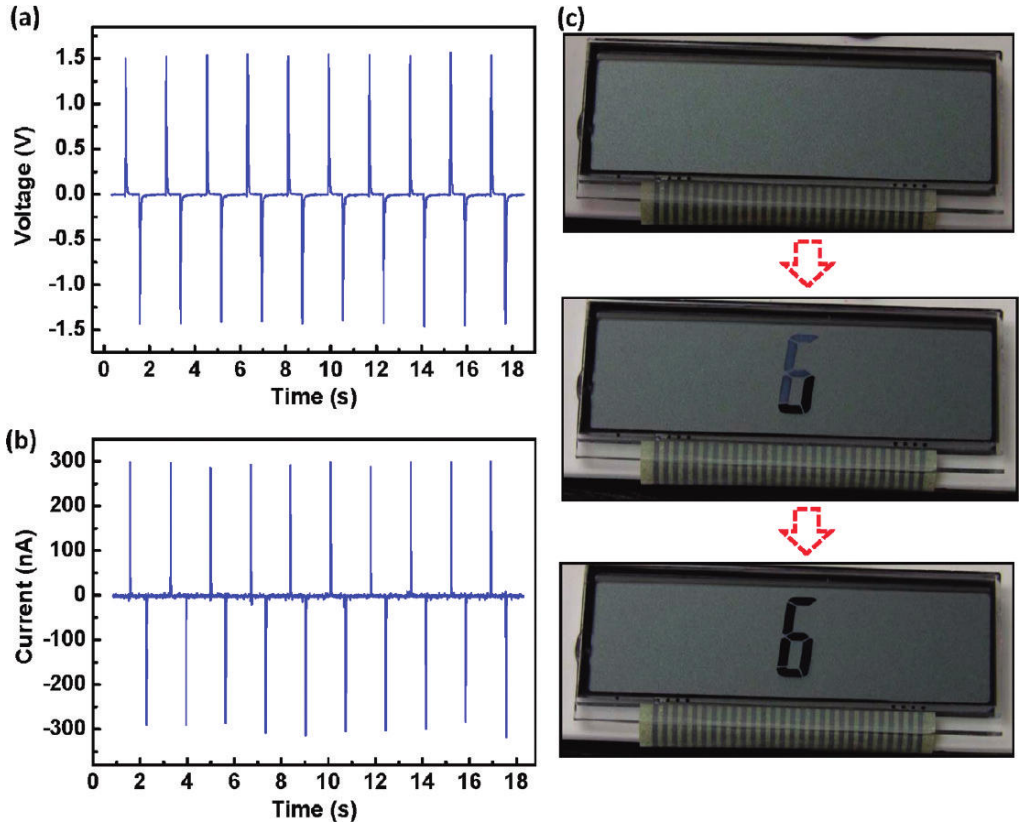

Figure 7.3 Continuous driving of a commercial LCD by an NG at a mechanical straining frequency of 0.56 Hz. (a, b) The measured output voltage and the current of the NG with a peak voltage of 1.5 and a current of 300 nA. (c) Three snapshots taken from the LCD when the NG was periodically strained at a frequency of 0.56 Hz, showing part of the character "6" lit up and then all of the segments continuously lit afterward.

straining actions, and its charging time is shorter than the response time of the human eye. Parts a and b of Figure 7.3 show the performance of an NG with an output of 1.5 V and current of 300 nA. The equivalent inner resistance of this NG was 5.3MΩ, and the maximum output power was 118 nW. When the LCD screen was powered by the NG, it showed a continuous lighting up status (Figure 7.3c) (see video 2). The video shows that the screen was blinking at first, and then part of the segments were lit continuously. Finally, after several cycles, it reached an equilibrium lighting status for the full character, indicating that our NG is capable of generating enough power to continuously drive an LCD.

Video 1: Real-time imaging showing the lighting up of an LCD powered by an NG at each cycle of the mechanical movement.

Video 2: Real-time imaging showing the continuous lighting of a triggering. The triggering frequency was increased slowly, demonstrating the operation of the NG at variable frequencies. An LCD was powered by the NG after a few seconds of operation. The mechanical agitation frequency was 0.56 Hz.

7.1.2 LCD demonstration by a rotating tire[96]

For bicycles, cars, trucks, and even airplanes, a self-powered monitoring system for measuring the inner tire pressure is not only important for the safe operation of the transportation tool, but also for saving energy. After the lighting of an LCD by an NG driven by a linear motor, the NG was integrated onto the inner surface of a bicycle tire, demonstrating the possibility for energy harvesting from the motion of automobiles. A small liquid-crystal display (LCD) screen was lit directly using an NG that scavenges mechanical energy from the deformation of a tire in motion. The effective work area of the NG was about 1.5 cm × 0.5 cm, and the maximum output power density approached 70 μW cm^{-3}. The integration of many NGs is presented for scale-up. Furthermore, the NG showed the potential to work as a self-powered tire-pressure sensor and speed detector. This work provides a simple demonstration of the broad application prospects of NGs in the field of energy harvesting and self-powered systems.

In general, tires turn and compress during their rotations. The shape change rate of the tires at positions where they touch or detouch the road surface is very large and can be regarded as a good mechanical trigger that quickly introduces or withdraws a bending, as shown in Figure 7.4 a. If a flexible NG is attached to the inner surface of the tire, an electric pulse is generated at the moment it passes through such a position. Depending on the strain induced by such a trigger and the performance of the NG, the energy harvested in this process may be enough to directly power a small electronic device or system. The energy harvested after a number of cycles can be stored in a capacitor or battery for powering larger consumption electronics. In this study, we used a bicycle tire to simulate the working conditions of a tire because it can easily be handled in a laboratory; however, this approach can be applied to any tires.

Figure 7.4b shows the experimental setup in which a tire (diameter ≈ 14 in.) was removed from a bicycle and caught between two rigid boards. One of the boards was fixed, and the other, connected to a linear motor, could be moved back and forth. The tire was squeezed and released periodically to simulate conditions that occur at the position where the touching or detouching of the road surface takes place. The NG used in this experiment, designed with a free-cantilever beam structure, consisted of five layers: a flexible polyester (PS) substrate, ZnO nanowire (NW) textured films on its top and bottom surfaces, and electrodes on the surfaces. The detailed fabrication and working mechanism of this type of NG can be found elsewhere. Each time the NG was bent, an electric pulse was generated. Figure 7.4c shows an NG attached tightly on the inner surface of the tire using adhesive tape. Due to its flexibility, the NG adhered tightly to the inner surface of the tire.

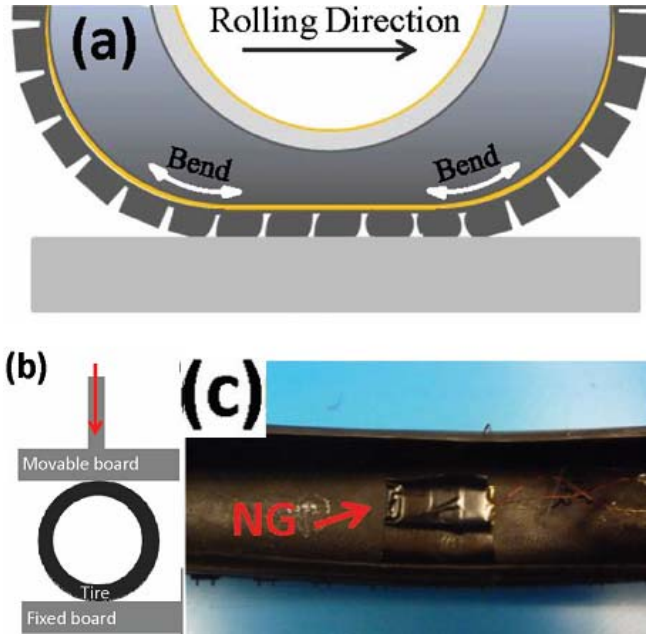

Figure 7.4 (a) Change in the shape of the tire during the movement of a vehicle. (b) Experiment setup in which a tire was caught between two boards, the purpose of which was to simulate the deformation of a tire at the position where touching or detouching the road surface takes place. (c) A photograph showing that an NG was fixed on the inner surface of a tire using adhesive tape.

Electric measurements characterized the performance of the NG under these conditions. The tire was squeezed and released by the movement of a board connected to a linear motor. Each time, an electric pulse corresponding to the trigger was generated. The result is shown in Figure 7.5. The measured output approached 1.5V, and the measured output current was around 25 nA when the travel distance of the board was 12 mm with an acceleration of 30 ms^{-2}. Compared to the results reported previously, the performance was somewhat degenerated under these conditions

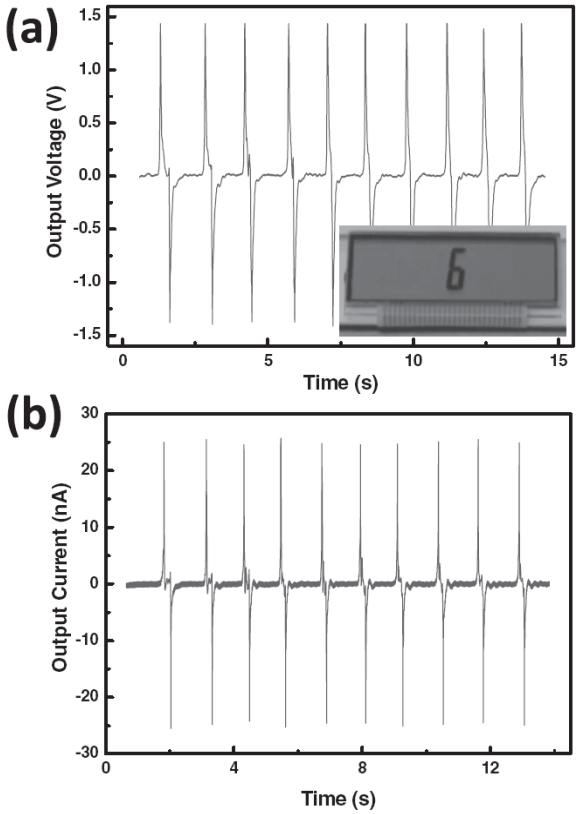

Figure 7.5 Performance of an NG attached to the inner surface of a tire, which was triggered by the deformation of the tire. The insert of (a) shows an LCD screen that was lit by the NG.

because rubber is a material that absorbs some of the mechanical energy, and the strain rate of this material is smaller than that of a rigid material under the same trigger conditions. However, the performance is still very good. A commercial LCD screen,

taken from a Sharp calculator, was connected to the NG. The screen was lit directly by the NG each time it was triggered.

The relationship between the measured output voltage U and the open circuit voltage Uoc of the NG is $U = U_{oc} R_m /(R_G + R_m)$, in which R_G is the inner resistance of the NG and R_m = 100 MΩ is the resistance of the voltmeter. This relationship indicates that the true open circuit voltage can be significantly larger than the measured output voltage if R_G is comparable to R_m . The measured output current I is related to the short circuit current I sc by $I = I_{sc} R_G /(R_G + R_m')$, where R_m' is the resistance of the ampere meter, which is 10 kΩ with a sensitivity of 10^{-8} A V^{-1} . According to the recorded data, the equivalent open circuit voltage is 3.4V, the inner resistance of this NG is about 136 MΩ, and the maximum output power density is around 70μW cm^{-3} at the volume occupied by ZnO. For real applications, NGs could be integrated into the entire inner surface of the tire and stacked layer-by-layer. For a common automobile tire, the inner surface area is about 1.5 m × 0.2 m. The size of the effective working area of our NG was around 1.5 cm × 0.5 cm. Thus, if a 1 cm thick working medium was attached, a 50 W output power could be generated for one vehicle. Considering that the total vehicle population is over one billion worldwide, energy harvesting technology based on this design has amazing application potential.

7.2 Micro-scale power system for hybrid cells

7.2.1 A system design perspective[99]

While the basic idea of environmental energy harvesting has been extensively explored and applied to the LCD, the design of micro-scale energy harvesting systems involves several new challenges. Most of these challenges stem from the fact that the form-factor constraint in these systems mandates the use of miniature energy

transducers[100] (a few cm^3). As a result, the maximum power output of these micro-scale transducers is extremely small, often only a few mW. Thus, the harvesting subsystem should be carefully designed to extract as much power as possible from the transducer and to transfer it to the electronic system with minimal loss, which requires extremely energy efficient design[101, 102]. This paper presents an overview of various system-level tradeoffs and considerations involved in the design of highly efficient micro-scale energy harvesting systems.

Figure 7.6 shows the block diagram of a micro-scale energy harvesting system consisting of four main components. The first component is the energy transducer, which captures energy from an ambient source and converts it into electrical energy. We discuss the operation and the modeling of various energy transducers in Section 7.2.2. The second component is the power conversion circuit, which serves as the load for the energy transducer. The power conversion circuit accepts the input electrical power produced by the transducer and conditions it for use by the system being powered. This step involves voltage rectification, if needed, followed by voltage level conversion. The power conversion circuit also ensures that the transducer operates at high efficiency (using a technique called "maximum power point tracking"). The design of efficient power converters and maximum power point tracking schemes for micro-scale energy systems is an active area of research. The third component is the energy storage subsystem, which stores the harvested energy for later use by the electronic system, the final component that operates using harvested power. The power consumption of the target system can be dynamically adjusted (using various power management techniques) so that it matches the amount of power available from an environmental energy source, resulting in an adaptive, self-sustaining system.

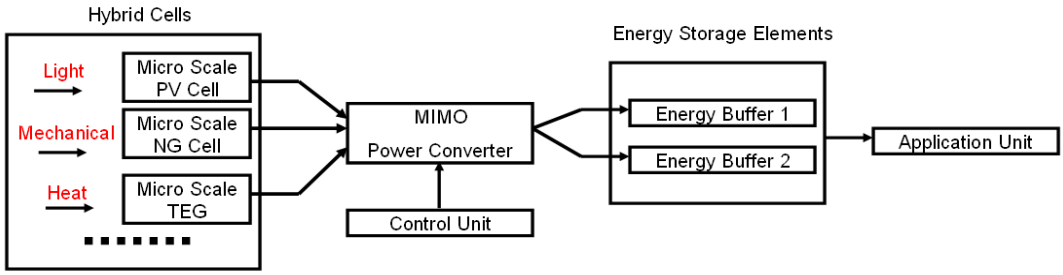

Figure 7.6 Multiple-input multiple-output (MIMO) energy harvesting

Figure 7.7 is a diagram of the proposed multi-type energy harvesting system for a hybrid cell. It is composed of five main blocks: the energy harvester, the power converter, the tracker, the control block, and the application unit. The energy harvester, which collects energy from the environment and produces unregulated low voltage, can be a non-stacked photovoltaic cell, a thermo generator, a nanogenerator, or a combination of

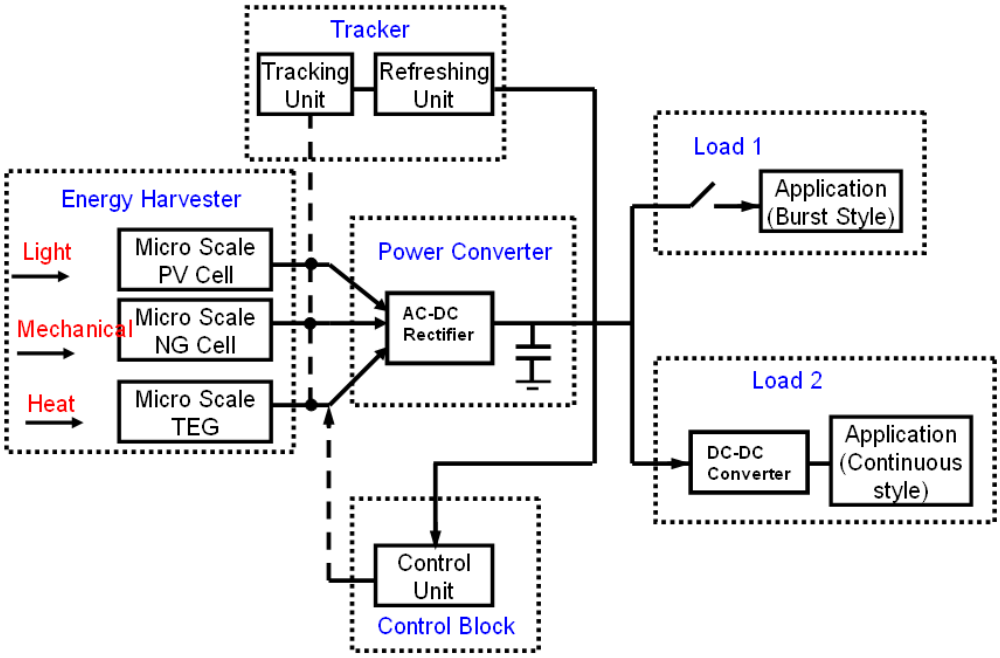

Figure 7.7 MIMO energy harvesting system

them. The unregulated low voltage of the energy harvester block is supplied to the power converter unit, where a high conversion ratio charge pump steps up the voltage and transfers the harvested charge into an energy buffer. The control unit provides the desired switching frequency with enough capability to drive the charge pump. An MPP tracking unit is connected to both the energy harvester and the control unit. The output of the tracking unit is sent to the control unit to turn on/off the switch that supplies current to the load and refreshes the setting. If the harvested power is larger than the power loss of these three blocks, the system can be self-powered without the need of a battery.

7.2.2 Electrical model of the energy transducer

Nanogenerator

An equivalent electrical model, shown in Figure 7.8, consists of a sinusoidal current source $i(t)=Ip \sin(2\pi ft)$, in which Ip depends on the vibration magnitude, f is the vibration frequency, and C_{NG} and R_{NG} are the internal capacitance and resistance, respectively. Measurement results show that C_{NG} is almost constant under a wide range of vibration frequencies. R_{NG} is usually very large and can be ignored. The output voltage of a piezoelectric film depends on the structure, the piezoelectric properties, the mechanical vibration strength, and the output impedance of the material.

From a simulation of Pspice, the bottom part of Figure 7.8 shows the output voltages using the equivalent electrical model for different output loadings. Since the output of the NG is an AC voltage signal, for energy harvesting, we need an AC-DC rectifier to convert it to DC voltage.

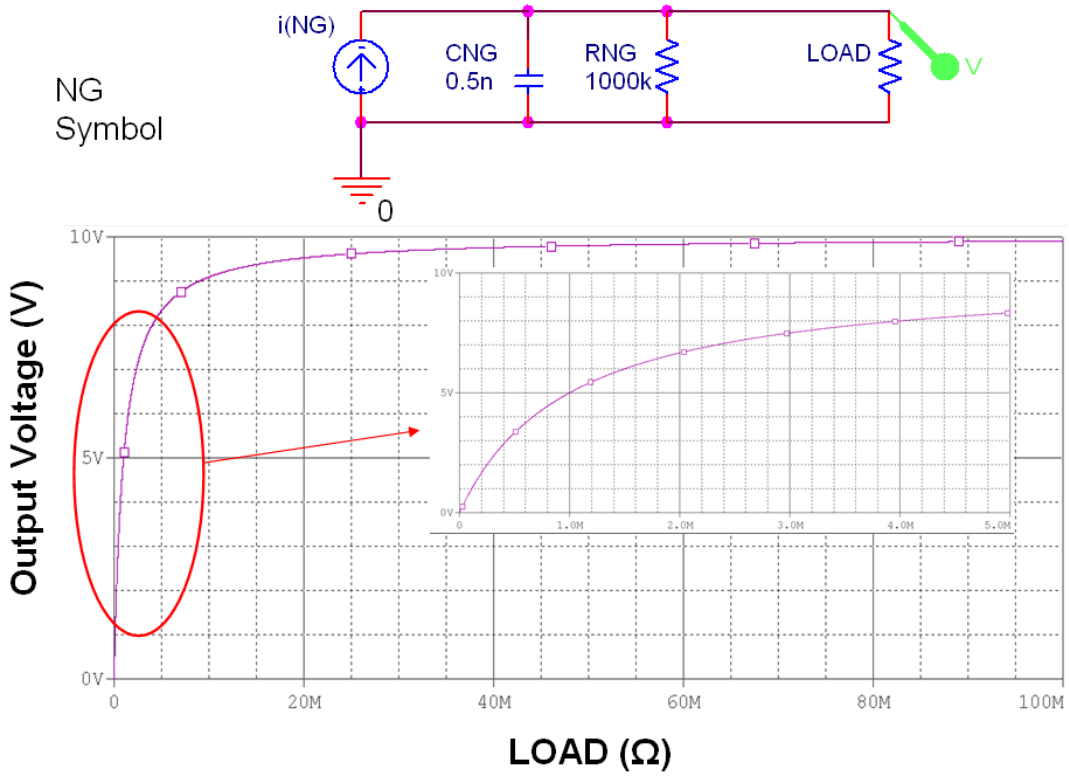

Figure 7.8 Equivalent nanogenerator circuit

Figure 7.9 shows the equivalent electrical model of the NG with the rectifier. The instantaneously harvested power is weak, so it may not be able to sustain continuous operations of

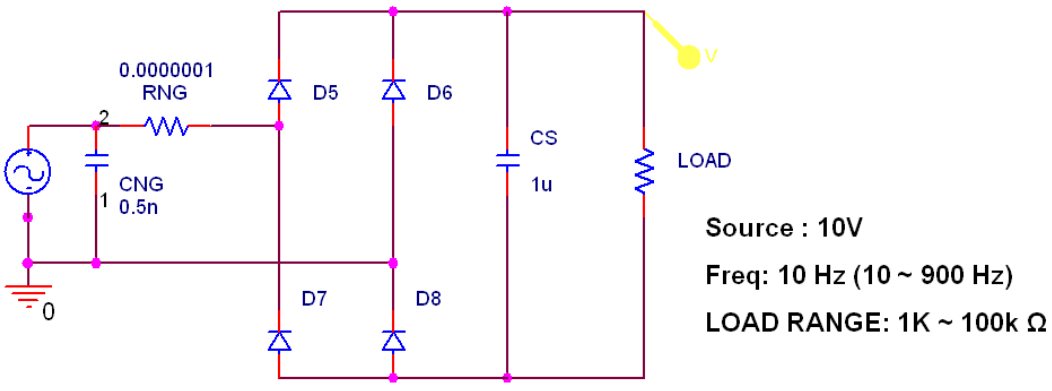

Figure 7.9 NG circuit with the rectifier

the application. The capacitor Cs is inserted to accumulate the harvested power. The real-time harvested power p(t) at the output of the rectifier heavily depends on the load resistance (LOAD) and the source frequency (f), which are not constant but varied with the practical subsystem and time. Thus, the maximum power also changes with these two variables. We simulated the harvested power with different load resistance and source frequencies, as plotted in Figures 7.10 and 7.11, which show that the output power varies significantly. To achieve a maximum harvested power, we need to maintain the load at a very low level, but the source frequency at a high level. To get the maximum power within our simulated range, the proposed value is 1kΩ for the load resistance and 900Hz for the source frequency.

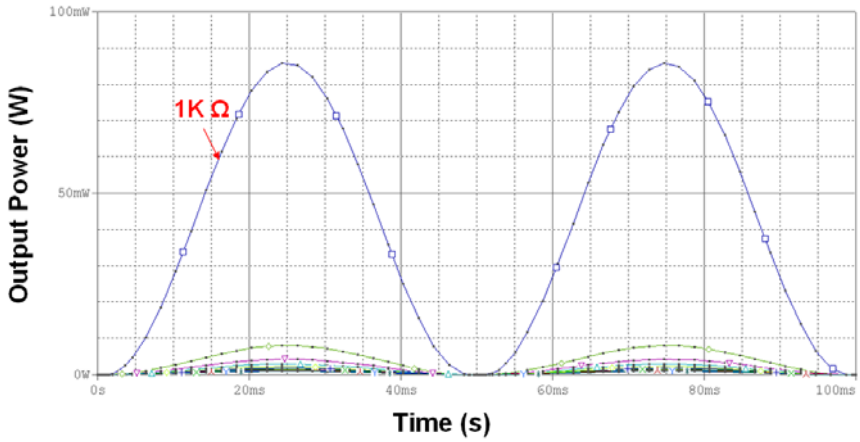

Figure 7.10 NG power vs. time in terms of frequency

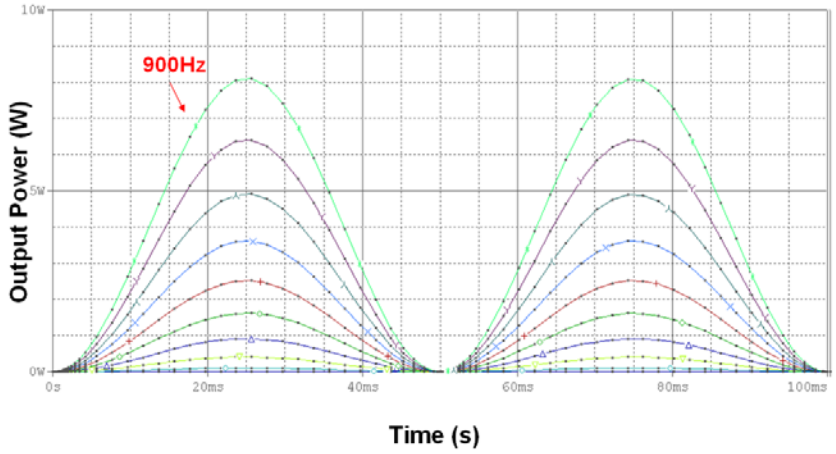

Figure 7.11 NG power vs. time in terms of frequency

Solar cell

Figure 7.12 shows the electrical model of a PV cell. The photocurrent varies with the light irradiance, Rs is the parasitic serial resistance, Rsh is the equivalent shunt resistance, and D1 is the forward-biased diode of the solar cell. We conducted simulations based on the circuit in Figure 7.12, in which we fix the photocurrent at 10mA. Both the output voltage and the power change with various resistive loads. From the plotted results in Figures 7.12 and 7.13, the output voltage has a saturation value with an increase in the load while the optimal power reaches only 50Ω, based on our simulation.

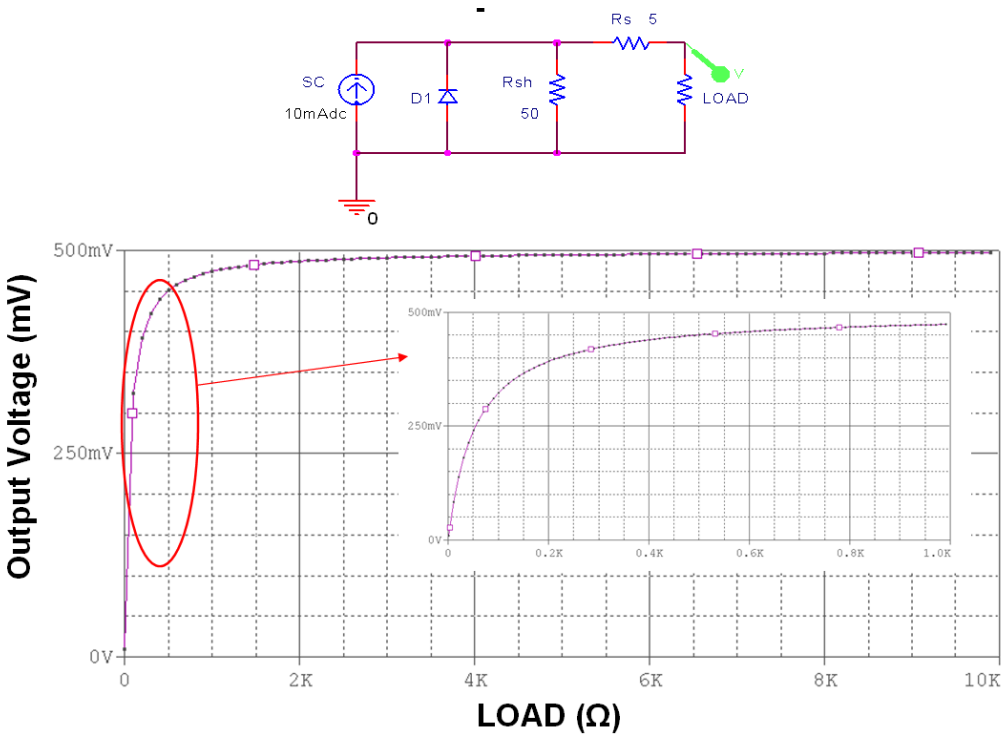

Figure 7.12 Solar cell circuit and output voltage vs. load

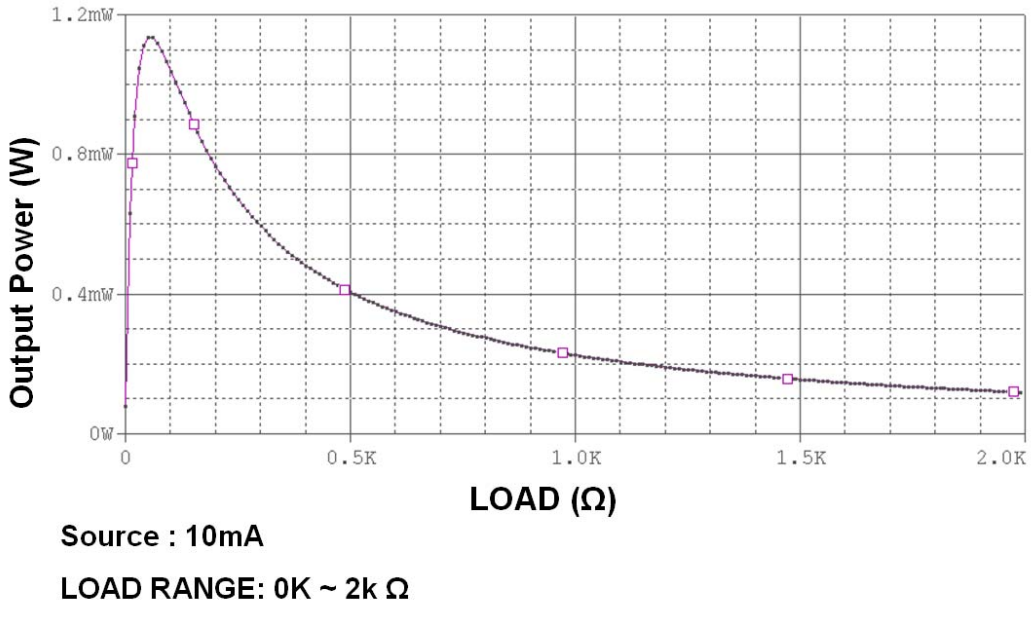

Figure 7.13 Solar cell power vs. load

7.2.3 Electrical model of the hybrid cell

In previous sections, we have presented two electrical models of the energy harvester. Figure 7.14 shows the equivalent circuit of a hybrid cell, which is mainly composed of an NG circuit with a rectifier and an SC circuit. According to our experiments, the NG source has a 10μA AC output current while the SC source has a 10mA DC output current. Based on the circuit shown in Figure 7.14, the output power also varies with the load resistance and other factors. Because of limitations of time and the complexity of developing multi-type harvesting modalities, we simulated the output power of the hybrid cell that changes with the load first. Figure 7.15 shows that the hybrid cell with a subsystem load at 100Ω has the most power output.

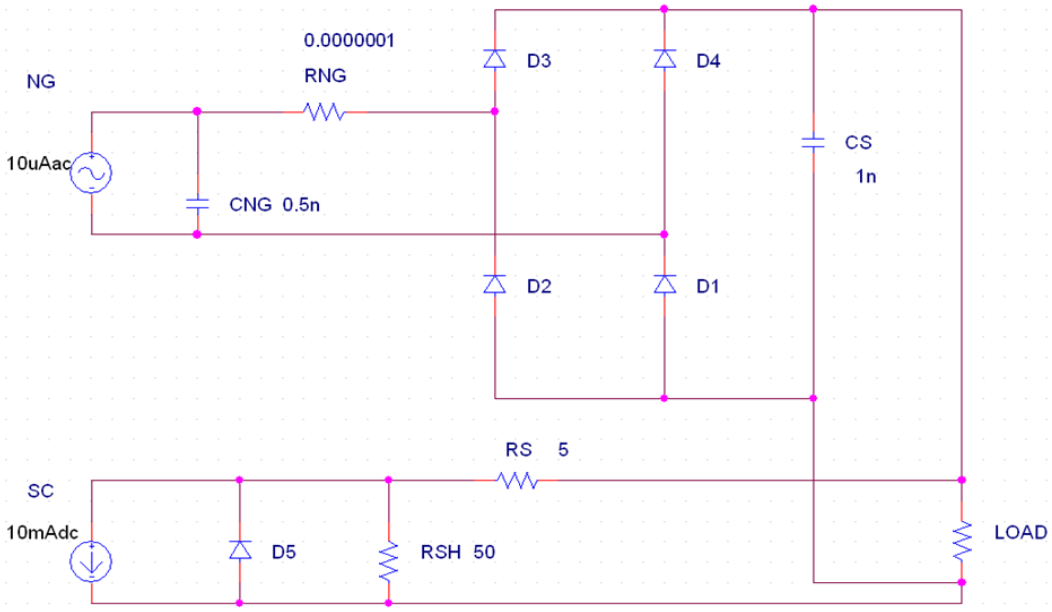

Figure 7.14 Hybrid cell equivalent circuit with the rectifier

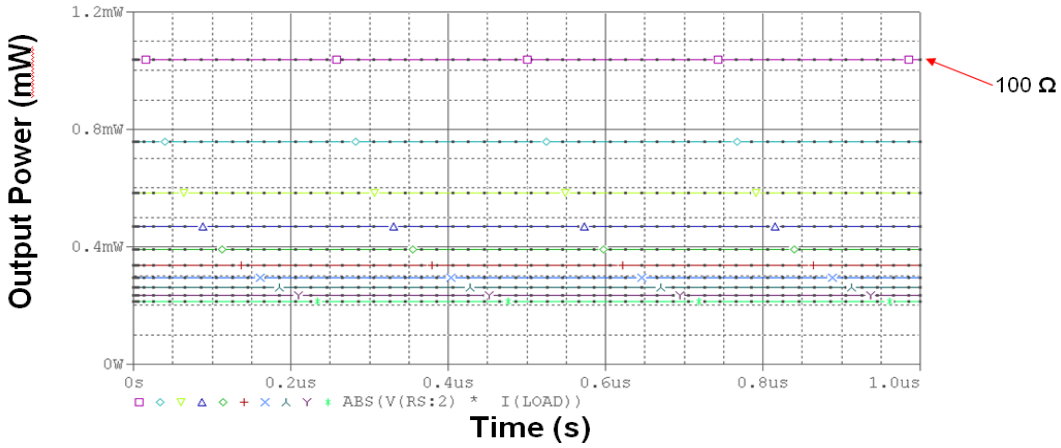

Figure 7.15 Hybrid cell (variable load) power vs. time

The approach we used in the dissertation presents a simple overview of the various system-level tradeoffs and considerations involved in the design of such highly efficient micro-scale energy harvesting systems. Despite the extensive exploration of environmental energy harvesting and its applications to practical systems, many challenges with regard to the design of an efficient hybrid with a well matched subsystem remain. To really implement hybrid cells in practical applications, we need more investigation from a system design perspective, as shown in Figure 7.7.

CHAPTER 8

CONCLUSION

The search for sustainable power sources for driving nanosystems is an emerging field in the energy research of today, and harvesting energy from multiple sources available in the environment to create self-powered nanosystems is now becoming a technological reality. This dissertation focuses on innovative research on hybrid cells for multi-type energy harvesting based on ZnO nanostructures, which show great promise.

Starting from the prototype, by sharing the integrated electrode, the hybrid cell (HC) integrates a Dye-sensitized Solar Cell (DSSC) and a piezoelectric Nanogenerator (NG) built by sharing electrodes and using ZnO nanowire arrays (NWs) as a common material for both units. Through the introduction of various fabrication procedures, the integration of the DSSC and the NG can be either in a series or in parallel.

With an understanding of the principle of the HC, we need to further explore methods of improving the ability to harvest multi-type energy from the environment using HCs. Also, because of the encapsulation problem originating from the use of the liquid electrolyte in conventional DSSC, solvent leakage and evaporation are two major obstacles. An innovative method to make the second generation of HC has been developed to convolute a solid state dye sensitized solar cell and an ultrasonic wave driven piezoelectric nanogenerator into a single compacted structure for concurrently harvesting solar and mechanical energies. With the introduction of a solid electrolyte to its DSSC part, we improved the HC so that it was more reliable than the liquid-based cell.

Even though these results have proven the ability to harvest multi-type energy, the low output of the HC still prevents it from being applied in practice. Towards more practical applications of HCs, this study has also made major enhancements in their reliability and performance. So that the high output NG unit can function as not only a complementary source but also a reliable independent source, its output has to be raised.

By scaling up the size, the output of the NGs has greatly increased, and it is now even large enough to light up the liquid crystal display.

For real applications, the maximum power output of these micro-scale transducers is extremely small, often only a few mW. Therefore, we investigated the harvesting subsystem to find methods of extracting as much power as possible from the transducer and transferring it to the electronic system with minimal loss, which requires an extremely energy efficient design. The core of this dissertation is the successful fabrication of an HC that paves the way to a new research field: multi-type energy harvesting. An illustration is the fabrication of an HC that harvests solar and mechanical energies.

In summary, this dissertation presents systematic research on the HC, a roadmap for a real application of multi-type energy harvesting. From the fabrication of the prototype HC that demonstrates an energy-harvesting capability, an HC that integrates DSSC and NG has been developed and a comparison between enhancements in energy conversion efficiency and those in effective energy recovery processes has been illustrated. Potential applications that demonstrate the utilization of multiple types of energy in the environment in an effective and complementary manner whenever and wherever one or all of them are available have also been discussed.

As a new field in nanotechnology-related research, we anticipate witnessing the impact of HC technology on nanosystems and even microsystems, which are intelligent, multifunctional, super small, extremely sensitive, and energy efficient. Still in its incipient stages, the field is still wide open with many opportunities for inquiry. In the near future, we expect to develop more HCs capable of harvesting all available energy sources in our living environment in addition to solar and mechanical energies. For specific applications, HCs can be developed by combining the harvesting of thermal and solar energies, sound and solar energies. More efforts on the part of both scientists and engineers will help advance HC technology, the development of which should stimulate

the creation other novel research areas and state-of-the-art technology. These efforts, along with the work presented in this dissertation, will help build a solid foundation for the advancement of multi-type energy harvesting.

REFERENCES

1. Waters, W. E.; Wilkins, H. F., *Hortscience* **1979,** *14* (2), 146-146.
2. Guo, D. G.; Zhang, X. Y.; Shao, H. B.; Bai, Z. K.; Chu, L. Y.; Shangguan, T. L.; Yan, K.; Zhang, L. H.; Xu, G.; Sun, J. N., *Renew Sust Energ Rev* **2011,** *15* (4), 2014-2020.
3. http://www.consumerenergyreport.com/2011/07/14/renewables-2011-global-status-report-released/.
4. Dresselhaus, M. S.; Thomas, I. L., *Nature* **2001,** *414* (6861), 332-337.
5. Hagfeldt, A.; Gratzel, M., *Accounts of Chemical Research* **2000,** *33* (5), 269-277.
6. Nazeeruddin, M. K.; Kay, A.; Rodicio, I.; Humphrybaker, R.; Muller, E.; Liska, P.; Vlachopoulos, N.; Gratzel, M., *Journal of the American Chemical Society* **1993,** *115* (14), 6382-6390.
7. Oregan, B.; Gratzel, M., *Nature* **1991,** *353* (6346), 737-740.
8. Huynh, W. U.; Dittmer, J. J.; Alivisatos, A. P., *Science* **2002,** *295* (5564), 2425-2427.
9. Yu, G.; Gao, J.; Hummelen, J. C.; Wudl, F.; Heeger, A. J., *Science* **1995,** *270* (5243), 1789-1791.
10. Pei, Q. B.; Yu, G.; Zhang, C.; Yang, Y.; Heeger, A. J., *Science* **1995,** *269* (5227), 1086-1088.
11. Tian, B. Z.; Zheng, X. L.; Kempa, T. J.; Fang, Y.; Yu, N. F.; Yu, G. H.; Huang, J. L.; Lieber, C. M., *Nature* **2007,** *449* (7164), 885-U8.
12. Gur, I.; Fromer, N. A.; Geier, M. L.; Alivisatos, A. P., *Science* **2005,** *310* (5747), 462-465.
13. Liboff, R. L., *Energy Sources* **1978,** *3* (3-4), 255-261.
14. Diffen, B. H., *Power* **2011,** *155* (12), 164-164.
15. DiSalvo, F. J., *Science* **1999,** *285* (5428), 703-706.
16. Dresselhaus, M. S.; Chen, G.; Tang, M. Y.; Yang, R. G.; Lee, H.; Wang, D. Z.; Ren, Z. F.; Fleurial, J. P.; Gogna, P., *Advanced Materials* **2007,** *19* (8), 1043-1053.
17. Pfann, W. G.; Vanroosbroeck, W., *Journal of Applied Physics* **1954,** *25* (11), 1422-1434.

18. Halls, J. J. M.; Walsh, C. A.; Greenham, N. C.; Marseglia, E. A.; Friend, R. H.; Moratti, S. C.; Holmes, A. B., *Nature* **1995,** *376* (6540), 498-500.
19. Wang, Z. L.; Song, J. H., *Science* **2006,** *312* (5771), 242-246.
20. Wang, Z. L., *Scientific American* **2008,** *298* (1), 82-+.
21. Paradiso, J. A.; Starner, T., *Ieee Pervasive Computing* **2005,** *4* (1), 18-27.
22. Pan, C. F.; Wu, H.; Wang, C.; Wang, B.; Zhang, L.; Cheng, Z. D.; Hu, P.; Pan, W.; Zhou, Z. Y.; Yang, X.; Zhu, J., *Adv Mater* **2008,** *20* (9), 1644-+.
23. Cui, Y.; Lieber, C. M., *Science* **2001,** *291* (5505), 851-853.
24. Pan, Z. W.; Dai, Z. R.; Wang, Z. L., *Science* **2001,** *291* (5510), 1947-1949.
25. Mahfuz, M. U.; Ahmed, K. M., *Sci Technol Adv Mat* **2005,** *6* (3-4), 302-306.
26. Chang, S. M.; Kim, Y. H.; Kim, J. M.; Chang, Y. K.; Kim, J. D., *Mol Cryst Liq Crys A* **1995,** *267*, 405-410.
27. Ferain, E.; Legras, R., *Nucl Instrum Meth B* **2009,** *267* (6), 1028-1031.
28. Song, J. H.; Zhang, Y.; Xu, C.; Wu, W. Z.; Wang, Z. L., *Nano Letters* **2011,** *11* (7), 2829-2834.
29. *Am Ceram Soc Bull* **2005,** *84* (1), 6-6.
30. Frank, S.; Poncharal, P.; Wang, Z. L.; de Heer, W. A., *Science* **1998,** *280* (5370), 1744-1746.
31. Comini, E.; Faglia, G.; Sberveglieri, G.; Pan, Z. W.; Wang, Z. L., *Applied Physics Letters* **2002,** *81* (10), 1869-1871.
32. Morales, A. M.; Lieber, C. M., *Science* **1998,** *279* (5348), 208-211.
33. Iijima, S., *Nature* **1991,** *354* (6348), 56-58.
34. Odom, T. W.; Huang, J. L.; Kim, P.; Lieber, C. M., *Nature* **1998,** *391* (6662), 62-64.
35. Park, Y. K.; Umar, A.; Lee, E. W.; Hong, D. M.; Hahn, Y. B., *J Nanosci Nanotechno* **2009,** *9* (10), 5745-5751.
36. Erbe, A.; Blick, R. H., *Ieee T Ultrason Ferr* **2002,** *49* (8), 1114-1117.
37. Hughes, W. L.; Wang, Z. L., *Appl Phys Lett* **2003,** *82* (17), 2886-2888.
38. Wang, Z. L., *Chinese Sci Bull* **2009,** *54* (22), 4021-4034.
39. Yao, B. D.; Chan, Y. F.; Wang, N., *Appl Phys Lett* **2002,** *81* (4), 757-759.
40. Xu, C. X.; Sun, X. W.; Dong, Z. L.; Yu, M. B., *J Cryst Growth* **2004,** *270* (3-4), 498-504.

41. Kong, X. Y.; Ding, Y.; Yang, R.; Wang, Z. L., *Science* **2004,** *303* (5662), 1348-1351.
42. Kong, X. Y.; Wang, Z. L., *Applied Physics Letters* **2004,** *84* (6), 975-977.
43. Kong, X. Y.; Wang, Z. L., *Nano Letters* **2003,** *3* (12), 1625-1631.
44. Wang, X. D.; Song, J. H.; Li, P.; Ryou, J. H.; Dupuis, R. D.; Summers, C. J.; Wang, Z. L., *Journal of the American Chemical Society* **2005,** *127* (21), 7920-7923.
45. Gupta, M.; Spivey, J. J., *Catal Today* **2009,** *147* (2), 126-132.
46. Wan, Q.; Li, Q. H.; Chen, Y. J.; Wang, T. H.; He, X. L.; Li, J. P.; Lin, C. L., *Appl Phys Lett* **2004,** *84* (18), 3654-3656.
47. Zhou, Q. F.; Sharp, C.; Cannata, J. M.; Shung, K. K.; Feng, G. H.; Kim, E. S., *Appl Phys Lett* **2007,** *90* (11).
48. Park, W. I.; Yi, G. C., *Adv Mater* **2004,** *16* (1), 87-+.
49. Zhang, X. M.; Lu, M. Y.; Zhang, Y.; Chen, L. J.; Wang, Z. L., *Adv Mater* **2009,** *21* (27), 2767-+.
50. Xu, S.; Xu, C.; Liu, Y.; Hu, Y. F.; Yang, R. S.; Yang, Q.; Ryou, J. H.; Kim, H. J.; Lochner, Z.; Choi, S.; Dupuis, R.; Wang, Z. L., *Adv Mater* **2010,** *22* (42), 4749-+.
51. Ozgur, U.; Alivov, Y. I.; Liu, C.; Teke, A.; Reshchikov, M. A.; Dogan, S.; Avrutin, V.; Cho, S. J.; Morkoc, H., *J Appl Phys* **2005,** *98* (4).
52. Look, D. C., *Mat Sci Eng B-Solid* **2001,** *80* (1-3), 383-387.
53. Heo, Y. W.; Norton, D. P.; Tien, L. C.; Kwon, Y.; Kang, B. S.; Ren, F.; Pearton, S. J.; LaRoche, J. R., *Mat Sci Eng R* **2004,** *47* (1-2), 1-47.
54. Yang, R. S.; Ding, Y.; Wang, Z. L., *Nano Letters* **2004,** *4* (7), 1309-1312.
55. Park, W. I.; Yi, G. C.; Kim, J. W.; Park, S. M., *Applied Physics Letters* **2003,** *82* (24), 4358-4360.
56. Harnack, O.; Pacholski, C.; Weller, H.; Yasuda, A.; Wessels, J. M., *Nano Letters* **2003,** *3* (8), 1097-1101.
57. Greene, L. E.; Law, M.; Goldberger, J.; Kim, F.; Johnson, J. C.; Zhang, Y. F.; Saykally, R. J.; Yang, P. D., *Angewandte Chemie-International Edition* **2003,** *42* (26), 3031-3034.
58. Green, M. A.; Blakers, A. W.; Narayanan, S.; Taouk, M., *Sol Cells* **1986,** *17* (1), 75-83.

59. Zhao, J. H.; Wang, A. H.; Altermatt, P. P.; Wenham, S. R.; Green, M. A., *Sol Energ Mat Sol C* **1996,** *41-2*, 87-99.
60. Zhao, J. H.; Wang, A. H.; Green, M. A., *Prog Photovoltaics* **1997,** *5* (3), 169-174.
61. Green, M. A.; Wenham, S. R., *Appl Phys Lett* **1994,** *65* (23), 2907-2909.
62. Shen, C. C.; Pearson, G. L., *P Ieee* **1976,** *64* (3), 384-385.
63. James, L. W.; Moon, R. L., *Appl Phys Lett* **1975,** *26* (8), 467-470.
64. Blakeslee, A. E.; Vernon, S. M., *Ibm J Res Dev* **1978,** *22* (4), 346-352.
65. Sun, S.; Fan, Z.; Wang, Y.; Haliburton, J., *J Mater Sci* **2005,** *40* (6), 1429-1443.
66. Ma, T. L., *Prog Chem* **2006,** *18* (2-3), 176-181.
67. Kruger, J.; Plass, R.; Gratzel, M.; Cameron, P. J.; Peter, L. M., *Journal of Physical Chemistry B* **2003,** *107* (31), 7536-7539.
68. Ohsaki, Y.; Masaki, N.; Kitamura, T.; Wada, Y.; Okamoto, T.; Sekino, T.; Niihara, K.; Yanagida, S., *Phys Chem Chem Phys* **2005,** *7* (24), 4157-4163.
69. Law, M.; Greene, L. E.; Johnson, J. C.; Saykally, R.; Yang, P. D., *Nature Materials* **2005,** *4* (6), 455-459.
70. Han, J. B.; Fan, F. R.; Xu, C.; Lin, S. S.; Wei, M.; Duan, X.; Wang, Z. L., *Nanotechnology* **2010,** *21* (40).
71. Wei, Y. G.; Xu, C.; Xu, S.; Li, C.; Wu, W. Z.; Wang, Z. L., *Nano Letters* **2010,** *10* (6), 2092-2096.
72. WenxiGuo, C., GuangZhu, CaofengPan, Changjian Lin, ZhongLinWang, *Nano Energy* **2011**.
73. Song, J. H.; Zhou, J.; Wang, Z. L., *Nano Letters* **2006,** *6* (8), 1656-1662.
74. Wang, X. D.; Song, J. H.; Liu, J.; Wang, Z. L., *Science* **2007,** *316* (5821), 102-105.
75. Xi, Y.; Lien, D. H.; Yang, R. S.; Xu, C.; Hu, C. G., *Phys Status Solidi-R* **2011,** *5* (2), 77-79.
76. Gonzalo Murillo, M. L., Chen Xu, Gabriel Abadal, Zhong Lin Wan, *Nano Communication Networks* **2011**.
77. Wang, X. D.; Liu, J.; Song, J. H.; Wang, Z. L., *Nano Letters* **2007,** *7* (8), 2475-2479.
78. Xu, S.; Wei, Y. G.; Liu, J.; Yang, R.; Wang, Z. L., *Nano Letters* **2008,** *8* (11), 4027-4032.

79. Xu, C.; Wang, X. D.; Wang, Z. L., *Journal of the American Chemical Society* **2009,** *131* (16), 5866-5872.
80. Zhang, J.; Sun, L. D.; Liao, C. S.; Yan, C. H., *Chem Commun* **2002,** (3), 262-263.
81. Zhang, D. F.; Sun, L. D.; Yin, J. L.; Yan, C. H.; Wang, R. M., *J Phys Chem B* **2005,** *109* (18), 8786-8790.
82. Liu, J.; Fei, P.; Song, J. H.; Wang, X. D.; Lao, C. S.; Tummala, R.; Wang, Z. L., *Nano Letters* **2008,** *8* (1), 328-332.
83. Liu, J.; Fei, P.; Zhou, J.; Tummala, R.; Wang, Z. L., *Applied Physics Letters* **2008,** *92* (17), -.
84. Bach, U.; Lupo, D.; Comte, P.; Moser, J. E.; Weissortel, F.; Salbeck, J.; Spreitzer, H.; Gratzel, M., *Nature* **1998,** *395* (6702), 583-585.
85. Boucharef, M.; Di Bin, C.; Boumaza, M. S.; Colas, M.; Snaith, H. J.; Ratier, B.; Boucle, J., *Nanotechnology* **2010,** *21* (20), -.
86. Xu, C.; Wang, Z. L., *Adv Mater* **2011,** *23* (7), 873-+.
87. Qin, Y.; Wang, X.; Wang, Z. L., *Nature* **2009,** *457* (7227), 340-340.
88. Gao, Z. Y.; Zhou, J.; Gu, Y. D.; Fei, P.; Hao, Y.; Bao, G.; Wang, Z. L., *J Appl Phys* **2009,** *106* (3).
89. Gao, Y.; Wang, Z. L., *Nano Lett* **2009,** *9* (3), 1103-1110.
90. Wang, Z. L.; Yang, R. S.; Zhou, J.; Qin, Y.; Xu, C.; Hu, Y. F.; Xu, S., *Mat Sci Eng R* **2010,** *70* (3-6), 320-329.
91. Hu, Y. F.; Zhang, Y.; Xu, C.; Zhu, G. A.; Wang, Z. L., *Nano Letters* **2010,** *10* (12), 5025-5031.
92. Service, R. F., *Science* **2010,** *328* (5976), 304-305.
93. Chang, C. E.; Tran, V. H.; Wang, J. B.; Fuh, Y. K.; Lin, L. W., *Nano Lett* **2010,** *10* (2), 726-731.
94. Choi, D.; Choi, M. Y.; Choi, W. M.; Shin, H. J.; Park, H. K.; Seo, J. S.; Park, J.; Yoon, S. M.; Chae, S. J.; Lee, Y. H.; Kim, S. W.; Choi, J. Y.; Lee, S. Y.; Kim, J. M., *Adv Mater* **2010,** *22* (19), 2187-+.
95. Yang, R.; Qin, Y.; Li, C.; Zhu, G.; Wang, Z. L., *Nano Lett* **2009,** *9* (3), 1201-1205.
96. Hu, Y. F.; Xu, C.; Zhang, Y.; Lin, L.; Snyder, R. L.; Wang, Z. L., *Advanced Materials* **2011,** *23* (35), 4068-+.

97. Hu, Y. F.; Zhang, Y.; Xu, C.; Lin, L.; Snyder, R. L.; Wang, Z. L., *Nano Letters* **2011,** *11* (6), 2572-2577.
98. Lin, L.; Lai, C. H.; Hu, Y. F.; Zhang, Y.; Wang, X.; Xu, C.; Snyder, R. L.; Chen, L. J.; Wang, Z. L., *Nanotechnology* **2011,** *22* (47).
99. Lu, C. R., V.; Roy, K.;, *IEEE JETCAS* **2011,** *1* (3), 254-266.
100. Jeon, Y. B.; Sood, R.; Jeong, J. H.; Kim, S. G., *Sensor Actuat a-Phys* **2005,** *122* (1), 16-22.
101. Alahmad, M.; Hess, H., *Iet Circ Device Syst* **2010,** *4* (3), 261-268.
102. Nutter, L. N., *Solid State Technol* **2011,** *54* (7), 32-34.